Universidade de Brasília – UnB
Campus Gama – FGA
Programa de Pós-Graduação em Engenharia Biomédica

Compressive Sensing Using Directional Filters for Magnetic Resonance Image Reconstruction under Different k-Space Trajectories

Jéssica Vivian Moreira da Silva

Orientador: Dr. Cristiano Jacques Miosso

UnB – Universidade de Brasília

FGA – Faculdade Gama

Programa de Pós-Graduação

Compressive Sensing Using Directional Filters for Magnetic Resonance Image Reconstruction under Different k-Space Trajectories

Jéssica Vivian Moreira da Silva

Orientador: Cristiano Jacques Miosso

Dissertação de Mestrado em
Engenharia Biomédica

Publicação: 108A/2019

Brasília/DF, June 2019

UnB — Universidade de Brasília

FGA — Faculdade Gama

Programa de Pós-Graduação

Compressive Sensing Using Directional Filters for Magnetic Resonance Image Reconstruction under Different k-Space Trajectories

Jéssica Vivian Moreira da Silva

Dissertação de mestrado submetida ao programa de pós-graduação da Faculdade Gama da Universidade de Brasília, como parte dos requisitos necessários para a obtenção do grau de mestra em engenharia biomédica

Aprovada por:

Cristiano Jacques Miosso
(Orientador)

Dr. Fabiano Araújo Soares
(Examinador interno)

Dr. Ricardo von Borries
(Examinador externo)

Brasília/DF, June 2019

Catalog Information

Vivian, Jéssica
Compressive Sensing Using Directional Filters for Magnetic Resonance Image Reconstruction under Different $\boldsymbol{k}$-Space Trajectories[Distrito Federal], 2019.
95p., 210 × 297 mm (FGA/UnB Gama, Mestrado em Engenharia Biomédica, 2019).
Dissertação de Mestrado em Engenharia Biomédica, Faculdade UnB Gama, Programa de Pós-Graduação em Engenharia Biomédica.
1. Compressive Sensing — 2. Magnetic Resonance Imaging (MRI)
3. Prefiltering — 4. Directional filters
I. FGA UnB/UnB. — II. Título (série)

Reference

Vivian, Jéssica (2019). Compressive Sensing Using Directional Filters for Magnetic Resonance Image Reconstruction under Different $\boldsymbol{k}$-Space Trajectories. Dissertação de mestrado em engenharia biomédica, Publicação 108A/2019, Programa de Pós-Graduação, Faculdade UnB Gama, Universidade de Brasília, Brasília, DF, 95p.

Copyright Agreement

Autor: Jéssica Vivian Moreira da Silva

Título: Compressive Sensing Using Directional Filters for Magnetic Resonance Image Reconstruction under Different $\boldsymbol{k}$-Space Trajectories

Grau: Mestra

Ano: 2019

jessicavivian.eng@gmail.com

Brasília, DF – Brasil

It is not the critic who counts; not the man who points out how the strong man stumbles, or where the doer of deeds could have done them better. The credit belongs to the man who is actually in the arena, whose face is marred by dust and sweat and blood, who strives valiantly; who errs and comes short again and again; because there is not effort without error and shortcomings; but who does actually strive to do the deed; who knows the great enthusiasm, the great devotion, who spends himself in a worthy cause, who at the best knows in the end the triumph of high achievement and who at the worst, if he fails, at least he fails while daring greatly. So that his place shall never be with those cold and timid souls who know neither victory nor defeat.

- Theodore Roosevelt

To my parents and my brother, thank you for everything. To Alexandre and the family we have built, you and the three little ones light up my days and make me want to be my best version.

Acknowledgment

I would like to express my special thanks and gratitude to my research advisor, Dr. Cristiano Jacques Miosso, who have been guiding me since my undergraduate research. His guidance and countless hours teaching me about magnetic resonance imaging, compressive sensing, linear algebra and stochastic process opened my eyes to a part of science that would take me decades of study to understand it by myself. I could not have hoped for a better advisor than Dr. Miosso. He is the most gentle and patient person I know. I will be a really accomplished researcher if I turn out to be half of the researcher you are!

I would also like to extend my gratitude to the Dr. Fabiano Araújo Soares, Dr. Ricardo von Borries and Dr. Adson Ferreira da Rocha, who accepted to be part of this research contributing with valuable suggestions, encouragement and insightful comments.

I thank the Programa de Pós Graduação em Engenharia Biomédica (PPGEB) for the opportunity in pursuing my Master degree and all the professors who contributed to my learning. Also, I thank the professors involved in the collaboration project between the University of Brasília (UnB) and the University of Texas (UTEP), at el Paso that made possible for me to run my simulations in the Virgo cluster. This study was financed in part by the Coordenação de Aperfeiçoamento de Pessoal de Nível Superior - Brasil (CAPES).

To conclude, I want to give a special thanks to my fiancé Alexandre, you have supported me all this time and always had positive thoughts to help me see the best side of things. I will need a life time to express how grateful and lucky I feel for having you in my life. Also, thanks to my parents and my brother, who encouraged me and supported in all those years.

Resumo Estendido

Compressive Sensing Using Directional Filters for Magnetic Resonance Image Reconstruction under Different k-Space Trajectories

Autora: Jéssica Vivian Moreira da Silva

Orientador: Prof. Dr. Cristiano Jacques Miosso

Programa de Pós-Graduação em Engenharia Biomédica

Dissertação de Mestrado Brasília-DF. Junho de 2019

Introdução

Nós vivemos na era do big data, da Internet das coisas, do aprimoramento genético e da recodificação do genoma. No entanto, visualizar os componentes internos do corpo humano e suas funcionalidades ainda é um desafio. Uma breve pesquisa sobre os artigos mais recentes publicados de 2018 a 2019 no campo da imagiologia médica com Ressonância Magnética (RM) nas bases de dados da Biblioteca Digital IEEE Xplore, PubMed e Web of Science, apresentou uma coleção de 50.574 estudos sobre detecção, segmentação, extração, delineação, diagnóstico e classificação das patologias do corpo humano e características fisiológicas.

A prevalência de tais estudos indica que os pesquisadores estão direcionando seus esforços para serem precisos e assertivos em relação ao diagnóstico, procedimentos e tratamentos. O imageamento por ressonância magnética (IRM) tem mostrado ser uma ferramenta poderosa e flexível capaz de gerar imagens de diferentes aspectos do corpo humano [30]. O exame de RM é conhecido principalmente devido à sua superioridade no que diz respeito ao contraste do tecido, o que aumenta as chances de diagnóstico em comparação com outras técnicas como raios-X, radiografia e tomografia computadorizada (CT) [21, 32]. Além disso, a RM permite o uso de várias técnicas e dispositivos auxiliares para adquirir imagens de alta resolução úteis em muitas fases da intervenção médica. Pesquisas recentes sobre IRM mostram avanços no diagnóstico precoce da síndrome de Sturge-Weber, a detecção de lipossarcoma mixóide metástases antes dos sintomas clínicos e metástases pulmonares, a predição de distúrbios respiratórios em pacientes com Esclerose Lateral Amiotrófica (ELA), revelando atrofia medular cervical precoce [2, 24, 25], e a adequação de IRM na triagem de câncer de pulmão e nódulos com diâmetros acima de 6 milimetros [35]. Embora o cenário para o IRM seja promissor em relação a novas aplicações e técnicas relacionadas à escolha de pulsos RF e trajetórias de aquisição, o exame ainda enfrenta complicações e problemas relacionados à aceitação do paciente. Os exames leva de 45 a 60 minutos por parte do corpo, e o paciente tem que ficar parado por um longo período de tempo, frequentemente em posições muito desconfortáveis. Isso é especialmente desafiador no caso de pacientes pediátricos, que por vezes requerem sedação ou anestesia geral. Esse procedimento envolve riscos ao paciente e necessita de pessoal especializado e equipamento de monitoramento [17]. Outro caso desafiador é o dos pacientes claustrofóbicos, para quem às vezes o exame acaba por não ser uma opção viável, principalmente quando os pacientes precisam estar atentos e responsivos [20]. Visando reduzir o tempo total do exame, técnicas de reconstrução de imagem baseadas em Compressive Sensing (CS) foram desenvolvidas e tiveram resultados positivos com relação ao número de medidas no domínio do espaço-k [34, 11, 38, 28]. Pesquisas recentes usando pré-filtragem mostraram resultados favoráveis relacionados ao tempo de reconstrução, número de medições requeridas e qualidade de imagem. Essas pesquisas, no entanto, não inspecionaram possíveis relações entre diferentes trajetórias no domínio do espaço-k e pré-filtragem. Em [42] a técnica de pré-filtragem é testada com uma variedade de famílias de filtros, todas elas correspondendo a respostas de frequência não direcionais. No entanto, não encontramos estudos sistemáticos com pré-filtragem sob diferentes cenários, com diferentes trajetórias e filtros direcionais.

Objetivos Gerais

Esta pesquisa tem como objetivo avaliar o potencial de esparsificação dos filtros direcionais e o quanto eles afetam a imagem final reconstruída ao usar CS com pré-filtragem. O objetivo principal é explorar características dos filtros direcionais e como elas afetam a esparsidade de imagens quando comparado com os filtros de Haar, que foram usados nas primeiras estratégias de pré-filtragem. A hipótese é que os filtros direcionais podem produzir imagens mais esparsas, uma vez que podem extrair componentes de alta frequência em direções específicas.

Metodologia

Nesta pesquisa, avaliamos o uso de filtros direcionais para reconstrução de imagens de ressonância magnética utilizando CS com pré-filtragem. Argumentamos que os filtros direcionais podem melhorar a reconstrução quando comparados aos filtros separáveis, como os usados nos primeiros trabalhos de pré-filtragem. Inicialmente, começamos projetando e implementando filtros direcionais considerando uma variação suave no domínio da frequência, onde a frequência máxima é colocada em um determinado ângulo, variando em toda a faixa de frequências até chegar em zero, esses são os filtros dos cenários I e II. Já os demais filtros dos cenários III, IV e V foram projetados e implementados levando em conta uma distribuição em faixa de frequência igualmente dividido entre o número de filtros no conjunto. O design desses filtros seguem três etapas como resumido na Figura 1. Para testar os filtros propostos utilizamos dois fantomas de cabeça (Shepp-Logan e Cérebro) e uma imagem real do cérebro em corte sagital, comparando esse resultado com reconstrução com pré-filtragem utilizado filtros de Haar e reconstruções com Total Variation (TV). Utilizamos parâmetros de qualidades como a razão sinal-erro (SER) e o índice de similaridade estrutural (SSIM)

Resultados

No geral, os índices de qualidade mostram que, ao truncar os filtros com janelas que têm *ripples* fixas como Blackman, Hann e Hamming compensam em termos de diminuir os efeitos do fenômeno de Gibbs e isso tem um efeito positivo na qualidade das imagens finais reconstruídas. Este efeito pode é visto nos resultados do cenário III, onde todos os resultados para os filtros janelados com uma janelas retangulares estão abaixo do SER dos outros filtros para o mesma imagem reconstruída. A partir das reconstruções com fantomas, notamos que os filtros direcionais pareciam se beneficiar da estrutura do fantoma do Cérebro e isso se refletia no SER mais alto que o do fantoma de Shepp-Logan. Por essa razão, reconstruímos uma imagem real de cabeça em corte sagital. Nós primeiro adquirimos medidas na mesma trajetória com 90 linhas radiais no espaço-k utilizada para os fantomas e em seguida com uma trajetória em espiral com crescimento do raio exponencial e 180 voltas. Os principais resultados das reconstruções estão resumidos na Tabela 4.1.

Tabela 1. Resultados SER e SSIM para a reconstrução usando CS com pré-filtragem com filtros Haar no esquema 3 configurado como em [37], pré-filtragem com filtros direcionais e as reconstruções com TV de [45].

	Haar		TV		Directional	
Images	SER_{dB}	SSIM	SER_{dB}	SSIM	SER_{dB}	SSIM
Shepp-Logan	135	1	114.9	1	28.7	0.98
Brain	39.2	0.420	37.4	0.516	31.5	0.369
Head	26.5	0.580	22.1	0.481	27.7	0.592

Conclusão

Neste trabalho, avaliamos diferentes estratégias para projetar filtros direcionais. Ao comparar o desempenho de todas as estratégias de filtros na reconstrução de uma imagem real da cabeça, os filtros do cenário III apresentaram melhores resultados em termos de qualidade de imagem quando comparados aos filtros de Haar. Relacionamos esse resultado com a capacidade dos filtros direcionais em extrair informações como limites, arestas, sulcos, texturas em diferentes orientações da imagem e, portanto, essa capacidade favorece a esparsidade em cada versão filtrada das medidas, portanto, simplificando o processo de resolução da minimização da lp para cada versão filtrada das imagens finais reconstruídas. Igualmente importante, as reconstruções a partir de medidas adquiridas em uma trajetória em espiral com crescimento exponencial apresentaram maiores resultados de SER e SSIM, mesmo com uma diminuição de 0,13% das medidas com relação à trajetória radial.

Palavras-chave: Ressonância Magnética, Compressive Sensing, Pré-Filtragem, Filtros Direcionais, Filtros Separáveis.

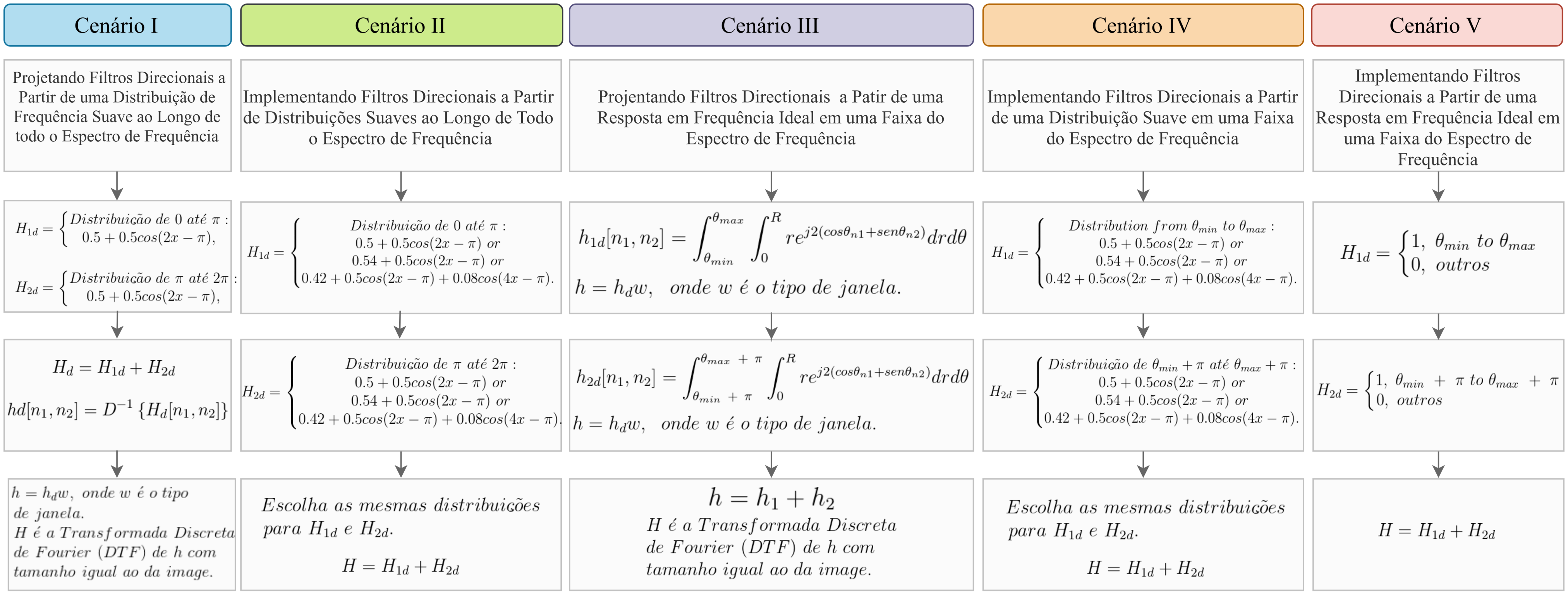

Figura 1. Resumo das etapas para projetar cada cenário dos filtros direcionais propostos.

Referências

[1] C. Andica, A. Hagiwara, M. Nakazawa, et al. The Advantage of Synthetic MRI for the Visualization of Early White Matter Change in an Infant with Sturge-Weber Syndrome. *Magnetic Resonance in Medical Sciences*, 15(4):347–348, 2016.

[2] E. Candès, J. Romberg, e T. Tao. Robust Uncertainty Principles : Exact Signal Frequency Information. 52(2):489–509, 2006.

[3] C. Dagia e M. Ditchfield. 3T MRI in paediatrics: Challenges and clinical applications. *European Journal of Radiology*, 68(2):309–319, November 2008.

[4] E. Dyrberg, E. Larsen, H. Hendel, et al. Diagnostic bone imaging in patients with prostate cancer: patient experience and acceptance of NaF-PET/CT, choline-PET/CT, whole-body MRI, and bone SPECT/CT. *Acta Radiologica*, page 028418511775128, 2018.

[5] J. Edmund e T. Nyholm. A review of substitute CT generation for MRI-only radiation therapy. *Radiation Oncology*, 12(1):28, dec 2017.

[6] N. Gorelik, S. Reddy, R. Turcotte, et al. Early detection of metastases using whole-body MRI for initial staging and routine follow-up of myxoid liposarcoma. *Skeletal Radiology*, 47(3):369–379, mar 2018.

[7] G. Grolez, M. Kyheng, R. Lopes, et al. MRI of the cervical spinal cord predicts respiratory dysfunction in ALS. *Scientific Reports*, 8(1):1828, dec 2018.

[8] T. Küstner, C. Würslin, S. Gatidis, et al. MR image reconstruction using a combination of compressed sensing and partial fourier acquisition: Espresso. *IEEE Transactions on Medical Imaging*, 35(11):2447–2458, November 2016.

[9] Z. Liang e P. Lauterbur. *Principles of Magnetic Resonance Imaging: A Signal Processing Perspective*. SPIE Optical Engineering Press, 2000.

[10] T. Liu, S. Wang, H. Liu, et al. Detection of vertebral metastases: a meta-analysis comparing MRI, CT, PET, BS and BS with SPECT. *Journal of Cancer Research and Clinical Oncology*, 143(3):457–465, March 2017.

[11] M. Lustig. *Sparse MRI.* Phd thesis, Stanford University, September 2008.

[12] M. Meier-Schroers, R. Homsi, D. Skowasch, et al. Lung cancer screening with MRI: results of the first screening round. *Journal of Cancer Research and Clinical Oncology*, 144(1):117–125, January 2018.

[13] C. Miosso, R. von Borries, e J. Pierluissi. Compressive sensing method for improved reconstruction of gradient-sparse magnetic resonance images. *Signal, System and Computers, 2009 Conference Record on the Forty-Third Asilomar Conference on*, páginas 799–806, 2009.

[14] C. Miosso, R. von Borries, e J. Pierluissi. Compressive sensing with prior information: Requirements and probabilities of reconstruction in ℓ_1-minimization. *IEEE Transactions on Signal Processing*, 61(9):2150–2164, 2013.

[15] Gian L. de O. Paiva. Comparação Objetiva de Imagens de Ressonância Magnética usando Compressive Sensing em Diferentes Estruturas de Decomposição Multinível. Dissertação de mestrado, Universidade de Brasília - Faculdade do Gama (FGA), 2017. Programa de Pós-Graduação em Engenharia Biomédica.

[16] J. Romberg. l_1-magic - Barrier iterations for equality constrained TV minimizaiton., October 2015. Available at https://statweb.stanford.edu/~candes/l1magic/. Last access: Jul 9$^{\text{th}}$, 2019.

Abstract

Compressive Sensing Using Directional Filters for Magnetic Resonance Image Reconstruction under Different k-Space Trajectories

Author: Jéssica Vivian Moreira da Silva
Supervisor: Dr. Cristiano Jacques Miosso
Post-Graduation Program in Biomedical Engineering
Brasília, June of 2019.

Recent research in Magnetic Resonance Imaging (MRI) shows improvements in diagnostic and early diagnostic for a wide range of pathologies and the superiority of the contrast for softy tissues when compared to other imaging techniques shows the applicability and importance of MRI exams. Even though the promising research, the MRI exam still face obstacles due to the time required to scan specific areas of the body and how this problem escalates with pediatric and claustrophobic patients. Research in Compressive Sensing (CS) showed positive results in terms of diminishing the number of measures and thus the time required for scanning the human body.

Although, these research showed positive results when implementing prefiltering with compressive sensing, they did not explore different scenarios, as directional filters and different trajectories. That being said, this research proposes five strategies in designing directional filters for prefiltering with Compressive Sensing. We show the mathematical steps adopted in each strategy and we reconstruct two phantoms and a real image of the head with several filters set for each scenario.

We also give an special attention to the quality indexes used to assess image quality and what they actually measure in terms of image fidelity. All the images were reconstructed from simulated measures acquired in a radial and spiral k-space trajectory using an Iterative Reweighted Least Square (IRLS) algorithm with prefiltering.

Finally, we showed that directional filters projected from ideal frequency response distributions and windowed by Hann, Hamming, Blackman and rectangular window present better Signal-to-Error Ratio (SER) and Structural Similarity Index Measure (SSIM) results for a real image of the head reconstruction when compared to the reconstruction of Haar filters.

Key-words: Magnetic Resonance Imaging, Compressive Sensing, Prefiltering, Directional Filters, Separable Filters.

Contents

List of Tables

List of Figures

List of Nomenclatures and Abbreviations

TR Repetition Time 6

TE Echo Time 6

PD Proton Density

SE Spin Echo 6

GE Gradient Echo 6

T_1 Spin-lattice Relaxation Time

T_2 Spin-spin Relaxation Time

G_{SS} Slice-select Gradient

G_{PE} Phase-encoding Gradient

G_{FE} Frequency-encoding Gradient

FID Free Induction Decay 11

IDTFT Inverse Discrete Time Fourier Transform 21

DTFT Discrete Time Fourier Transform 21

IRLS Iterative Reweighted Least Square 18

TV Total-variation 20

Chapter 1

Introduction

1.1 Research Topic

We live in the era of big data, the Internet of things, genetic enhancement, and genome recoding. However, visualizing the human body's internals and their functionalities is still challenging. A brief search over the most recent articles published from 2018 to 2019 on the field of medical imaging with Magnetic Resonance Imaging (MRI) on the data bases IEEE Xplore Digital Library, PubMed and Web of Science showed a collection of 50.574 studies regarding detection, segmentation, extraction, delineation, diagnosis and classification of the human body pathologies and physiological characteristics. To see the ten most relevant studies from each data base and the definitions of the articles search refer to the Tables 9, 10, and 11 in Annex C.

The prevalence of such studies indicates that researchers are directing their effort on being accurate and assertive regarding diagnosis, procedures and treatments. MRI has shown to be a powerful and flexible tool capable of generating images of many aspects of the human body [30]. It is well known mainly due to his softy tissue contrast superiority, which increases the diagnostic odds compared to other techniques as X-ray, radiography, and Computed Tomography (CT) [21, 32]. Also, MRI enables the use of a number of techniques and auxiliary devices to acquire high-resolution images useful in many phases of medical intervention [24, 27].

Recent research on MRI show improvements on diagnosing renal Angiomyolipomas Without Visible Fat (AML.wovf) [31], advances in early diagnosis of Sturge-Weber Syndrome (SWS), the detection of Myxoid Liposarcoma (MLS) metastases before clinical symptoms and pulmonary metastases, the prediction of respiratory disorders in Amyotrophic Lateral Sclerosis (ALS) patients, by revealing early cervical spinal cord atrophy [2, 24, 25], and the suitability of MRI on screening lung cancer and nodules with diameters above 6 millimeters [35].

A meta-analysis compiling works from 1995 to 2015 concluded that MRI is the best imaging modality for the diagnosis of vertebral metastases, when compared to other techniques such as CT, Positron Emission Tomography (PET), Single-photon Emission Computed Tomography (SPECT), and Bone Scintigraphy (BS) [32]. MRI is also suitable as a research tool, playing an important role in tractography, and in the mapping of brain regions and structural connectivity trajectory, which helps us to understand the human brain network functioning and which can thus lead to discoveries and advances on the treatment of neuro-degenerative diseases [47, 48, 3].

In radiotherapy planning, the accurate structural information and tumor delineation leads to a preference regarding MRI over CT images [41], although several radiotherapy services still rely on CT for treatment planning due to economical and time constraints.

New strategies in MRI acquisition and reconstruction show promising advances in fetal cardiac imaging, in the prediction of growth restriction and birth weight despite of maternal and fetal motion [49, 18, 33]. MRI is also being applied in radiofrequency ablation tests, eliminating the use of an external Radiofrequency (RF) generator and allowing real-time monitoring of the ablation progress. Also, in ablation treatments MRI allows one to gather more data on the impact suffered by different tissues [27].

Even though the MRI scenario is promising regarding new applications and techniques related to the choice of RF pulses and acquisition trajectories, the exam still faces complications and issues related to patient acceptance. In fact, the exam takes from 45 to 60 minutes per body part [40], and the patient has to be still for a long period of time, frequently in very uncomfortable positions. This is specially challenging in the case of pediatric patients, and this sometimes requires sedation or general anesthesia. Such procedure however involves risks and needs specialized staff and monitoring equipment [17]. Another challenging case is that of claustrophobic patients, for whom sometimes the exam ends up not being a viable option, especially when the patients need to be aware and responsive, so anesthetics cannot be administered [20].

In order to reduce the total exam time, image reconstruction techniques based on Compressive Sensing (CS) have been developed and they have had positive results concerning the number measurements in the k-space domain [34, 11, 38, 28]. Recent research using prefiltered images have shown favorable results related to time of reconstruction, number of required measurements and image quality [37, 16, 1]. These research, however, did not inspect possible relations between different trajectories in k-space domain and prefiltering. In addition, to our best knowledge, they still did not explore directional filters and their ability to extract high frequency components in separate directions, which could potentially improve reconstruction by providing sparser filtered images.

In [34], the author discussed how an evaluation can be conducted in order to determine an appropriate sparsifying transform for a specific type of k-space trajectory. Additionally, in [42] the prefiltering technique is tested with a variety of filters' families, all of them corresponding to nondirectional frequency responses. Nonetheless, we did not find systematic studies performed on the prefiltering strategy under different scenarios, meaning with different trajectories and directional filters. Since different trajectories can show different results in terms of signal sparsity, and filtering those same measurements can alter the corresponding image's sparsity, the reconstruction algorithms may suffer a change in performance depending on the relation between the trajectory and the chosen filters. In addtion, the sparsifying potential of the directional filters was not systematically tested along with prefiltering in Compressive Sensing.

1.2 Research Question and Contributions

In the context of the research gaps related to prefiltering in Compressive Sensing, this research proposes a systematic evaluation of the use of directional filters combined with different trajectories, and the study of their influence on reconstructed image's quality, number of required measurements, and algorithm performance. Also, we aim at exploring different strategies to implement the directional filters. The motivation is that different strategies to build a filter with a certain frequency specification can lead to major changes in terms of the filtered measurements and the impact on the reconstruction quality.

In order to achieve these outcomes, we will simulate Magnetic Resonance (MR) measures under different trajectories. Also, we will use digital phantoms and MR images to help us quantify the relation between the filters and different trajectories. We also want to perform statistical tests in order to evaluate the hypothesis of quality enhancement when prefiltering with determined trajectories.

In this research we address the following questions:

1. What are the improvements in the Signal-to-Error Ratio (SER) in MRI reconstruction when using prefiltering in the measurement domain with directional filters?
2. Which trajectory shows better results for a specific filter or set of filters?
3. What is the difference in the directional filters' results compared to results in the scientific literature?
4. How significant and reliable are the findings and results in terms of the number of measures, reconstruction time, and image quality?

1.3 Objectives

1.3.1 General Objectives

This research aims at evaluating the sparsifying potential of directional filters and how much they affect the final reconstructed image when using CS with prefiltering. The main goal is to study some filter characteristics and how they impact the image sparsity and compared to Haar filters, which were used in the first prefiltering strategies. The hypothesis is that directional filters may produce sparser images, since they can extract high frequency components in specific directions, as in the case of ridges, lines and edges. This study attempts to identify some required characteristics of sparsifying filters and how they relate to different trajectories.

We will design and implement different directional filters in this research, and they will be compared between each other and to the Haar filters results provided by [37], in terms of image quality and reconstruction time. Also, the filters will be tested under different k-space trajectories.

1.3.2 Specific Objectives

- Design and implement directional filters with different techniques in order to compare the sparsifying potential of each filter family.
- Evaluate the designed directional filters under different k-space trajectories and with different numbers of measurements.
- Compare the directional filters to the results obtained with Haar filters.
- Evaluate the results of the tested directional filters, when compared to the Haar filters in terms of quality indexes.

Chapter 2

Theoretical Foundation and State of the Art

This chapter describes the basic theory used in this research and the state of the art regarding techniques to reconstruct MR images from measurements in the k-space domain. Section 2.1 is a brief explanation of the fundamentals of Magnetic Resonance Imaging and the standard reconstruction methods used in clinical MRI scans. Finally, Section 2.3 explains the fundamentals of Compressive Sensing as well as the reasons why it is a promising method when combined with prefiltering.

2.1 Magnetic Resonance Imaging

There are many ways to describe the theory of MRI and in this work, we will adopt the theory sequence described in [46], which we consider more intuitive as a first introduction as well as an interesting approach to someone already acquainted with the subject. We also adopt the classical description [30, 6, 5].

2.1.1 What is seen in MRI images?

To answer this question a good approach is to classify the body tissues into three categories:

I - Fluids: Cerebrospinal Fluid (CSF), synovial fluid, edema;
II - Water-based tissues: Muscle, brain, cartilage, kidney;
III - Fat-based tissues: Fat, bone marrow.

In Figure 2.1, one can observe that these types of tissues differ from each other by the level of grey. This difference in grey levels associated to different tissues is defined as the image contrast. Indeed, the MR scan is able to measure some tissue property, as we will describe, and associate it to a proportional level of grey, thus allowing us to see the boundaries between the organs and pathological tissues, which frequently have edemas

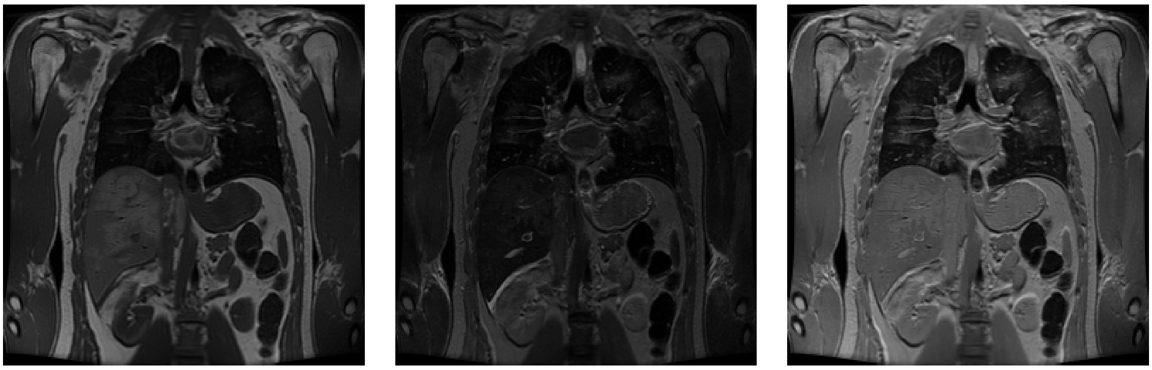

(a) T_1 image. **(b)** T_2 image. **(c)** PD image.

Figure 2.1. Coronal magnetic resonance images of a human abdomen, taken from the Visible Human Project [43]. The contrast varies in each figure as a result of the physical characteristics (T_1, T_2 or PD) measured after the stimulation of the tissue cells with RF pulses as well as magnetic spatial gradients.

or proliferating blood supply. This characteristic makes them appear as a mixture of water-based tissues and fluids on the MR images.

MRI scans provide a wide range of contrast by applying different RF pulse sequences and gradient pulses (we will get to them in the following sections). The challenge is to set the right RF pulse sequences that will provide an appropriate level of contrast between types of tissue that one wants to distinguish, for example normal tissues opposed to pathological ones. Those sequences are normally already defined in the scan configuration and they have carefully controlled timings and durations. Even though there are infinite possibilities of pulse and gradient sequences, they all have timing values called the Repetition Time (TR) and the Echo Time (TE). Also, each configuration of pulse sequence is designed in a manner as to enhance a part of the tissue we want to depict. In this context, T_1, T_2 and PD are the physical properties that an MR scan measures and codes in the form of image brightness.

Depending on the kind of tissue we want to image there is a specific set of pulse sequence that will produce a signal with high intensity and consequently an image with better contrast. There are two main types of pulse sequences, Spin Echo (SE) and Gradient Echo (GE). For each sequence there is a specific technique related to timings and the flip angle. Section 2.1.2 contextualize the sequence of pulses and gradients applied to the human body in order to select a region and to provide an image of that area.

2.1.2 How is the MR data encoded and stored?

Based on the relation between T_1, T_2 and PD and the grey levels in the image, we now consider the shape of the pulse sequence and how each element of volume in the body (*voxel*) is excited and them have their timings *measured* by coils in the MRI scan. Also, the same coils are used to apply the pulses and gradients at a certain degree in specific times (TE and TR). Here we explore the gradient echo sequence focusing on how it manages to localize the MR signal coming from the tissue. Figure 2.2 shows the pulses arrangement.

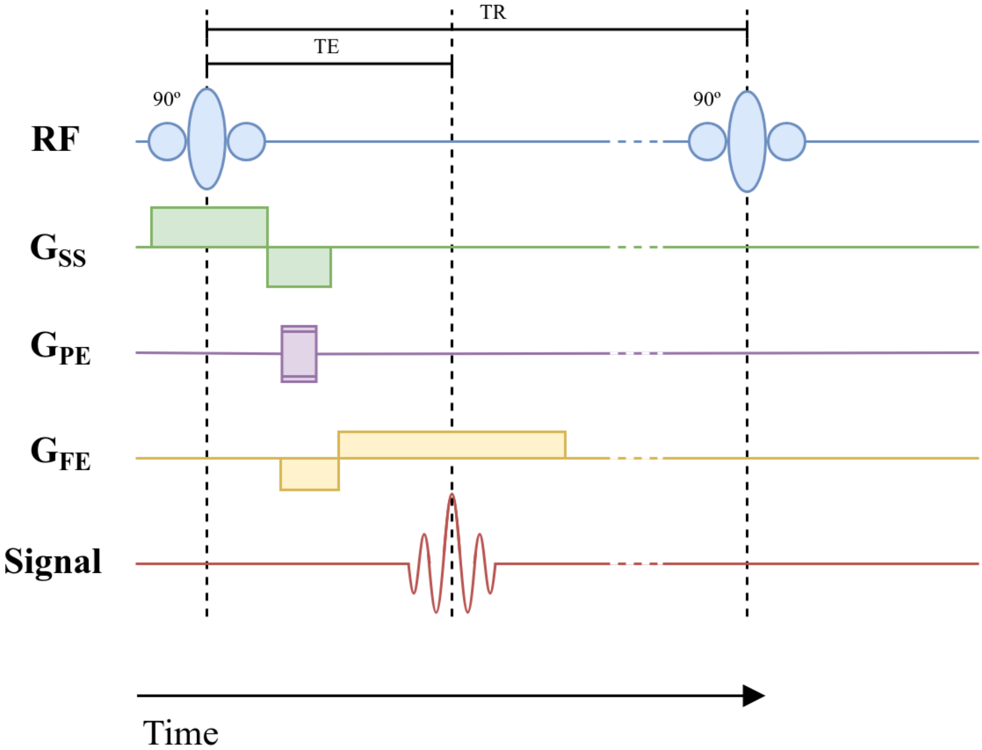

Figure 2.2. Diagram representing the pulses and gradients over time used in the gradient-echo setup, in MRI. The first line represents the RF pulse applied at the angle of 90°. At the same time there is the G_{SS} and at the end of the RF pulse the direction of the G_{SS} is reversed. The G_{PE} is applied between the duration of the reversed G_{SS}, as well as the reversed G_{FE}. The positively directed part of the G_{FE} is applied at the end of G_{SS}. TE is a measure of time between the RF pulse and the signal coming from the tissue that is excited. TR is a measure of all the process including application of pulses and measure of the MR signal. This process is repeated many times depending on the size and resolution of the final image.

Spatial Encoding

For each voxel we want to establish a particular resonance frequency and for that we have to apply a G_{SS} alongside with the RF pulse. The RF pulse excites the tissues and the G_{SS} selects the plane of the resulting image. Combinations of the gradients G_x, G_y and G_z are used to create images of the body planes (sagittal, transverse and coronal) as in Figure 2.3. A G_{PE} is applied in 90° from the G_{SS} gradient direction. Suppose that we are acquiring a coronal image, so the slice in the z-axis is encoded by G_{SS} and the directions x and y are then encoded by using the phase and frequency of the signal returning from the tissue. The G_{FE} is applied at the same time the coils receive the MR signal from the tissue. The gradient used to encode the x and y axes are arbitrary, which means that we can encode the frequencies in rows or columns, since the analogous is chosen for the phase. In this example the G_{PE} will encode the x-axis (columns), and the G_{FE} will encode the y-axis (rows).

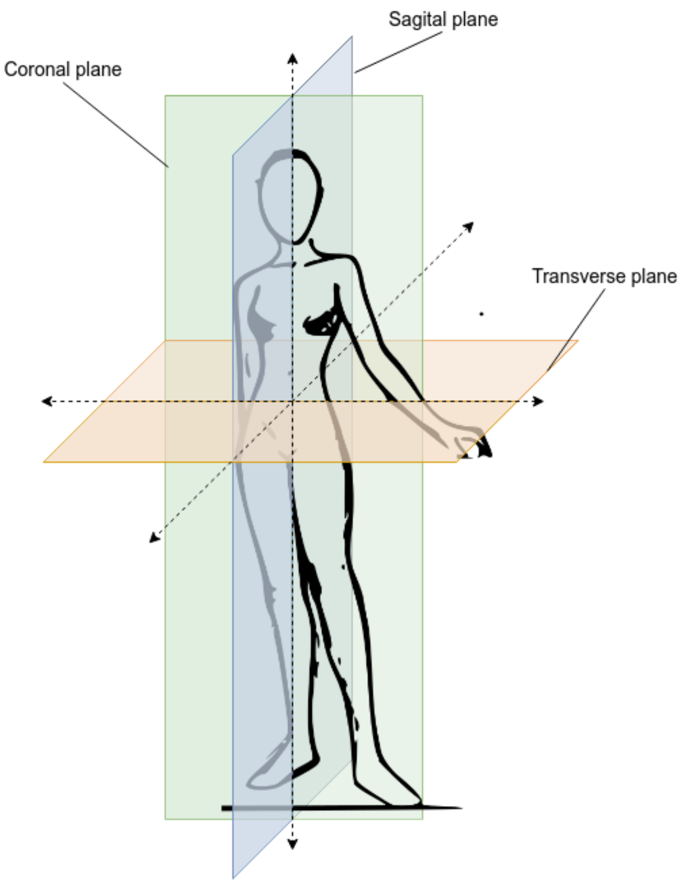

Figure 2.3. Anatomical planes. Image modified from [7]. In order to conduct the MRI acquisition process we use the anatomical planes to place the pulses and gradients at the right directions and acquire images from different perspectives.

The signal acquired here has two sets of data (phase and frequency) and we want to be able to acquire this information as a single set. We can do it by Fourier Transforming our signal, which allow us to collect the data as an individual set of complex data. The MR signal acquired as a function of time is then mathematically represented as a function of frequency. The process represented by the diagram in Figure 2.2 is repeated a certain number of times and the average of the results is stored. This is done to decrease the relative contribution of noise in the signal.

After that, we change the magnitude of the G_{PE} gradient and reapply all the pulse sequence. The number of times this process is repeated determines the number of columns of the slice. We do it because the G_{PE} does not offer enough information to differentiate the columns in the slice. A second Fourier transform is applied, after all phase-encoding steps are completed in order to fill a matrix of data (k-space matrix), to relate phase and position as a Fourier transform pair. This process is time consuming, with the total scan time given by the product of multiplication

$$ST = N_A \cdot N_{PE} \cdot TR, \tag{2.1}$$

where N_A is the number of signal averages, N_{PE} is the number of phase-encoding gradients applied, and TR is the pulse repetition time.

In fact, if we wanted to acquire all data from all voxels in the slice selected it would take days, which is not feasible for medical and clinical circumstances. To contour this situation we sample the signal following trajectories in the k-space and apply a series of mathematical techniques to reconstruct an image from the sampled data. If we had all the measurements from all voxels, we would only make an inverse Fourier transform to acquire the MR image. Some of those techniques used to reconstruct an image from samples of the k-space are, spectral interpolation, which consists in interpolating the frequency domain in order to obtain measurements in a cartesian mesh and then to calculate an inverse transform to reconstruct a MR image. Other technique widely used is, the filtered back-projection, applied in tomography but also in MRI for the case where the data is measured using a radial trajectory. For this case, the projection slice theorem relates Fourier to the measurements in linear projections and the back-projection filtering process allows to calculate the image. This technique consists in filtering projections in the frequency space using a ramp filter, performing an inverse transform and back-projecting it to create the final image. A promising technique, called Compressive Sensing, is discussed in the Section 2.3 and we will explain some of the advantages and challenges of its application in MRI.

2.2 MRI Physics and the Bloch Equation

The ability to image the human body relies on the possibility of using pulse sequences to excite the body particles and then to measure the effects of different set of pulses. This is feasible due to the behavior of atoms nucleus with odd atomic number that have an angular momentum, called spin. An abundant atom in the human body with odd atomic number is hydrogen, see Table 2.1. Naturally, the spins of the atoms are oriented in random directions, but once they are affected by a strong magnetic field they tend to align in the same direction of the field.

In order to measure an MR signal, we not only apply a sequence of pulses but also a strong field B_0 in the z-direction, that works as a reference from where the spins start to move. This field remains in all the process to acquire the MR signal from the tissue. Besides the angular momentum, the spin also precesses about the magnetic field direction, see Figure 2.4. This movement results from the interaction of forces with a rotating object. The relationship between the frequency f (in megahertz, MHz) of precession and

Table 2.1. Biological abundance of some elements studied in medical imaging. Values calculated from the Source: [22, 26].

Element	Biological Abundance (%)
Hydrogen	63
Carbon	9.4
Nitrogen	1.5
Sodium	0.041
Phosphorus	0.24
Calcium	0.22

the strength B (in tesla, T) of the magnetic field was found from experiments and given by the Larmor equation, which states that

$$f = \gamma B, \tag{2.2}$$

where γ is the gyromagnetic ratio, equal to 42.58 MHz T^{-1}. Since there are so many protons, what we actually measure is the average magnetic moment of a large group of protons in the magnetic field that precess at nearly the same Larmor frequency. The spins can be in two possible states, one is known as spin-up or parallel and is aligned to the magnetic field, the other is spin-down or anti-parallel. There is a statistical distribution for the two states and the lower state, spin-up, is slightly favored. The sum of all those spins is the net magnetization $M_{(t_0)}$ in the same direction as the field B_0. When the longitudinal component M_z of the magnetization is equal to $M_{(t_0)}$ and there is

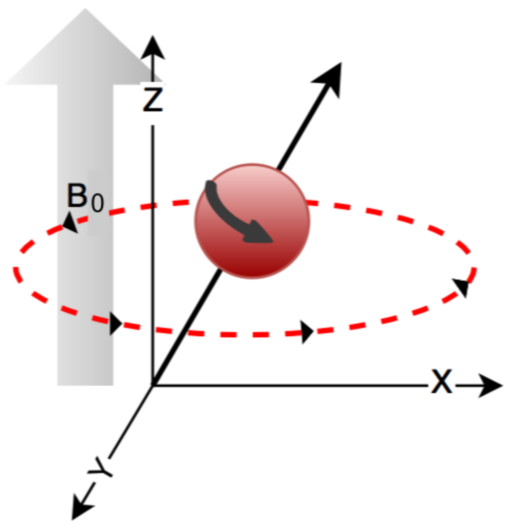

Figure 2.4. Geometric representation of a spin precessing about the B_0 field. The red ball representes the spin and the curved arrow around it, represents its natural movement around itself. The bigger arrow crossing the ball indicates the state of the spin, alligned with the B_0 field, in a positive direction related to the tridimensional plane. The red dashed circle with arrows indicates the direction of the precessing movement.

no transverse magnetization in the x and y directions, we say the system is in equilibrium. It is possible to change the magnetization of the system if we expose it to a RF pulse with a frequency equal to the energy difference between the states of the spins. If sufficient energy is applied, it is possible to saturate the spin and make $M_z = 0$. The time constant describing how M_z returns to its equilibrium ($M_{(t_0)}$) is the, already know, relaxation time T_1, and is given by

$$M_z = M_{(t_0)}(1 - e^{-t/T_1}), \tag{2.3}$$

which is an exponential growth with time constant T_1.

If a magnetic field is applied in the xy direction, the magnetization vector will rotate around the z-axis at the Larmor frequency, equal to the frequency of the photon, which leads to the transition between energy levels of the spins. This rotation will at some point begin to lapse because each subsystem of spins begins to perceive the influence of a different magnetic field and this delay will be higher depending on the duration of the pulse applied. The influence of the pulse in the transverse magnetization at xy is described by

$$M_{xy_{(t_1)}} = M_{xy_{(t_0)}} e^{-t/T_2}, \tag{2.4}$$

where the relaxation time T_2 is the constant that describes how long the transverse magnetization of the spins system takes to return to the balance. As the interaction between spins occurs more rapidly, T_2 is always smaller in relation to T_1, since $T_1$is slower due to the difficulty that larger cells have in moving and dissipating energy. The curve presented in Figure 2.5 represents exponential growth in M_z compared to the exponential decay of M_{xy}, which occurs more quickly due to time constant T_2. This behavior is described as Free Induction Decay (FID), that is the tendency of the spins to return to equilibrium after suffering disturbances.

Since now we know how the spins work as a system and how a pulse sequence is applied to extract the MR signal from the tissue, the following image, Figure 2.6 summarize the process of imaging a certain area of the human body. First, we apply a B_0 field that will align the spin system in the z-plane, after that we apply a G_{SS} gradient to select the plane we want to image. In the region where G_{SS} is applied the Larmor equation is valid and we can excite the region with gradients as G_{PE}, G_{FE} or RF pulses, that depends on the sequence we are using. The following steps where already described in the Section 2.1.2. Each sequence of gradient and RF pulses are used to enhance the MR signal from determined tissue, also some of they take in account the PD, since the number of protons affect directly in magnetization.

The behavior of these magnetization curves can be described by means of the phenomenological Bloch equation. In fact, if **B** is the effective magnetic field (including the static component and the desired perturbations) at a certain position, **M** is the magnetic

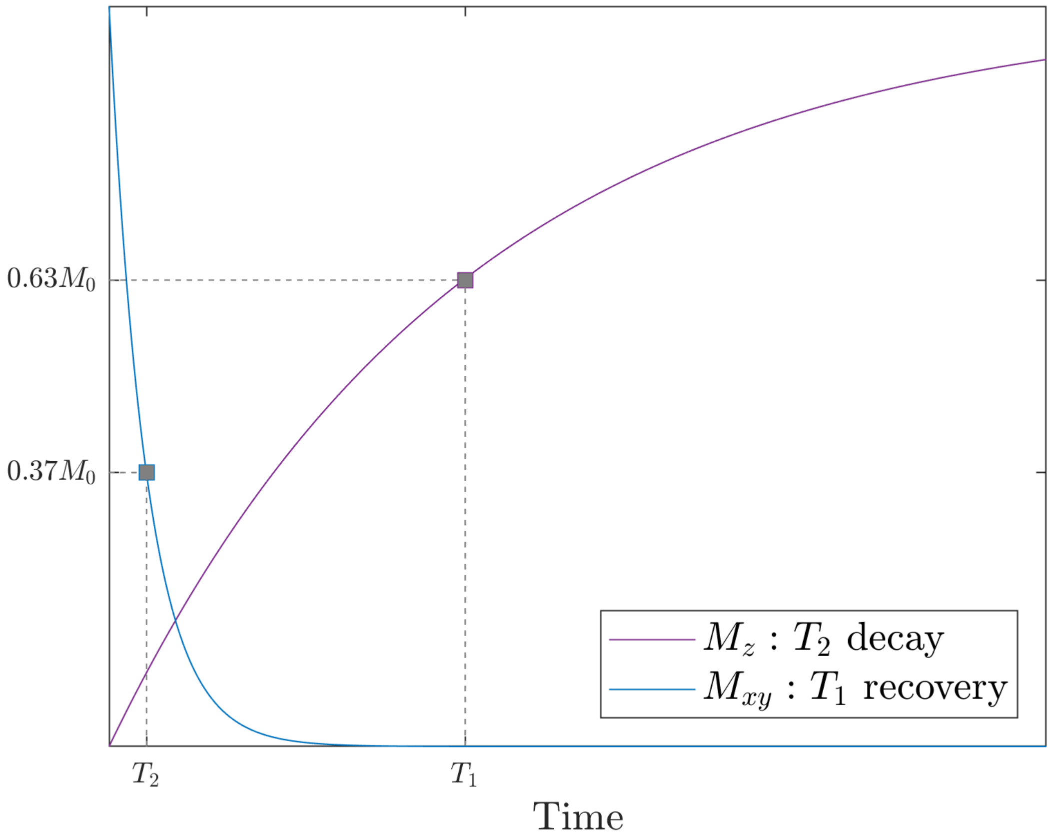

Figure 2.5. Magnetization curves M_z and M_{xy}. The blue curve represents the magnetization decay in the xy direction. T_2 is measured at 37% of the equilibrium magnetization value in the M_{xy} curve. The purple curve represents the magnetization increase in the z direction. Similarly, T_1 is measured at 63% of the equilibrium magnetization value in the M_z curve.

moment at the same position and $\overrightarrow{i}$, $\overrightarrow{j}$, $\overrightarrow{k}$ are the unitary vectors in the x, y, and z directions, respectively, then the phenomenological Bloch equation establishes that

$$\frac{d\mathbf{M}}{dt} = \gamma \boldsymbol{M} \times \mathbf{B} - \frac{M_x(t)}{T_2}\overrightarrow{i} - \frac{M_y(t)}{T_2}\overrightarrow{j} - \frac{M_z(t) - M_0}{T_1}\overrightarrow{k}, \tag{2.5}$$

$$\boldsymbol{M} \times \mathbf{B} = \begin{bmatrix} M_y(t)B_z(t) - M_z(t)B_y(t) \\ M_z(t)B_x(t) - M_x(t)B_z(t) \\ M_x(t)B_y(t) - M_y(t)B_x(t) \end{bmatrix}, \tag{2.6}$$

where γ is the gyromagnetic ratio, M_z is the longitudinal magnetization component,

M_x and M_y are the transverse magnetization components, M_0 is the magnetization of equilibrium, and T_1 and T_2 the spin-lattice relaxation time and the spin-spin relaxation time.

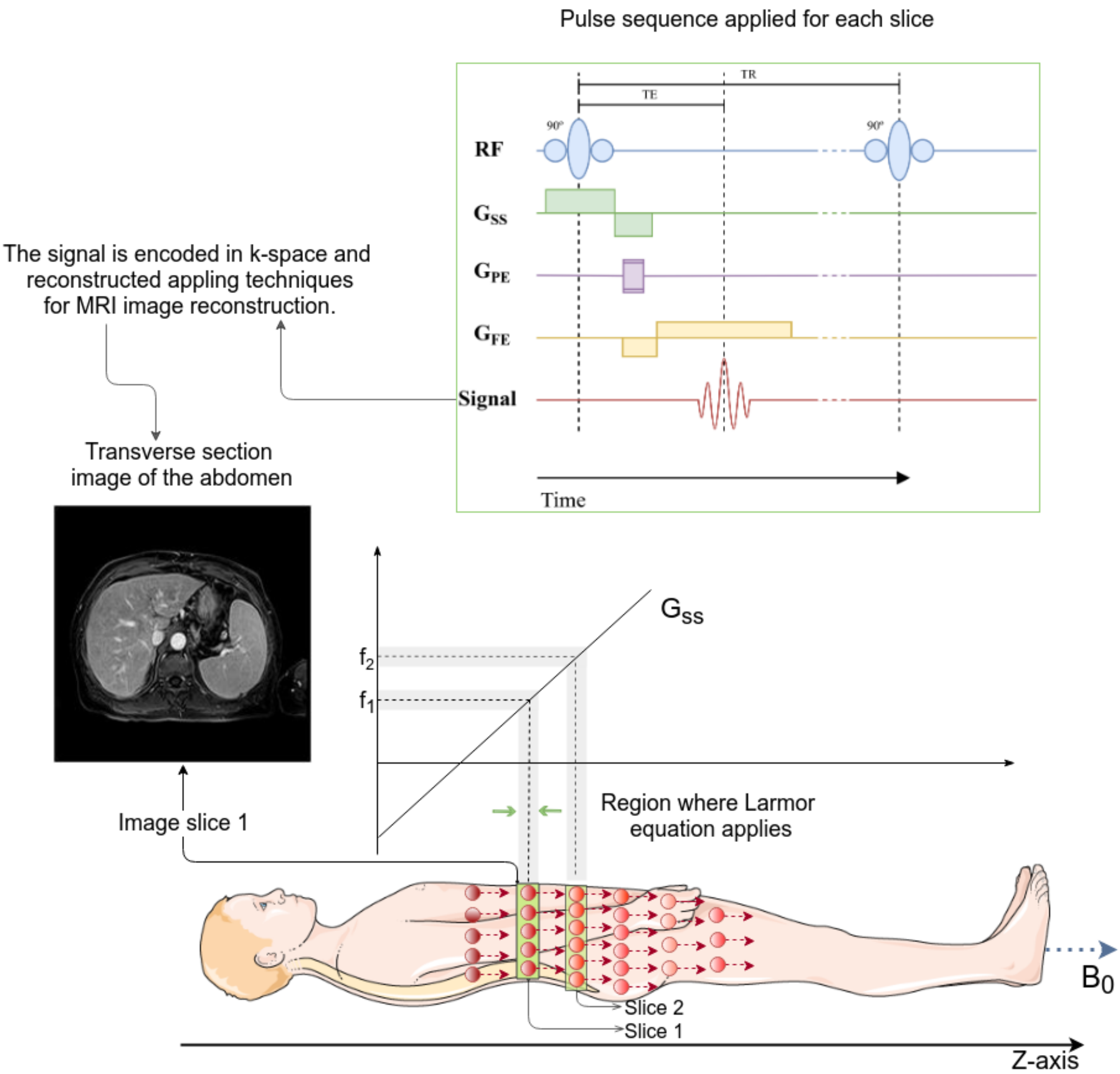

Figure 2.6. MR signal acquisitionon process for a transverse image of the abdomen applying a gradient echo sequence. The red balls represent the spins of the protons aligned with the B_0 field. Notice that the protons have different colors and it is an attempt to represent their different characteristics concerning each tissue which results in different times (T_1 and T_2), also the PD is different and that is why the number of protons differ around the body region imaged. The cross sectional image of the abdomen is from the Sansum Clinic [15]. Human body in supine position modified from [8].

By expanding the vectorial product in (2.5), it is also possible to rewrite the Bloch equation in terms of three spatial components, given by

$$\frac{dM_x(t)}{dt} = \gamma(M_y(t)B_z(t) - M_z(t)B_y(t)) - M_x(t)/T_2; \tag{2.7}$$

$$\frac{dM_y(t)}{dt} = \gamma(M_z(t)B_x(t) - M_x(t)B_z(t)) - M_y(t)/T_2; \tag{2.8}$$

$$\frac{dM_z(t)}{dt} = \gamma(M_x(t)B_y(t) - M_y(t)B_x(t)) - (M_z(t) - M_0)/T_1. \tag{2.9}$$

With appropriate limiting conditions those equation can be solved for different circumstances that describe the changes in the magnetization during excitation and relaxation. For the special case in which, $B_x(t) = B_y(t) = 0$ and $B_z(t) = B_0$, the equation can be expressed as:

$$\frac{dM_x(t)}{dt} = \gamma(M_y(t)B_0) - M_x(t)/T_2; \tag{2.10}$$

$$\frac{dM_y(t)}{dt} = -\gamma(M_x(t)B_0) - M_y(t)/T_2; \tag{2.11}$$

$$\frac{dM_z(t)}{dt} = -(M_z(t) - M_0)/T_1. \tag{2.12}$$

2.3 Mathematical Principle of Compressive Sensing

Compressive Sensing (CS) is set of theories and methods for reconstructing signals from highly limited linear measurements, possibly acquired below the Nyquist rate, making use of numerical optimization and exploring the existence of a sparse representation in some domain.

The mathematical foundation of CS was initially developed by Donoho, Candès, Romberg, and Tao [11, 12, 19]. Basically, CS can be applied when we have only m samples or linear measurements of a signal x and we want to be able to obtain all the l samples of the signal, with $m < l$. Thinking of MR images, we want samples of the MR signal to fill the whole k-space, so that in Figure 2.7, $x_{l\times1}$ is a staked version of the desired image matrix, but we can only acquire a few samples ($b_{m\times1}$) of the matrix, due to hardware, physiological, and physic constraints. Our problem can be stated as computing x based solely on

$$b = Mx. \tag{2.13}$$

with M a matrix with fewer rows than columns, so that (2.13) is undetermined. Note that under this condition, we need additional information in order to solve the system, and in CS this piece of information refers to sparsity. Starting from a unknown x, we can affirm that there is a transformed version of x that is sparse. In other words, there is a invertible $T_{l\times l}$ that can be applied to x and results in a sparse vector. In this context, T is called the *sparsifying* matrix, so that

$$\hat{x} = Tx, \tag{2.14}$$

is a vector that has most part of its components null or, in practice, fairly close to zero under a tolerance. Note that, since $\hat{x}$ is sparse, even with less measurements m, only a solution whose transform T is sparse is a valid solution.

Therefore, our problem is represented with the following restriction:

$$MT^{-1}\hat{x} - b = 0, \tag{2.15}$$

where M is a mxl matrix, which represents the acquisition process in the k-space, so that (M) is a submatrix of the Fourier matrix.

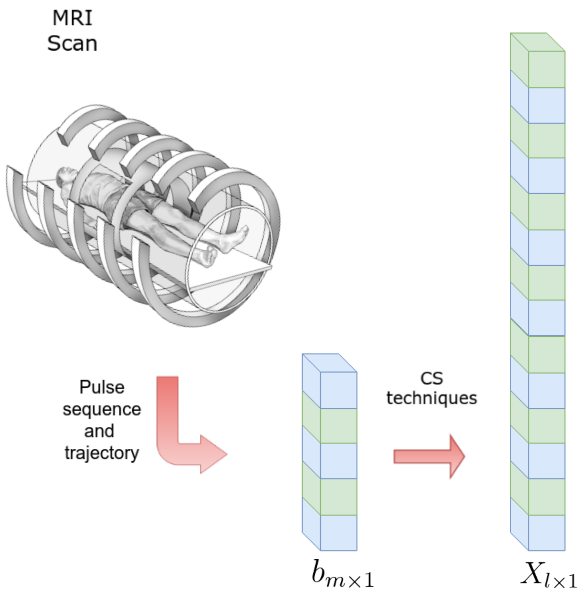

Figure 2.7. Illustration of MRI signal sampling acquisition. The pulse sequence and specially the trajectories have a effect on the k-space matrix. The first column represents the measurements $b_{m\times1}$ acquired after applying techniques concerning pulse and trajectory sequences to obtain the MR signal. Apling techniques of image reconstruction, as CS, we are then able to obtain all the measurements $X_{l\times1}$ needed to represent the signal as an image. The MRI scan figure is modified from [39].

By this point, CS becomes a problem of optimization with restrictions. Ideally, we want to find the sparsest version of $\hat{x}$, which is to minimize the number of non-zeros in $\hat{x}$, process called l_0 of $\hat{x}$ and expressed as $\|\hat{x}\|_0$. However, this problems is known as NP-hard, because requires an enumeration of all $\binom{l}{\eta}$ possible locations of the non-zeros in $\hat{x}$, where η is the number of non-zeros, or sparsity of the signal [4, 36]. In particular, the theory of CS proposes some conditions and theorems that implies m to be high enough with η, for which there will be only a x satisfying Equation (2.13) and also $\|\hat{x}\|_0 << \eta$ [10, 11, 34]. As a result, one possible option is to find the minimum l_1-norm by solving

$$\min_{\hat{x}} \|\hat{x}\|_1, \quad subject\ to\ A\hat{x} - b = 0, \tag{2.16}$$

where $A = MT^{-1}$. When searching for the sparse solution, we are looking for the intersection between the solution space and the axis. One way of visualizing it is to start from the center and to expand until it reaches the intersection in the solution space, as is shown in Figure 2.8 for different values of p.

For the case where we try to solve the l_2-norm, there is a close form solution (least square), however, solving it means to find the minimum energy solution and in general, it is not the sparsest solution. Similarly, finding the solution for the l_1-norm has bigger probabilities to find the sparsest solution when compared to l_2, whereas, there is no closed form solution for that case, but there is a solution based in convex optimization, since the problem is of polynomial complexity. In a like manner, we can solve the l_p-norm for $p < 1$ and in some cases, it shows better results than the l_1-norm, at the cost of computational effort, but less measurements when compared to l_1.

For a perfect reconstruction the M matrix has to satisfy certain criteria, known as necessary and sufficient conditions. The conditions are listed below:

I - Restricted Isometry Property (RIP) M is such that $\forall$ signal v_{lx1} with no more than 3η non null entries, RIP states that

$$1 - \epsilon \leqslant \frac{\|MT^{-1}v\|_2}{\|v\|_2} \leqslant 1 + \epsilon, \tag{2.17}$$

where $\epsilon > 0$ and the smaller the ϵ the easier to meet the conditions, because the matrix preserves the Euclidean length of the vector v, which indicates that it is not in the null space of MT^{-1} [9].

II - Incoherence: The rows of M cannot be sparse in the transformed domain defined by T. Which means that, the transform used to sparsify x cannot sparsify the rows of M [13]. The relation of coherence (μ), with m samples for Partial Fourier is given by

$$m \geqslant C.\mu.\eta(log(n))^4, \tag{2.18}$$

where C is as small as ϵ in the RIP.

2.3.1 Optimization algorithm

In [23] Foucart discuss a series of algorithms for CS based on optimization. The algorithms are Basis pursuit and Quadratically constrained basis pursuit. The first one is an attempt to solve the l_1-norm as Equation in 2.16, the other method is also called noise-aware l_1-minimization, where the constrain takes in account a tolerance for the scenarios with noise. The problem is described as

$$\min_{\hat{x}} \|\hat{x}\|_1, \quad subject\ to\ \|A\hat{x} - b\|_2^2 \leqslant \eta, \tag{2.19}$$

The cases for l_p with $p < 1$ where studied by Rao and Kreutz-Delgado [44], where they substituted the objective function in the l_p-minimization by a weighted l_2-norm, where the weights are computed from a previous interaction. The approach here is to solve a

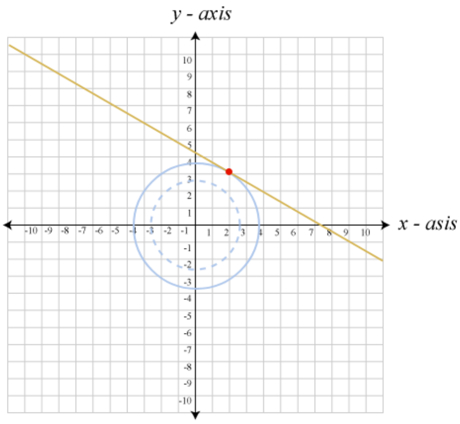

(a) $p = 2$.

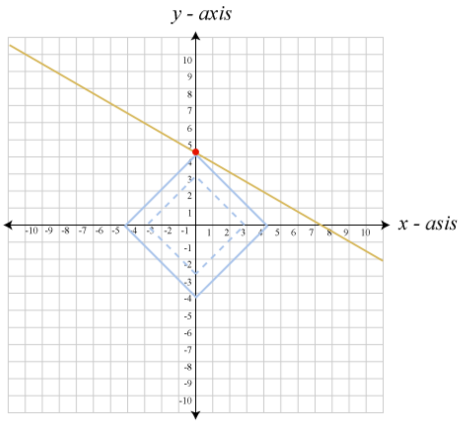

(b) $p = 1$.

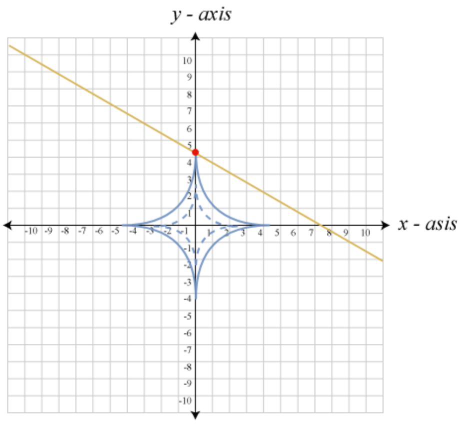

(c) $p = \frac{1}{2}$.

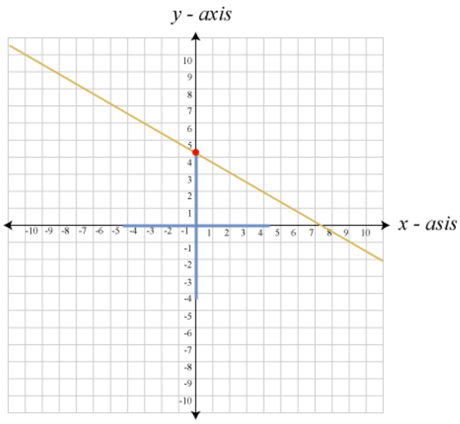

(d) $p = 0$.

Figure 2.8. Visual example of the lp-minimization solution to a set of underdetermined equations. The strait line represents all the points satisfying all the infinite points of the equation $Ax = b$, with $A_{1\times2}, x_{2\times1}, b_{1\times1}$. The concave closed curves are examples of lp-balls, corresponding to complete set of points with the same lp-value. By increasing lp and thus the corresponding lp ball until this ball touches the straight line we identify a solution to $Ax = b$ with minimum lp, here represented by the red dot. This illustrates the fact that minimizing the lp with the constraint $Ax = b$ may yield a sparse solution to the underdetermined system, as required by CS. The figure **(a)** represents the lp-minimization solution for $p = 2$, for this problem there is a closed form solution called least-square. The smaller the value of p more precise is the solution, however, it means that we will need more measurements or more computational power. For $p = 1$, figure (b), the solutions adopted require more measurements compared to solving l_2-norm. For values of $p < 1$, figure (c), a possible solution is IRLS, where the smaller the p more computationally demanding the solution will be. The ideal solution would be by solving l_0, as in figure (d), however this process is known as of NP-hard complexity and its solution requires years of computational effort to find a single solution, what is unsuitable for MRI

modified version of

$$\min_{\hat{x}} \frac{1}{2} \|\hat{x}\|_p^p, \quad subject\ to\ A\hat{x} - b = 0, \tag{2.20}$$

by solving

$$\min_{\hat{x}} \frac{1}{2} \sum_{n=1}^{N} w_n |\hat{x}_n|^2, \quad subject\ to\ A\hat{x} - b = 0 \tag{2.21}$$

Where $w_n = \left|x_n^{k-1}\right|^{p-2}$. This methods is called Iterative Reweighted Least Square (IRLS) and is a powerful algorithm applied in CS, with the advantage that for different values of p it is possible to use the same algorithm by only changing one single parameter. The algorithm utilized here has a stage of prefiltering before every reconstruction and a composition stage, as described in Section 2.3.2. Next, we present the algorithm used in this work and based on [36, 14, 37].

Algorithm 1 Signal Reconstruction in Compressive Sensing Using IRLS and Prefiltering

Inputs: $p > 0$, A, b, H, μ

First: Calculate the n filtered versions bf_n of b using (2.22).

Loop 1: Reconstruction of the n filtered versions of $\hat{x}$: For 1 to n

Second: Initialize $\hat{x}f_n^{(0)} = Q^{(0)}A^T(AQ^{(0)}A^T)^{-1}bf_n$ and $Q^{(0)} = I$(identity matrix).

Loop 2: Inner loop: Start $m := 1$;

2.1 Compute $Q^{(m)} = diag(q_1^{(m)}, q_2^{(m)}, ..., q_N^{(m)})$, where $qk = \left|\hat{x}f_{n(k)}^{(m-1)}\right|^{2-p}$;

2.2 Calculate $\hat{x}f_n^{(m)} = Q^{(m)}A^T(AQ^{(m)}A^T)^{-1}bf_n$;

2.3 If $\frac{\left\|\hat{x}f_n^{(m)} - \hat{x}f_n^{(m-1)}\right\|}{1+\left\|\hat{x}f_n^{(m-1)}\right\|} \leqslant \frac{\sqrt{\mu}}{100}$ **then**

Go to **Third**;

else

$m := m + 1$;

End Loop 2

Third: Update the regularization parameter, $\mu := \frac{\mu}{10}$;

3.1 If $\mu < 10^{-8}$, **end** iterations of *Loop 1*;

else

Go to **2.1**;

End Loop 1

Loop 3: For 1 to n

Fourth: Xf_n *is the DFT of* $\hat{x}f_n$

4.1 If $|H_n| > tolerance$ **AND** $|H_n| >$ than all $\left|H_{(n-1)}\right|$

$Xr = \frac{Xf_n}{H_n}$

End Loop 3

xr *is the IDFT of* Xr.

2.3.2 Prefiltering for Image Reconstruction in Compressive Sensing

Compressive Sensing with prefiltering consists in using filters before computing the l_1 or l_p to find filtered versions of the MR desired image. In some studies, it has been shown that the use of prefiltering with Haar filters at one level has improved the quality of the reconstructed image relative to other methods [37]. The idea is to choose the filters in such a way that they increase the image sparsity in the pixel domain. The prefiltering is performed by means of 2D filters, which are created from 1D filters after the external product between two filters. The filtered versions of b are calculated from

$$b_f = H_{k\in\tau} \circ b, \tag{2.22}$$

where $\circ$ is the element-by-element product and $H_{k\in\tau}$ is the staked version of the filter H in the trajectory τ of the k-space samples. In addition, the filtered versions are computed in a manner that combined preserves the spectral information of the nonfiltered image. For each filtered version, the minimization problem is solved and a composition stage is responsible for searching the high-pass information for each pixel in all filtered version. For each corresponding value of the components of Xf_n (reconstruction of the filtered version of the image), we divide the frequency corresponding by the filter H_n. The DC level of the image is lost in the filtering process, but it is reclaimed from the original measurements b. Although, this procedure leads to more reconstructions, they tend to be less computationally demanding and also allow parallelization for each filtered version reconstruction, which decreases substantially the total time of reconstruction.

Chapter 3

Initial Experiments

In this research, we evaluate the use of directional filters for reconstructing magnetic resonance images using compressive sensing with prefiltering. We argue than directional filters can potentially improve reconstruction when compared to separable filters, such as those used in the first prefiltering works. Furthermore, we explore different scenarios regarding the directional filters design, the total number of filters, the passband etc. In this chapter and in the following one, we describe these scenarios and the experiments we conducted in order to evaluate the final image quality in each case, in Figure 4.30 we present a summary of all the directional filters explored in this work.

We start by describing the adopted proceedings for the initial tests, which are divided into two approaches to build directional filters with smooth transitions. The algorithm used to minimize the l_p is IRLS, already described in Section 2.3.1.

3.1 Directional Filters with Smooth Transitions

The approach proposed by Miosso *et al.* in [37] makes use of filter banks in three different schemes in a way that combining Haar filters preserves the spectral information of the image; the DC components as well as other low-pass components are restored from the original measurements. Their experiments showed improvements in terms of SER and computation time over techniques as Total-variation (TV). However, they did not explore other filters or different trajectories. In this work, we propose the use of directional filters since they have showed to be able to extract edges and details in a predefined direction [50]. We are also exploring different smooth distributions for each direction of the filters and exploring different windows to truncate the filters. Initially, we are proposing two scenarios described below.

3.1.1 Scenario I: Projecting Directional Filters from a Smooth Frequency Distribution Along all Frequency Spectrum

We begin designing directional filters considering a smooth variation in the frequency domain, where the maximum frequency is placed at a given angle, varying across all frequencies until it reaches zero. The design of this filters follow three steps, where we first create a smooth distribution for the frequency domain (H_d), this version is almost what we want to use, except for the fact that it is a band-pass filter and we want only the high frequencies. Hence, we use a high-pass mask to preserve the high frequencies we want to keep. For that part is particularly important to preserve the smoothness of the filter, because we want to be as sparse as possible in the image domain and abrupt changes in the frequency domain leads to vestigial indexes in the image domain and that is exactly what we want to avoid. We calculate the filter version h_d in the image domain by calculating the Inverse Discrete Time Fourier Transform (IDTFT) of H_d. Finally, we create a bi-dimensional window to truncate h_d and then, calculate H for the image size we want.

I - *Smooth distribution*: For each set o n filters we calculate a smooth distribution H_{1d} according to the Hann Function 3.1, in each direction given by an determined angle between 0 to π.

$$W_h[n] = 0.5 + 0.5cos(2x - \pi). \tag{3.1}$$

The Hann function was chosen because we wanted to guarantee that the distribution reaches zero at the limits as show in Figure 3.1. Also, we limited the angles because the other half (H_{2d}) of the spectrum is a mirrored version of H_{1d}, or H_{1d} calculated with a 90° degrees forward shift. In that way, our smooth distribution is given by

$$H_d = H_{1d} + H_{2d}. \tag{3.2}$$

This is done as an attempt to create a symmetric filter, so we end up having a real image at the final of the reconstructions. Equally important, we apply the high-pass mask to guarantee a high-pass filter at the final of the design, the process can be visualized in Figures 3.2a, 3.2b and the three-dimensional versions in Figures 3.3a, 3.3b.

II - *Calculating h_d*: In order to calculate the filter h_d in the image domain it is used the smooth distribution H_d. Let $D\{h_d\}$ be the Discrete Time Fourier Transform (DTFT) of H_d, them $D^{-1}\{H_d\}$ is the IDTFT of h_d as described by the Equation 3.3 below.

$$h_d[n_1, n_2] = \iint_{2\pi} H_d[n_1, n_2] e^{j2\pi(n_1 f_1 + n_2 f_2)} df_1 df_2. \tag{3.3}$$

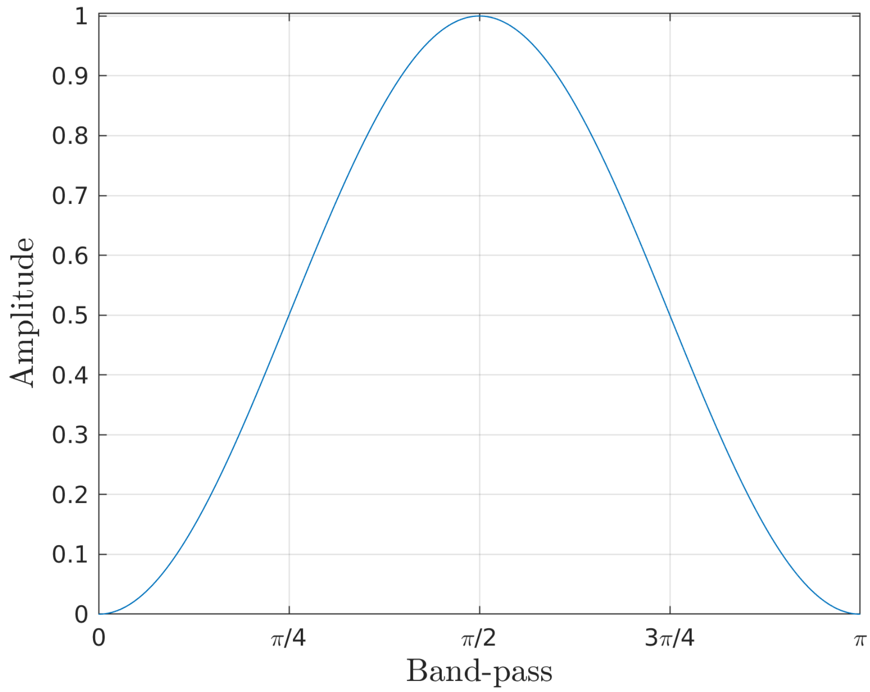

Figure 3.1. Hann function with independent variable x scaled over the frequency domain $[0, \pi]$. The function is used to determine the smooth distribution H_d along the chosen band-pass of the filter.

III - *Windowing*: Finally, the next stage relies on windowing the filters with a bi-dimensional window $W_{(N_o+1)\times(N_o+1)}$, where N_o is the order of the filter h_p. The Figures 3.4a, 3.4b, 3.4c and 3.4d are a visual illustration of the windows type used to truncate the filters h_p. After this step, each filter is transformed to frequency domain in order to filter the measurements b and to obtain the filtered versions b_f, where for each of them is reconstructed a filtered version of the MR image.

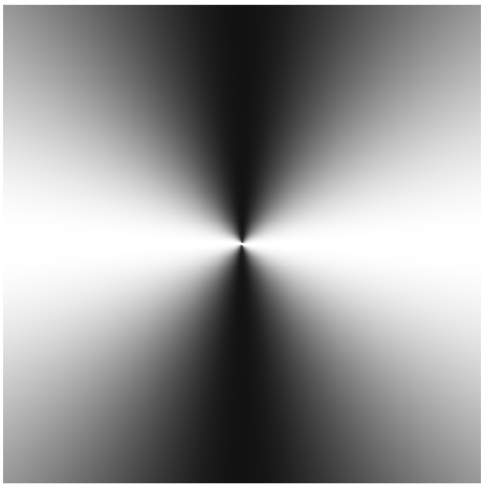

(a) Band-pass version of H_d.

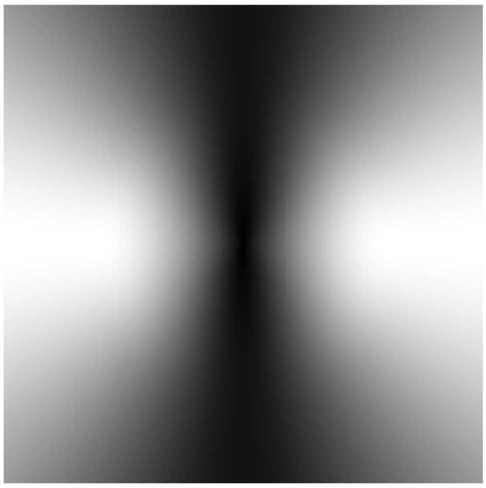

(b) H_d after the high-pass mask.

Figure 3.2. Visual difference comparison before and after applying a high-pass mask to eliminate low frequencies.

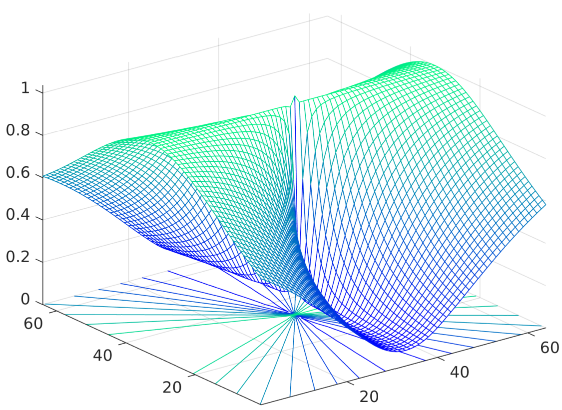

(a) Band-pass version of H_d.

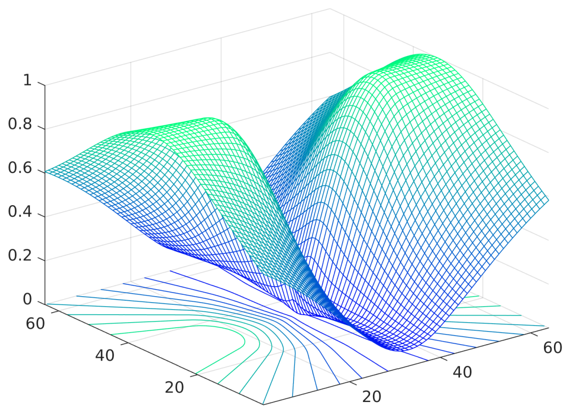

(b) H_d after the high-pass mask.

Figure 3.3. 3D representation of the filters in Figures 3.2a and 3.2b, respectively.

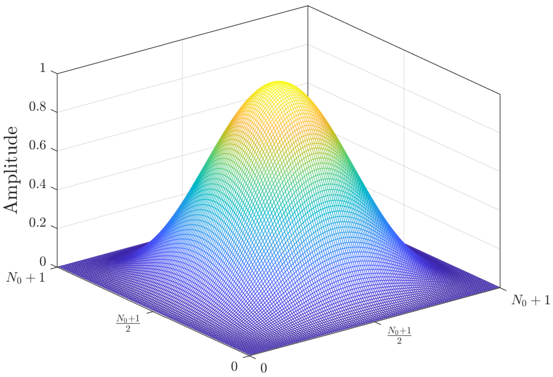

(a) Bi-dimensional Hann window.

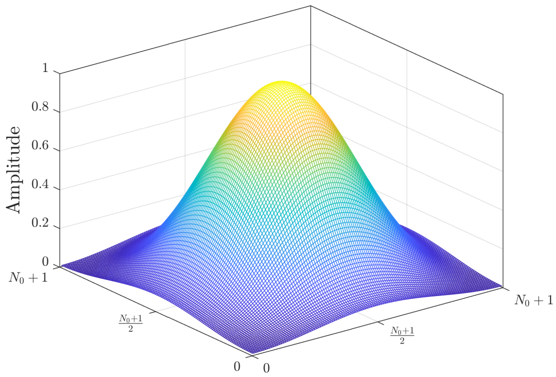

(b) Bi-dimensional Hamming window.

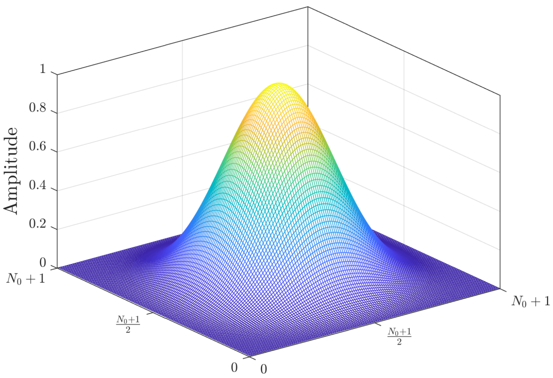

(c) Bi-dimensional Blackman window.

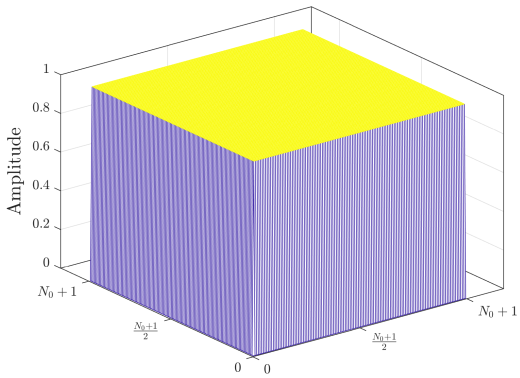

(d) Bi-dimensional rectangular window.

Figure 3.4. Bi-dimensional windows used to truncate h_p.

3.1.2 Scenario II: Implementing Directional Filters from Smooth Windows Distributions Along all Frequency Spectrum

This second set of filters can be seen as a special case of the scenario I previously presented in Section 3.1.1. Where the filter used to sparsify the measurements b are the smooth distributions H_d after applying the high-pass mask, differentiating only the functions for the distribution as described by the Equations 3.1, 3.4 and 3.5. The Figures 3.5a, 3.5b, 3.5c, show the resulting image of each filter with their respective distribution functions. To implement filters directly in the frequency domain does not guarantee control over the behavior of the intermediate frequencies, but this characteristic is not necessarily a problem if the filters are still capable to sparsify the filtered versions of the final image.

$$Hamming: \quad W_h[n] = 0.54 + 0.5cos(2x - \pi), \tag{3.4}$$

$$Blackman: \quad W_h[n] = 0.42 + 0.5cos(2x - \pi) + 0.08cos(4x - \pi), \tag{3.5}$$

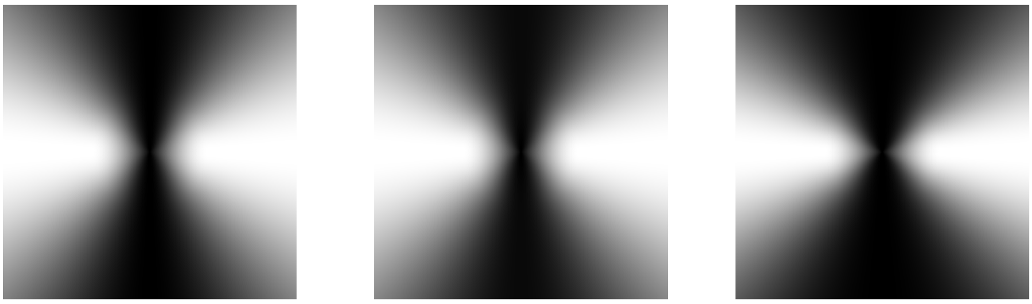

(a) **(b)** **(c)**

Figure 3.5. H_d version of the filters for **(a)** Hann function, **(b)**Hamming function and **(c)**Blackman function.

3.1.3 Simulated k-Space Measurements

We started from an image X and from that we calculated the measurements b by computing a Fourier Transform of X in a Cartesian grid and selecting the components closest to a trajectory τ in the k-space, this procedure is similar to the one in [11]. The Figure 3.6 represents the trajectory used to compose the experiments that will be described in the next section, and this trajectory represents $\approx 23.68\%$ of the possible measurements for the chosen size of the image. After that, we computed each filtered version b_f from the original measures b and composed the images following the process explained in Section 2.3.2.

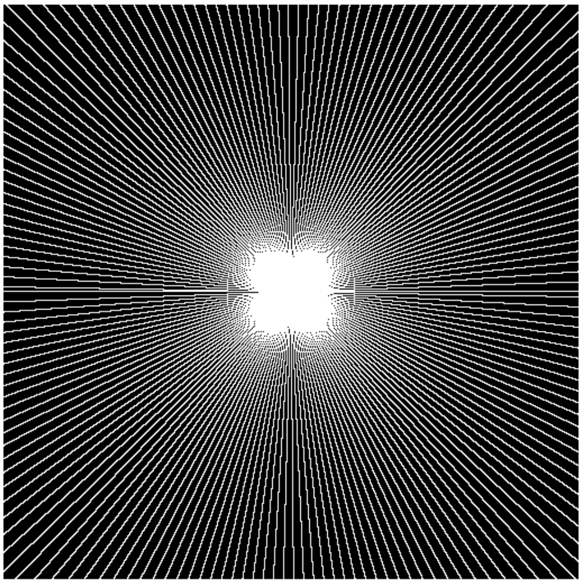

Figure 3.6. Radial trajectory with 90 lines representing $\approx 23.68\%$ of the possible measurements for an image of size 512×512.

3.2 Experimental Structure

For each scenario of filters, were computed experiments for 12 sets of filters $n = [2, 3, 5, 6, 7, 8, 9, 10, 20, 30, 35, 40]$, where $n(k)$ represents the number of filters for each set. They are equally distributed for all the frequency spectrum, according to a given angle. For example, for the set of filters with $n(2) = 3$, the maximum frequencies will be around the angles $(0, \frac{\pi}{3}, \frac{2\pi}{3})$ and their respective mirrored angles, since H_d were implemented in a way to guarantee symmetry, this can be seen in Figure 3.7a, 3.7b and 3.7c.

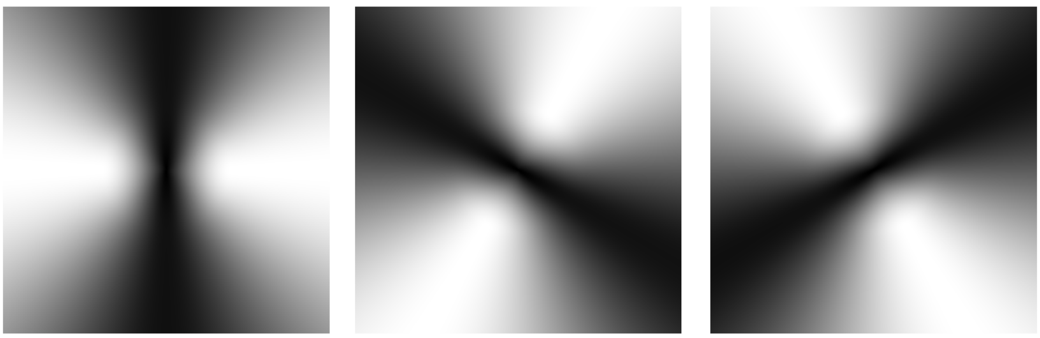

(a) **(b)** **(c)**

Figure 3.7. Set of H_d built using the same ground rules in scenario I. Windowed by Blackman window with 3 filters, where the maximum frequencies are around the angles $-\pi$ *and* π for **(a)**, $\frac{-\pi}{3}$ *and* $\frac{\pi}{3}$ for **(b)**and $\frac{-2\pi}{3}$ *and* $\frac{2\pi}{3}$ for (c).

The same criteria were used to build the other set of filters, in a way that, the bigger the n, the smaller the angle distance from the next filter in the set. We used two reference images to extract the measurements b, they are both displayed in Figures 3.8a and 3.8b, to simplify, we will refer to them as Shepp-Logan and Brain image. For the scenario I, we tested four windows type and reconstructed 48 MR images for each reference image. For the scenario II, we tested three distribution functions and reconstructed 36 MR images for each reference image, totalizing 168 reconstructions. For each image we evaluated the SER and the Structural Similarity Index Measure (SSIM). The SSIM is a measure that evaluates structural information and the dependence of samples of the image with its neighboring samples [51]. The structural index is assembled as a weighted combination of luminance (l), contrast (c), and structure (s) comparison, as

$$SSIM(x_1, x_2) = [l(x_1, x_2)]^{\alpha}[c(x_1, x_2)]^{\beta}[s(x_1, x_2)]^{\gamma}, \tag{3.6}$$

where x_1 and x_2, are the signals we are trying to compare. The equation (3.7) is built in a way to make sure the index satisfies similarity ($S(x_1, x_2) = S(x_2, x_1)$), where the order of the signals does not affect the comparison, boundedness ($S(x_1, x_2) \leqslant 1$), which states a upper bound as an indicator of how close the signals are and unique maximum ($S(x_1, x_2) = 1 \iff x_1 = x_2$), what means that the index is equal to 1, if and only if the signals are equal [52]. That being said, the index is stated as

$$SSIM(x_1, x_2) = \frac{(2\mu_{x_1}\mu_{x_2} + c_1)(2\sigma_{x_1x_2} + c_2)}{(\mu_{x_1}^2 + \mu_{x_2}^2 + c_1)(\sigma_{x_1}^2 + \sigma_{x_2}^2 + c_2)}. \tag{3.7}$$

Given the two signals x_1 e x_2 of same size $N \times N$, μ_{x_1} and μ_{x_2} are the sample mean, $\sigma_{x_1}^2$ and $\sigma_{x_2}^2$ are the sample variance and $\sigma_{x_1x_2}$ is the sample covariance of x_1 and x_2. The terms $c_1 = (k_1L)^2$, $c_2 = (k_2L)^2$ are variables to stabilize the division by the denominator, L is the dynamic range of the pixel value and the constants are $k_1 = 0.01$ and $k_2 = 0.03$, by default. Besides the image quality measurements, we also calculated the mean, maximum, and standard deviation reconstruction time for each set of filters.

3.3 Preliminary Evaluation of Filter Design Strategies

In this section, we present and discuss the results of both scenarios I and II. All images reconstructed in this work where a minimization of the l_1-norm using the method described in the Section 2.3.1.

Experiment Settings :

- ***Reconstructed images***: Two reconstructed images 3.8a and 3.8b, both of size 512×512.

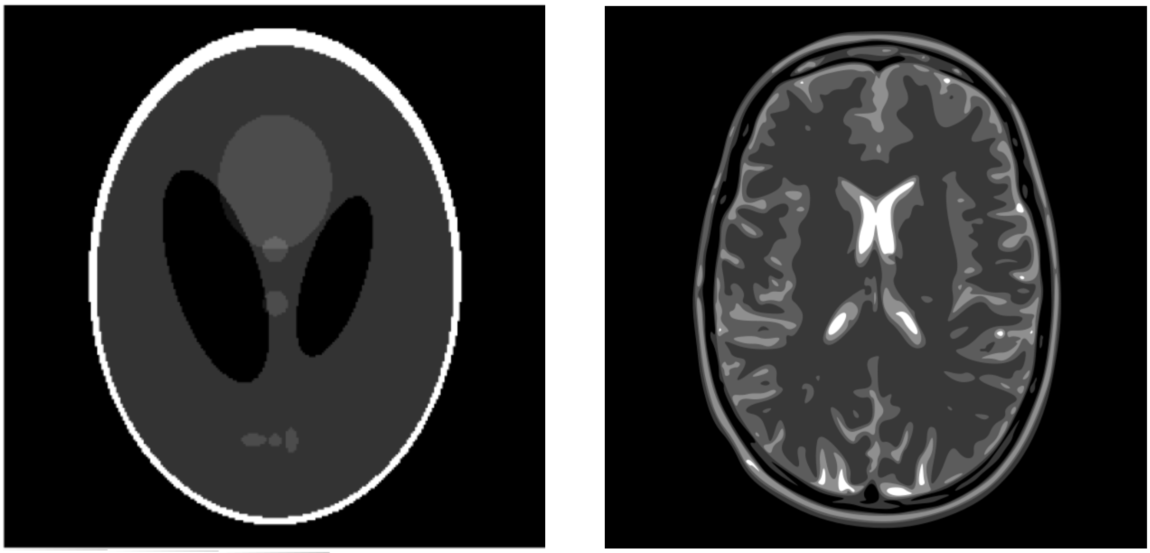

(a) Shepp-Logan phantom. **(b)** Transverse section phantom of the brain.

Figure 3.8. Images used to test the filters in the scenarios I and II.

- ***Trajectory***: Radial;
- ***Measurements***: 90 radial lines;
- ***lp minimization***: p = 1;
- ***Filters***: Directional filters from Scenario I and II;
- ***Exclusion Criteria***: Reconstructions with SER under zero.
- ***Total of Reconstructions***: 96 reconstructions from Scenario I and 72 reconstructions from Scenario II, 168 total.

3.3.1 Comparison between Scenario I and II

The Figures 3.9 and 3.10 lay out in graphs the quality parameters results for the reconstructions of the Shepp-Logan phantom in Figure 3.8a, where SER and SSIM are in function of the number of filters utilized to filtrate the image spectrum. In the scenario II the results for the set of 2 filters with smooth distribution following the equations of the Blackman and Hann windows was omitted since they were not able to properly reconstruct the images. In this work we are considering that the signal was reconstructed when SER > 0. All graphs presented in this section have a guideline legend where we separate the groups of filters by scenarios and window used to truncate the filters or smooth distribution, in both cases refereed by the function name. As an example of how to read the graphs; in Figure 3.9, all the graphs with an asterisk ($*$) are designed as described in Section 3.1.1 (Scenario I). So, the first graph in red with asterisks shows the

SER results for the filters design as described in Scenario I and also truncated by a rectangular window as the one shown in Figure (3.4c). The analogous analysis works for the other set of graphs. The purple graph with markers in circles (o) displays the SER results for the filters implemented as described in Section 3.1.2 (Scenario II) from a frequency distribution described by the Blackman Function (3.5). In both quality measurements, SER and SSIM, the higher the value the best performance has the filter. Where for the SSIM we evaluate the luminance, contrast and structure of the reconstructed image and the closeness to 1 means that the image has no distortion, degradation or changes in the structural information when compared to the original image in terms of absolute error. On the other hand, SER evaluates the ration of the power of the original image and the error between the original and reconstructed image. To elucidate, usually, SER values are reported with a significance of 0.1 dB and SSIM with significance of 0.001. In this work, we extrapolate the significance of both parameters by one decimal, to present even slight differences between our filters. An interesting example happens with the set of filters qualified as best SER and SSIM results for the Shepp-Logan phantom. In Figures 3.11a and 3.12a we have the reconstructions for the best SER and SSIM, respectively, however, evaluating the parameters we can tell that both reconstructions have a slight difference in terms of the quality parameters, but only noticeable when extrapolating the conventional significance used to report the measures. Since the filters can be considered similar in terms of quality of the final reconstructions measured here, we can take in account the number of filters in the set. That being said, the set of 5 filters is a preferable choice because even considering that the reconstructions are being parallel computed, the composition stage will take less time to search for the coefficients of Xr between 5 X_{fn} (reconstructions of the filtered versions of the phantom in frequency domain), than 35.

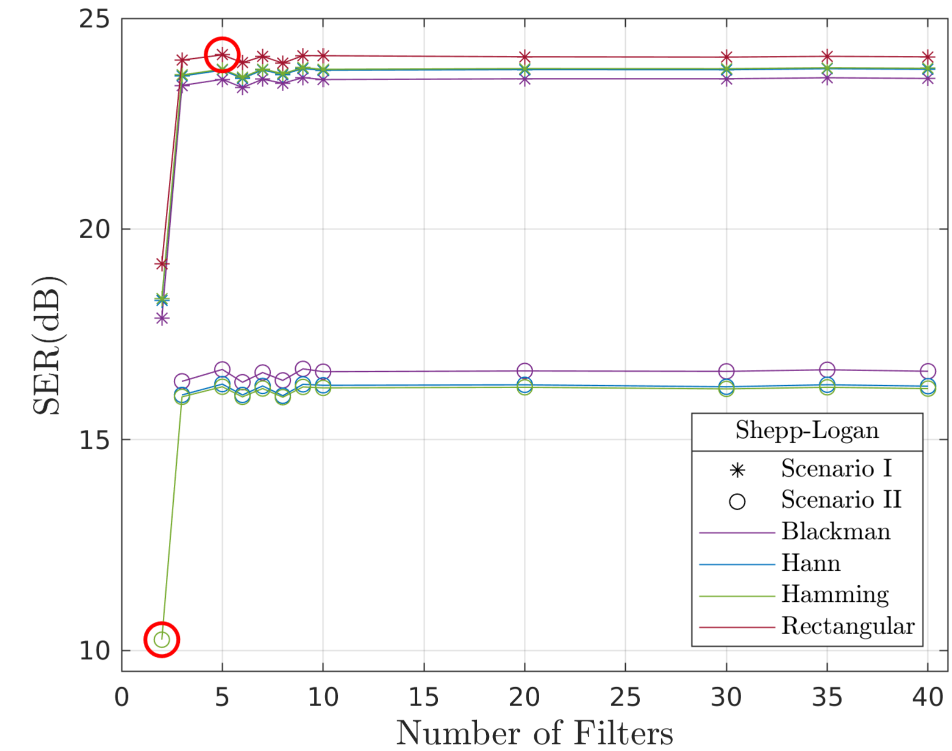

Figure 3.9. SER results for the reconstruction of the Shepp-Logan image in the scenarios I and II. The red circles highlights the highest and lowest SER for the image.

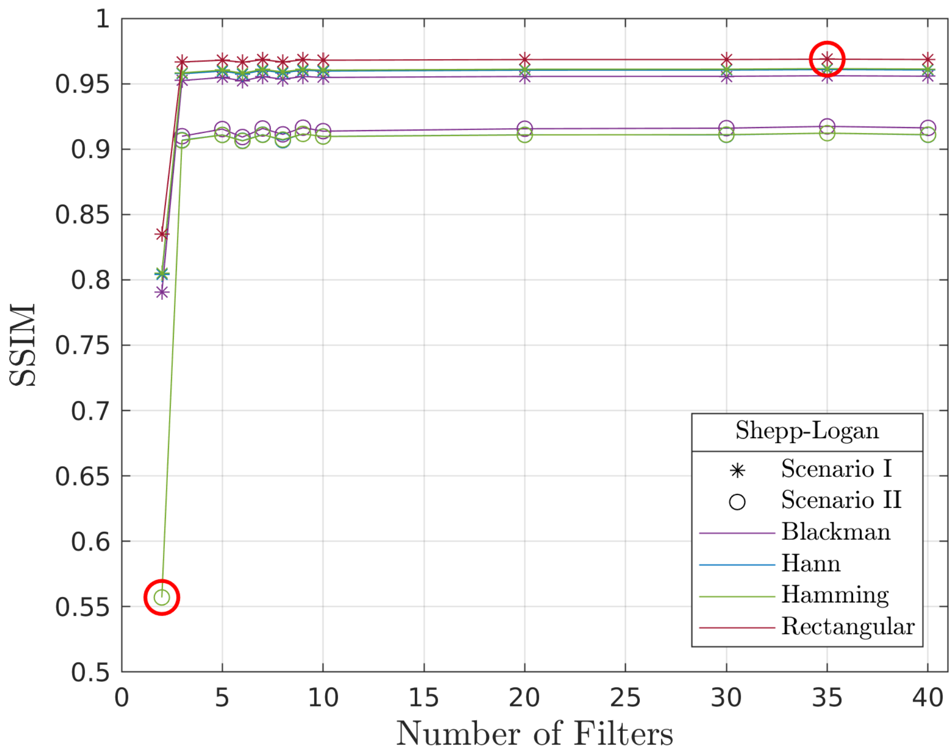

Figure 3.10. SSIM results for the reconstruction of the Shepp-Logan image in the scenarios I and II. The red circles highlight the highest and lowest SSIM for the image.

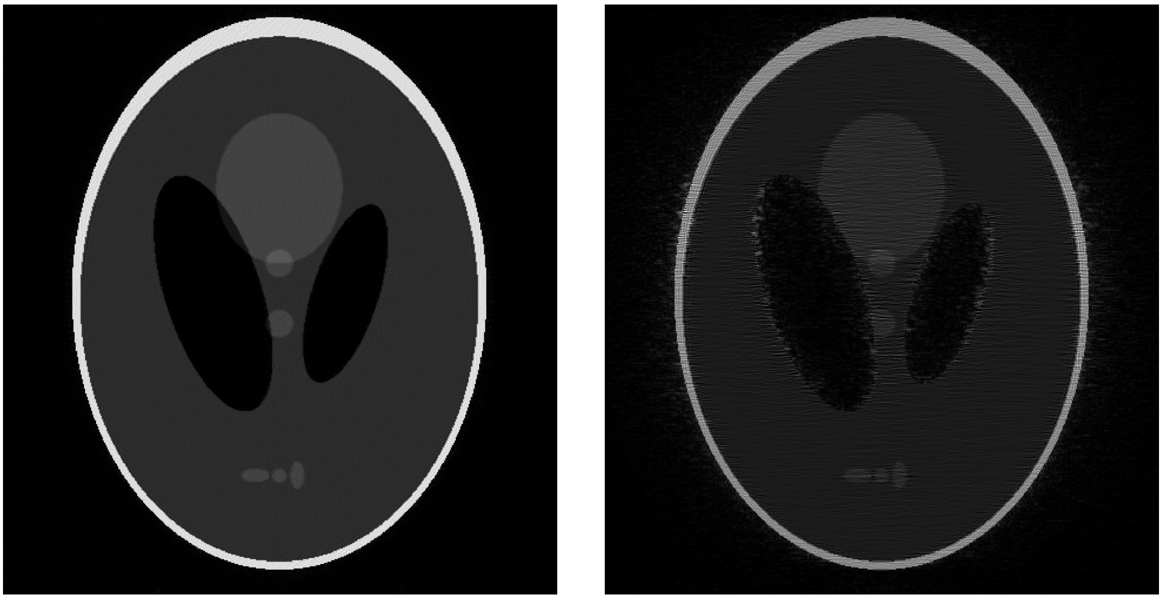

(a) SER = 24.13 dB, SSIM = 0.9679. **(b)** SER = 10.26 dB, SSIM = 0.5571.

Figure 3.11. Best and worst SER results for the reconstruction of the Shepp-Logan comparing both scenarios. **(a)** Reconstruction with filters from scenario I: Set of 5 filters and rectangular windowing. **(b)** Reconstruction with filters from scenario II: Set with 2 filters and smooth distribution following the equation of the Hamming windowing.

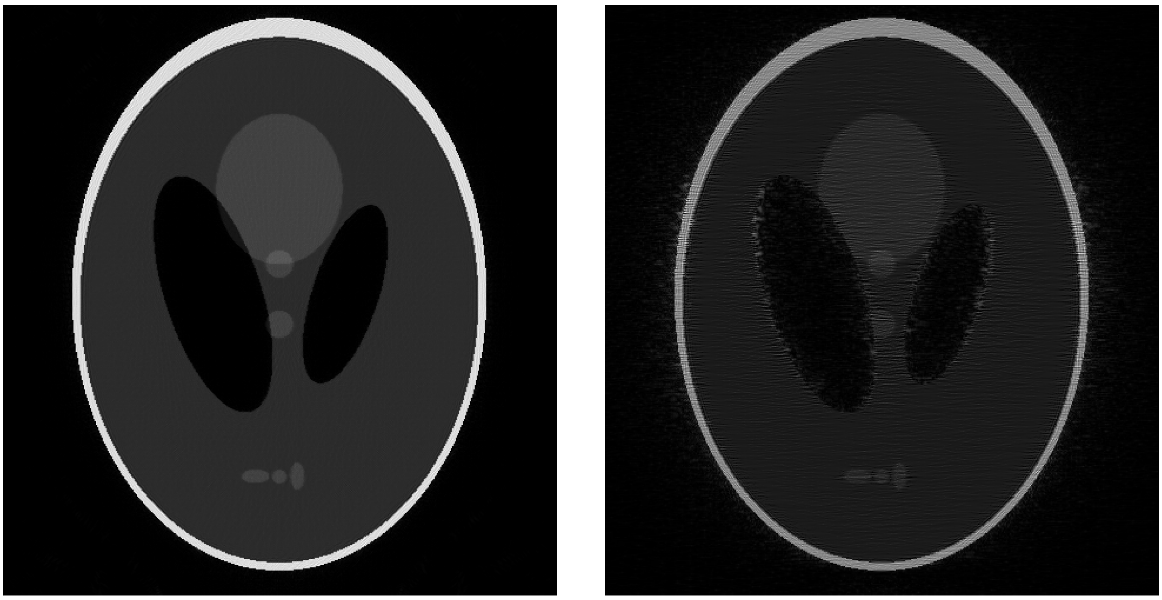

(a) SER = 24.08 dB, SSIM = 0.9688. **(b)** SER = 10.26 dB, SSIM = 0.5571.

Figure 3.12. Best and worst SSIM results for the reconstruction of the Shepp-Logan. **(a)** Reconstruction with filters from scenario I: Set of 35 filters and rectangular windowing **(b)** Reconstruction with filters from scenario II: Set with 2 filters and smooth distribution following the equation of the Hamming windowing.

Next, the Figures 3.13 and 3.14 are the reconstruction results for a more complex phantom of the brain, Figure 3.8b. The following two Figures 3.15a and 3.15b are the final reconstructed images comparison between the best and worst SER and SSIM results for the Brain phantom. In this case, both quality measures seemed to agreed revealing the same set of filters for the best and worst reconstructions. Also, for both phantoms, the set of 2 filters with smooth distribution following the equation of Hamming was the worst reconstruction comparing the both Scenarios I and II. Although, adding one filter to the same design of filters and placing the higher frequencies of each filters in angles equally distant from each other as the filters in Figures 3.7a, 3.7b and 3.7c resulted in an increase of 5.8 dB in SER and 0.394 in SSIM for the Shepp-Logan and 9.9 dB in SER and 0.117 in SSIM for the Brain phantom. In the Figures 3.16 and 3.17, we present again the SER results but this time as an attempt to compare how each design of filter behave for one of the phantoms. An interesting observation here is that even if the Brain phantom is, in theory, more complex than the Shepp-Logan image, the filters tested until here showed higher SER results and this will be taken in account to explore other designs for the directional filters, as well as different images to test the filters sparsifying potential.

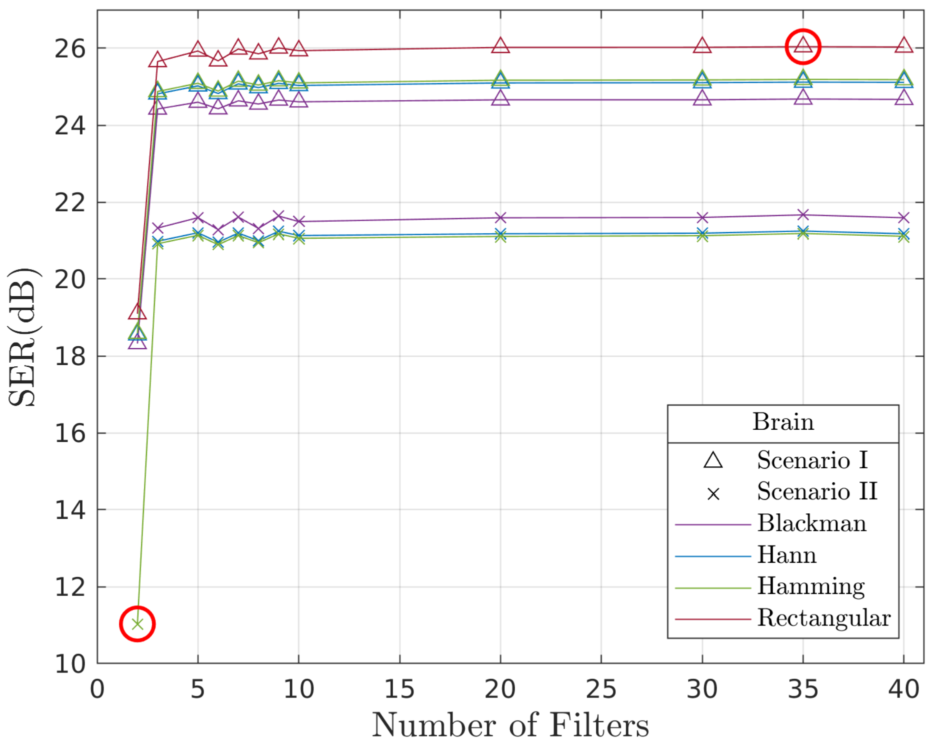

Figure 3.13. SER results for the reconstruction of the Brain image in the scenarios I and II. The red circles highlight the highest and lowest SER for the image.

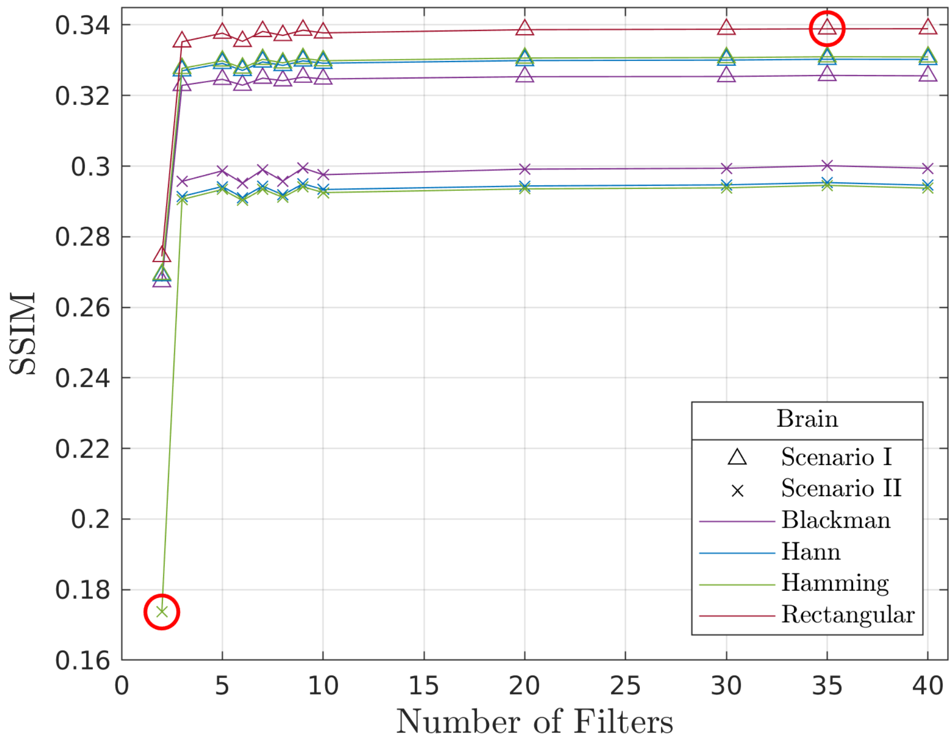

Figure 3.14. SSIM results for the reconstruction of the Brain image in the scenarios I and II. The red circles highlight the highest and lowest SER for the image.

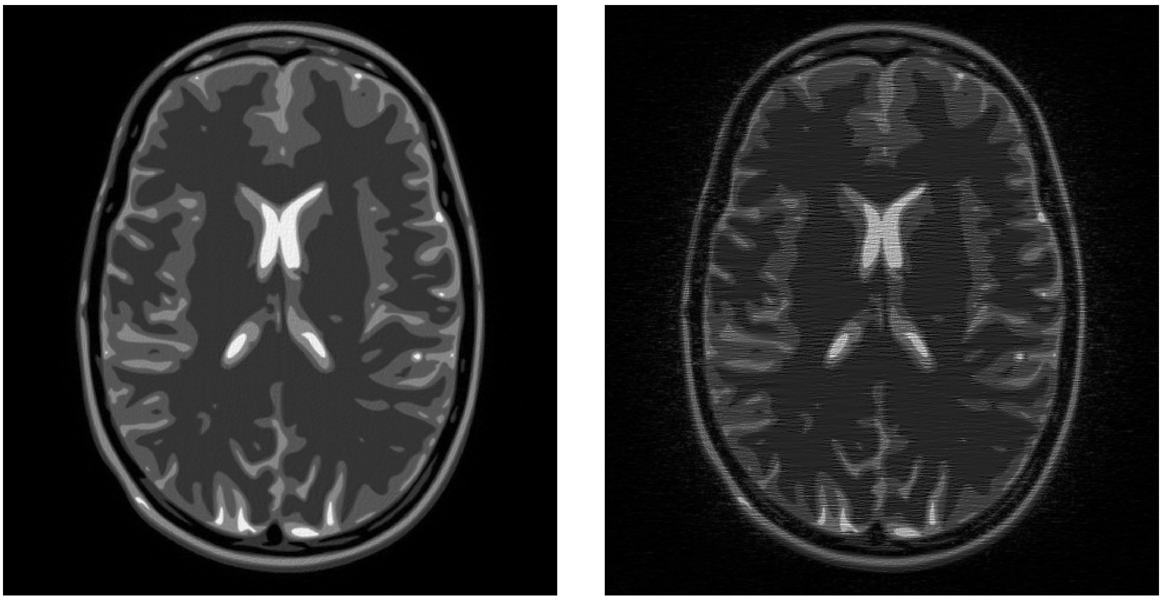

(a) SER = 26.04 dB, SSIM = 0.3389. **(b)** SER = 11.03 dB, SSIM = 0.1737.

Figure 3.15. Best and worst SER and SSIM results for the reconstruction of the Brain phantom. **(a)** Reconstruction with filters from scenario I: Set of 35 filters and rectangular windowing **(b)** Reconstruction with filters from scenario II: Set with 2 filters and smooth distribution following the equation of the Hamming windowing.

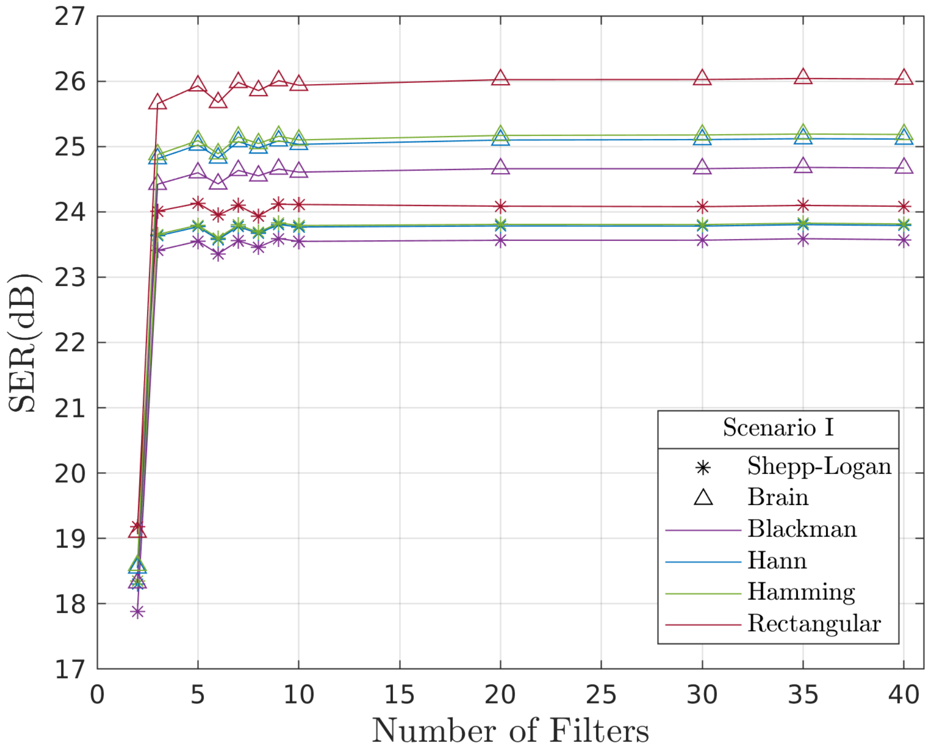

Figure 3.16. SER results for the Shepp-Logan and Brain images in scenario I.

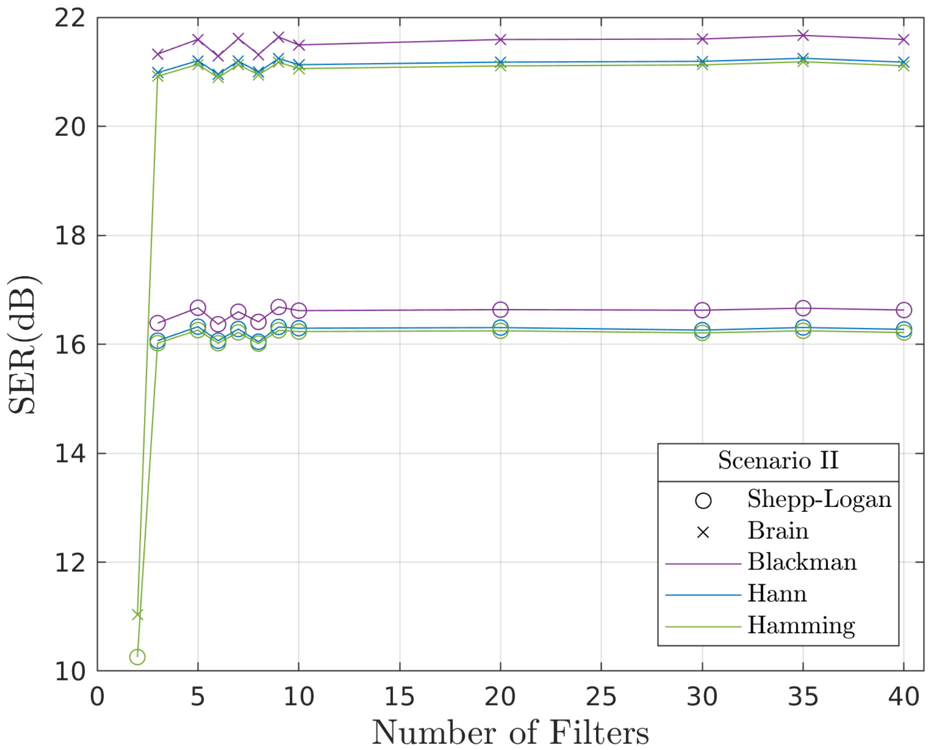

Figure 3.17. SER results for the Shepp-Logan and Brain images in scenario II.

Chapter 4

Further Experiments with Directional Filters

This chapter is composed of three sections, where we first describe different approaches to design directional filters and next, we present and discuss reconstructions with these filters using phantoms. Each design approach is described in a section and their respective graph results for the quality measures SER and SSIM of each image. In the last section, we present a group of tests with a real image of the brain in different trajectories.

4.1 Exploring Smooth Filters in a Frequency Range

4.1.1 Scenario III: Projecting Filters From an Ideal Frequency Response Distribution in a Range of the Frequency Spectrum

The present set of filters is built following the mathematical process of filters design using the windowing method. The steps are described as a comparison to what was designed in the initial experiments as an attempt to exemplify the theoretical differences between each set of filters. That being said, the filters were design similarly to the process of the filters in Section 3.1.1 (Scenario I) following the steps of the windowing method. The difference is in the frequency distribution adopted here. Therefore, in Equation 3.3, $H_d = 1$, and $h[n_1, n_2]$ is calculated for the limits of the angles (θ), equally distributed between the number of filters, and the radius r. We also apply a high-pass mask to eliminate the low frequencies from our filters. The windows applied here are the same as illustrated in Figures 3.4a, 3.4b, 3.4c and 3.4d and the visual result of the filters are presented in Figures 4.1a, 4.1b, 4.1c, 4.1d. To standardize, we kept the same number of filters as $n = [2, 3, 5, 6, 7, 8, 9, 10, 20, 30, 35, 40]$ and the same phantoms Shepp-Logan 3.8a and Brain 3.8b while comparing the filters scenarios.

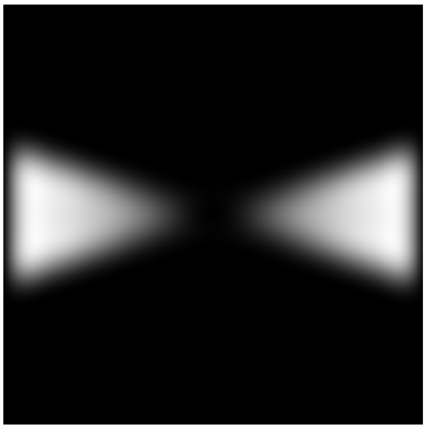

(a) Hann windowing.

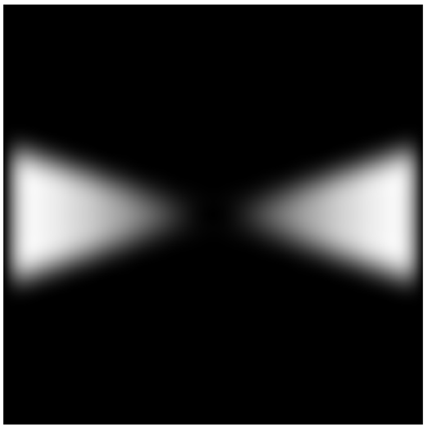

(b) Hamming windowing.

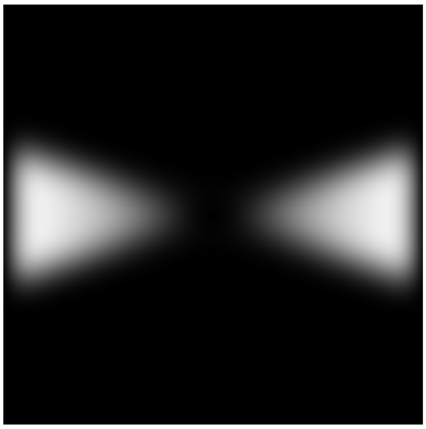

(c) Blackman windowing.

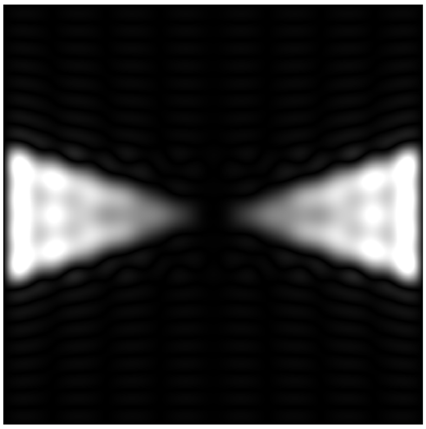

(d) Rectangular windowing.

Figure 4.1. Visual output of the filters in Scenario III.

4.1.2 Scenario IV: Implementing Directional Filters From a Smooth Frequency Distribution in a Range of the Frequency Spectrum

The filters investigated in Section 3.1.2 (Scenario II) where implemented following a smooth distribution of half the frequency spectrum in a way that the distribution displayed a symmetry for each half of the spectrum. Analogous to this structure, the filters here are design following the same arrangement for the smooth distributions distinguishing only from the range of the smooth distribution adopted. Instead of expanding the smooth distribution along all the spectrum, we limit the distribution in a range equally divided between the number of filters in the set. To summarize, the filters in this scenario are implemented in the frequency domain assuming a smooth distribution according to the equation of the windows of Hann, Hamming and Blackman, as previously described by the equations 3.1, 3.4 and 3.5, respectively. The Figures 4.2a, 4.2b and 4.2c below present the visual result of the filters in this configuration.

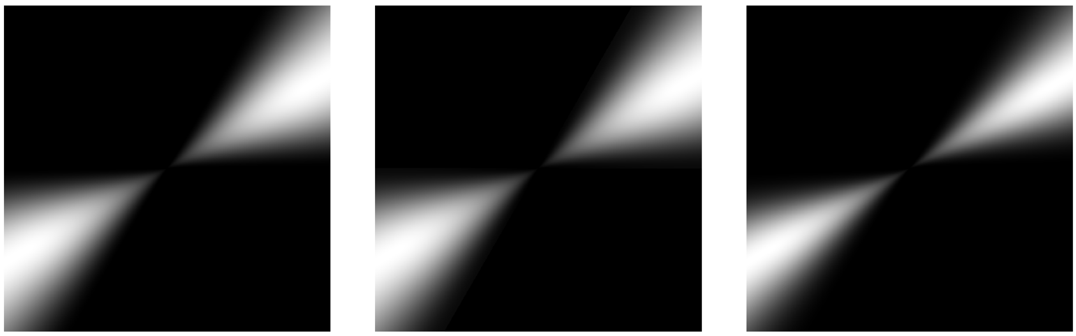

(a) Hann distribution. **(b)** Hamming distribution. **(c)** Blackman distribution.

Figure 4.2. Visual display of the filters following the smooth distribution of the equations of the Hann, Hamming and Blackman window.

4.1.3 Scenario V: Implementing Filters From an Ideal Frequency Response Distribution in a Range of the Frequency Spectrum

The following set of filters can be understood as a special case of the filters in the previous Section 4.1.2, where we implement the filters in an ideal frequency response range, also, equally divided between the number of the filters. In this case, we built a set of filters to contrast with the ones in Scenario IV to test and compare the effects of the smooth transition in a range of the filter gain. The process to implement the filters in this section is actually simple. For each set of n filters, we have to divide the frequency spectrum by the number of filters, in a way to implement symmetry between the angle directions, and in the range of the Discrete Fourier Transform (DFT) of each filter we place the gain as one and zero at the other frequencies. The Figure 4.3 shows the visual result of the filters with ideal frequency response distribution.

Figure 4.3. Visual display of the filters in Scenario V following an ideal frequency response distribution.

4.2 Experimental Results and Comparison

Experiment Settings :

- ***Reconstructed images***: Two reconstructed images 3.8a and 3.8b, both of size 512×512.
- ***Trajectory***: Radial;
- ***Measurements***: 90 radial lines;
- ***lp minimization***: p = 1;
- ***Filters***: Directional filters from Scenario III, IV and V;
- ***Exclusion Criteria***: Reconstructions with SER under zero.
- ***Total of Reconstructions***: 96 reconstructions from Scenario III, 72 reconstructions from Scenario IV and 24 reconstructions from scenario V, 192 total.

In the present section, we display the quality parameters results SER and SSIM of the reconstructions with directional filters designed in all the five scenarios explored in this research. To compare the results, we plotted again the graphs for the Scenario I and II alongside to the other scenarios graphs. The graphs are presented in the same way explained in Section 3.3.1, where the legend shows the separation of the filters set by scenarios with different markers and specify the type of the smooth distribution or truncation with a window by colors. Likewise, the results presented in the previous Chapter 3, we also pointed out the best and worst SER and SSIM results, see Figures 4.7a, 4.7b, 4.11a, and 4.11b. We display them not only to visually and mathematically contrast the highest quality index measures with the lowest outcomes, but to also compare or even highlight features that should be avoided in future design of directional filters when compared with the ones who had a better outcome. Since the best and worst outcomes, as shown in Figures 4.4, 4.5, 4.9, 4.10, for both phantoms are coming from the filters in scenario III, designed from an ideal frequency response distribution with windowing method, we want to start a comparison between those specific set of filters and analyze how their gain are distributed in the frequency spectrum. A central idea behind the design of directional filters to reconstruct MR measures with prefiltering is to favor the sparsity of each filtered version, Xf_n, because sparsity is not only a highly valuable feature, but also the piece of information that makes possible for CS to reconstruct signals with less measures when compared to other techniques. For that reason, we designed the filters thinking in smooth transition bands and a big γ (4.1) ratio between the main lobes and side lobes of the filters.

$$\gamma = \frac{|G(e^{jw})|}{|\delta|} \tag{4.1}$$

Overall, the quality indexes show that by truncating the filters with windows that have fixed ripples as Blackman, Hann and Hamming payoff in terms of diminishing the effects of Gibbs phenomenon and it has a positive effect on the quality of the final reconstructed images. This effect can be seen in the graphs of scenario III in Figure 4.27, where all the red graphs of the filters windowed with a rectangular windowing is below the SER rate of the other filters for the same reconstructed image. For the case of the best result for the Shepp-Logan phantom with Blackman windowing and 6 filters, the final image reconstruction is 4.3 dB in SER and 0.03 in SSIM above the filters with rectangular windowing and same set number, refer to Figure 4.6 to see the SSIM results. In addition to this analysis, the worst reconstruction case for both phantoms are from the scenario III with rectangular windowing in the set with 3 filters. This set of filters seem to be an outline, since reconstructing the same images with 2 or 5 filters in the set showed better results, with a SER gain of more than 20 dB, for both cases. Considering this outline aspect and the positive effects on diminishing the ripples in the stop band of the filters, it is possible that not only the size of the ripples but also how they are distributed in the frequency domain of the signal has an impact on how well these filtered versions are able to preserve the spectrum of the images in the composition stage. In Figures 4.8 and 4.12 we present some of the filtered xf_n reconstructions for the Haar filters and the best and worst result of the directional filters. Defining the sparsest xf_n versions visually is a challenging task, since the images seem alike. However, comparing the xf_n from Haar with the xf_n from the directional filters with worst results, the edges of the image seem to be scattered, although this not necessarily means that the final image will be of poor quality.

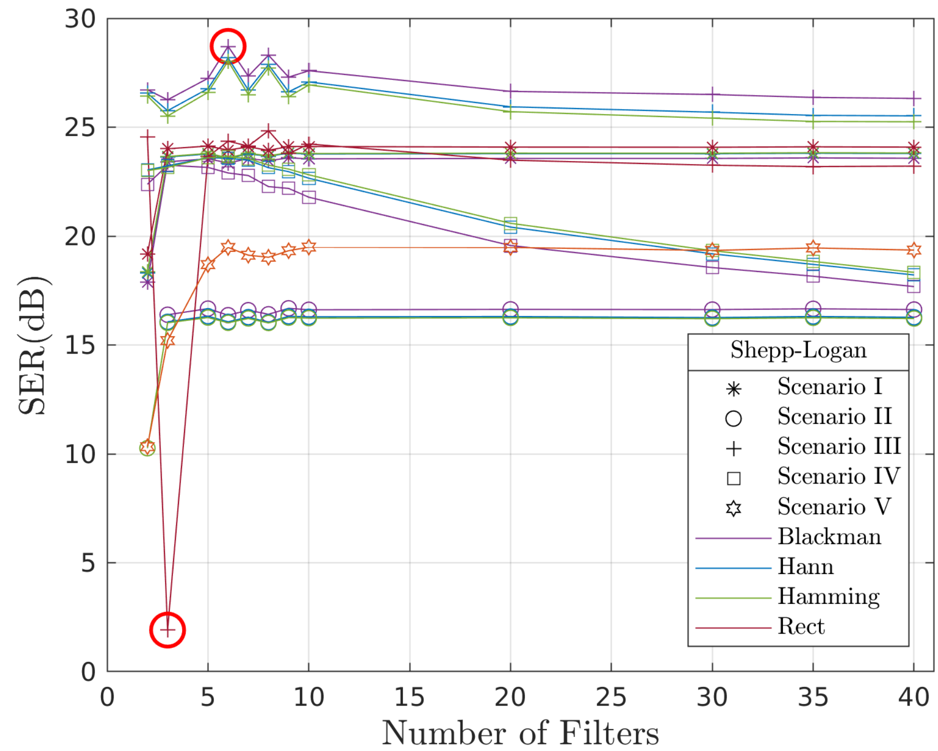

Figure 4.4. SER results for the reconstruction of the Shepp-Logan phantom. The red circles highlights the highest and lowest SER for the image.

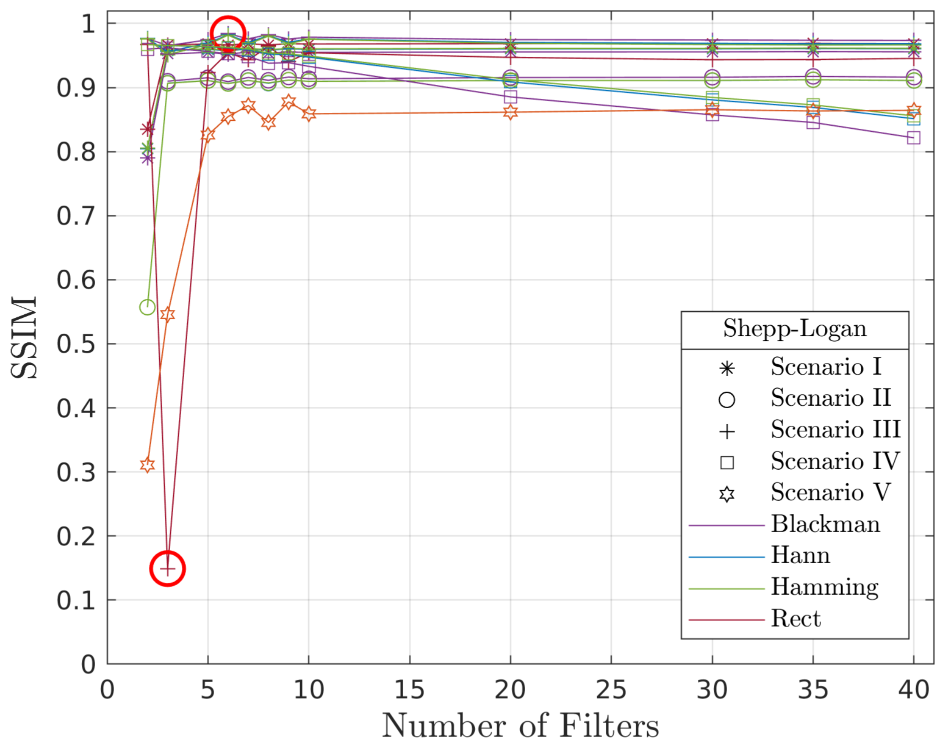

Figure 4.5. SSIM results for the reconstruction of the Shepp-Logan phantom. The red circles highlight the highest and lowest SSIM for the image.

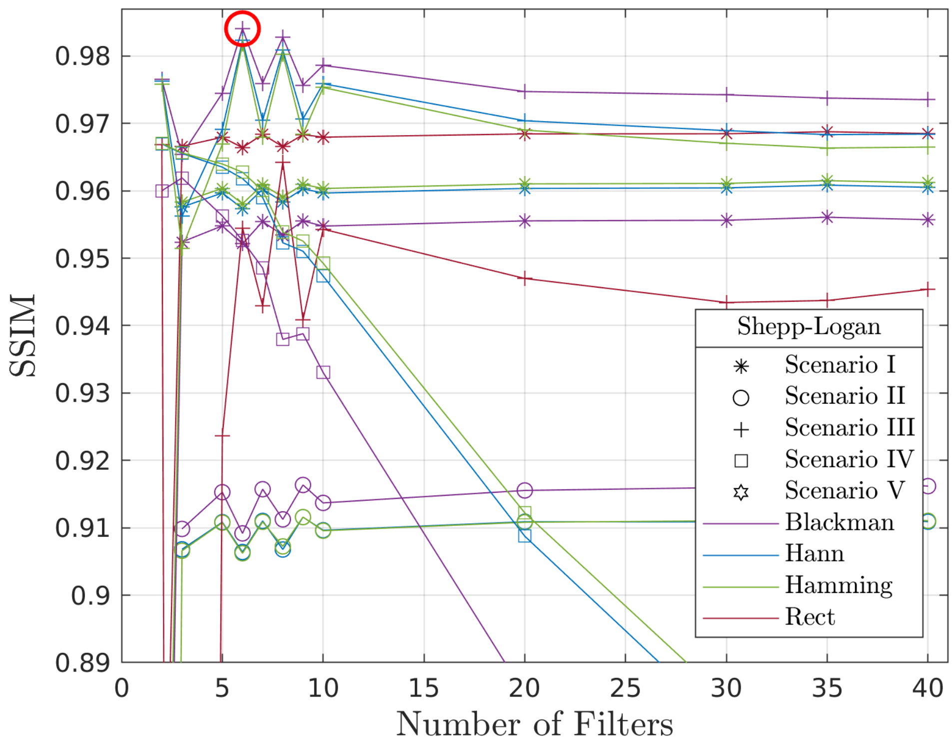

Figure 4.6. Zoomed in view of the upper graphs in SSIM results for the reconstruction of the Shepp-Logan phantom. The red circle highlight the highest and lowest SSIM for the image.

(a) SER = 28.71 dB, SSIM = 0.984.

(b) SER = 1.90 dB, SSIM = 0.149.

Figure 4.7. Best and worst SER and SSIM results for the reconstruction of the Shepp-Logan. **(a)** Reconstruction with filters from scenario III: Set of 6 filters and Blackman windowing. **(b)** Reconstruction with filters from scenario III: Set with 3 filters and rectangular windowing.

(a)

(b)

(c)

Figure 4.8. Reconstructed sparse xf_n components of the Shepp-Logan phantom. In **(a)** we have the three sparse components used to compose the final image, in **(b)** we have the three xf_n versions ($n = [10, 20, 30]$) for the Directional filter with best results, in **(c)** we have the three xf_n versions ($n = [10, 20, 30]$) for the Directional filter with worst results.

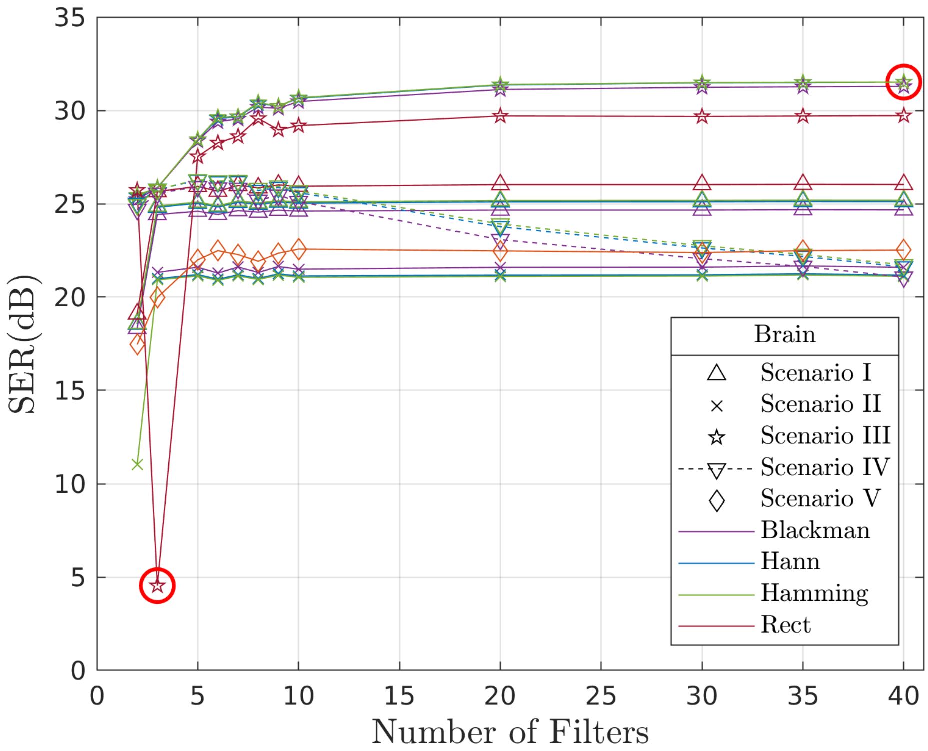

Figure 4.9. SER results for the reconstruction of the Brain phantom. The red circles highlight the highest and lowest SER for the image.

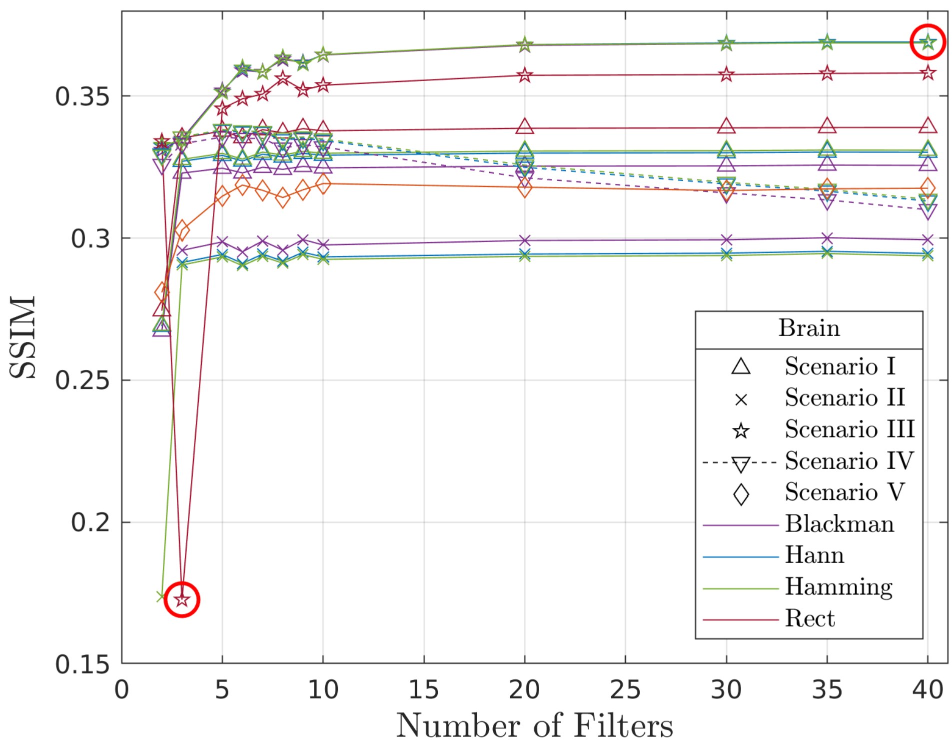

Figure 4.10. SSIM results for the reconstruction of the Brain phantom. The red circles highlight the highest and lowest SSIM for the image.

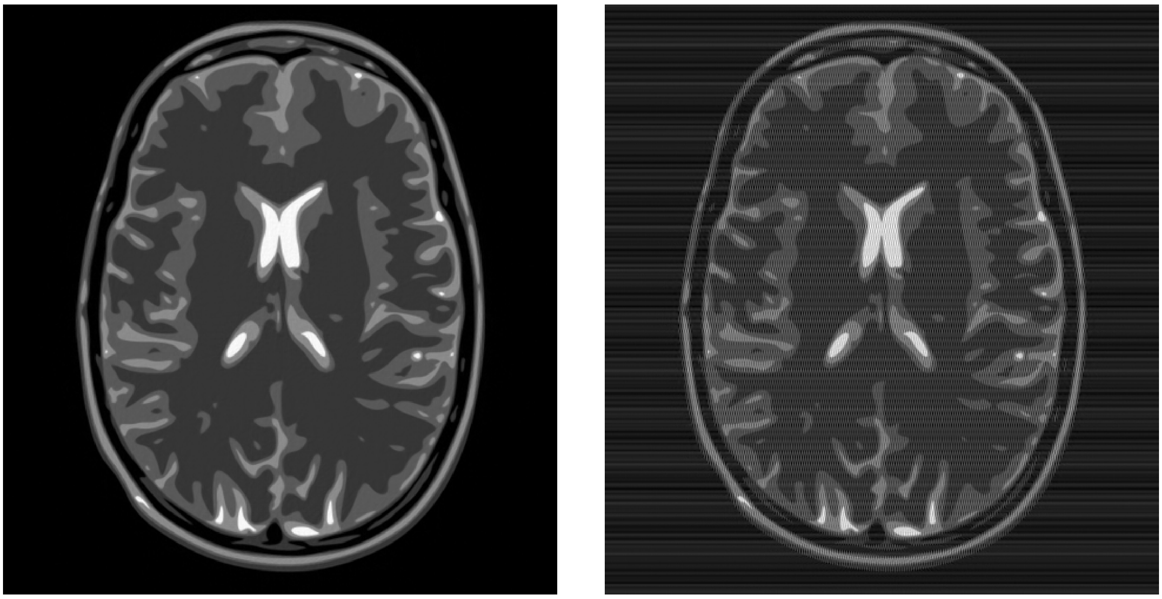

(a) SER = 31.52 dB, SSIM = 0.369.

(b) SER = 4.54 dB, SSIM = 0.1727.

Figure 4.11. Best and worst SER results for the reconstruction of the Brain phantom. **(a)** Reconstruction with filters from scenario III: Set of 40 filters and Hann windowing. **(b)** Reconstruction with filters from scenario III: Set with 3 filters and rectangular windowing.

(a)

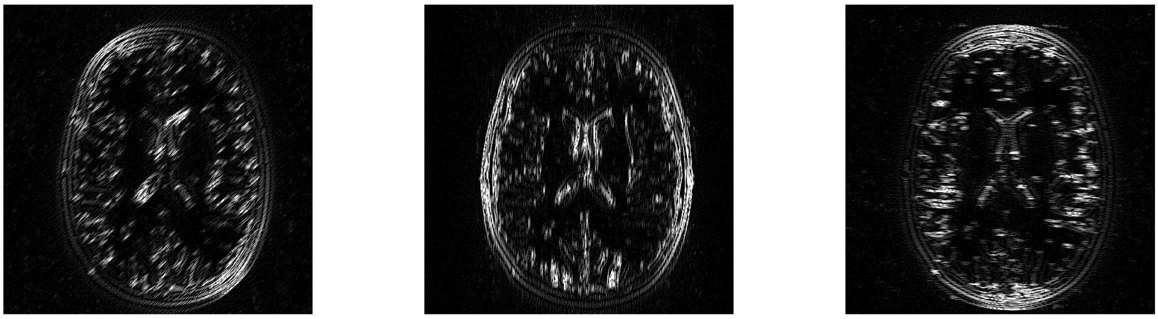

(b)

(c)

Figure 4.12. Reconstructed sparse xf_n components of the Brain phantom. In **(a)** we have the three sparse components used to compose the final image, in **(b)** we have the three xf_n versions ($n = [10, 20, 30]$) for the Directional filter with best results, in **(c)** we have the three xf_n versions ($n = [10, 20, 30]$) for the Directional filter with worst results.

4.3 Experiments with Real Image

Experiment Settings :

- ***Reconstructed images***: Head image originally of size 1024×1024 downsampled to a size of 512×512.

- ***Trajectories***: Radial and Spiral with exponential radius growth;

- ***Measurements***: 90 radial lines and 180 turns for spiral trajectory;

- ***lp minimization***: p = 1;

- ***Filters***: Directional filters from Scenarios, I, II, III, IV and V;

- ***Exclusion Criteria***: Reconstructions with SER under zero.

- ***Total of Reconstructions***: 96 reconstructions from Scenario I, 72 reconstructions from Scenario II, 96 reconstructions from Scenario III, 72 reconstructions from Scenario IV and 24 reconstructions from scenario V, 360 total.

From the reconstructions with phantoms we notice that the directional filters seemed to benefit from the structure of the Brain phantom and it was reflected in the SER higher than the ones for the Shepp-Logan phantom. For that reason, we reconstructed a real image that we will refer simply as Head image. We first acquired b measures in the same radial trajectory in the k-space as in Figure 3.6 and next with a spiral trajectory represented in Figure 4.18 with exponential radius growth and 180 turns. In these experiments the main goal was to compare the performance of the directional filters designed to the separable Haar filters, also by means of comparison, we reconstructed the image with a TV optimization routine, described as barrier iterations for equality constrained TV minimization in [45]. The Figures 4.13 and 4.14 show the SER and SSIM graphs for all the reconstructions with the directional filters in the different scenarios. We also plotted the Haar results with 3 filters as the scheme proposed by Miosso in [37] represented by a red star marker in both graphs. To help identify the filters set with higher SER and SSIM values than the Haar filters we plotted a dashed line that indicates that the filters above this reference line have presented higher values of the quality indexes for the reconstruction with the real image. Similarly to the previous experiments with phantoms the filters set from scenario III presented the best results in terms of quality measures but it seems that there is a minimum range from where the frequency spectrum should be divided in order to favor sparsity in the filtered measures b_f. For SER index, only the set after 8 filters started to present a gain in comparison with the Haar filters the gain went from 0.2 dB until 1.25 dB.

In terms of structural similarity, the gain started to be expressive after 10 filters in the set with a gain of 0.005 until 0.012 in SSIM. An interesting result from the filters in scenario III truncated with a rectangular window is that the distortion caused in the impulse response of the filter due to the rigging created at the edge of the transition band can be compensated if we redistribute the frequency spectrum in small ranges with more filters, this aspect can be seem starting from the set with 20 filters. In addition, the worst reconstruction result for the Head image is also from the same set of filters, which presented the worst results with the phantoms. This reinforces the idea that the distribution range of the frequency spectrum between the filters affect its capability to produce sparser versions of the measures. The reconstructed images of the head are displayed in Figures 4.15a, 4.15b, 4.15c and 4.15d, a detail of the reconstruction is presented in Figures 4.16b, 4.16c, and 4.16d to help the visual comparison, the first Figure 4.16a is the original image from where the measures were extracted. Also, in Figures 4.17a, 4.17b, and 4.17c, we present the some of the xf_n reconstructions for the Haar and directional filters. In Table 4.1 we summarize the results of the reconstructions from measurements acquired in a radial trajectory with Haar, directional filters and TV. From that, we see that the reconstructions of piecewise continuous images show better results with classical approaches as TV, compared to directional filters, however, the reconstruction using CS with prefiltering with Haar filters present better results in terms of image quality. On the other hand, reconstructions using CS with prefiltering using directional filters present higher results in terms of quality indexes.

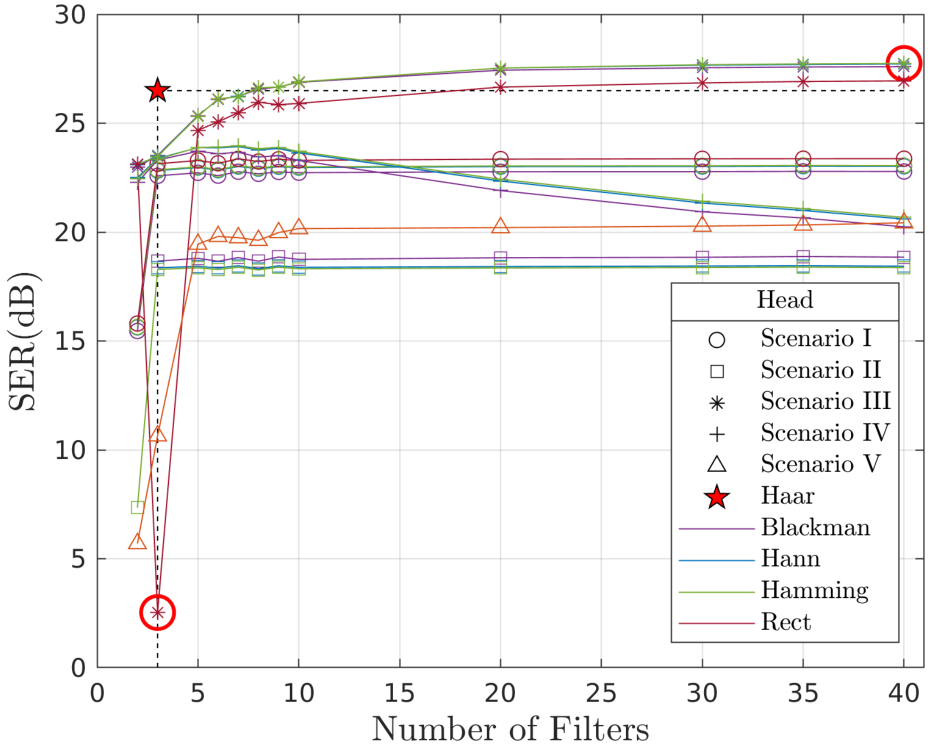

Figure 4.13. SER results for the reconstruction of the Head image in a radial trajectory. The red circles highlight the highest and lowest SER for the image. The red star is the result of the reconstruction of the Head image with the Haar filters.

Table 4.1. SER and SSIM results for the reconstruction using CS with prefiltering with Haar filters in the scheme 3 set up as in [37], and prefiltering with directional filters, and the reconstructions with TV from [45].

	Haar		TV		Directional	
Images	SER_{dB}	SSIM	SER_{dB}	SSIM	SER_{dB}	SSIM
Shepp-Logan	135	1	114.9	1	28.7	0.98
Brain	39.2	0.420	37.4	0.516	31.5	0.369
Head	26.5	0.580	22.1	0.481	27.7	0.592

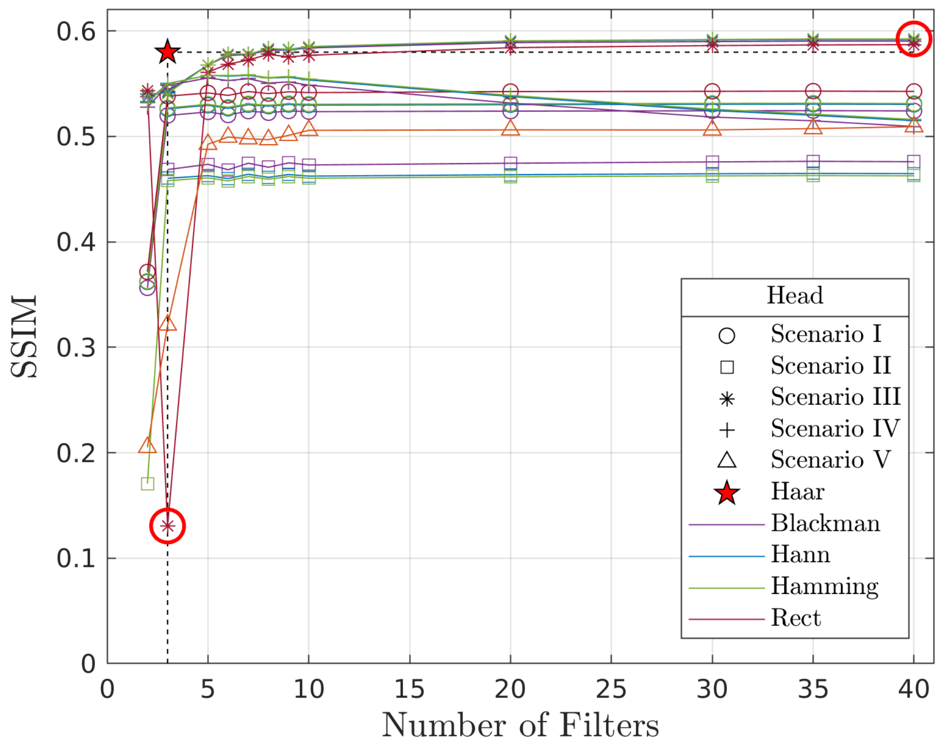

Figure 4.14. SSIM results for the reconstruction of the Head image in a radial trajectory. The red circles highlight the highest and lowest SSIM for the image. The red star is the result of the reconstruction of the Head image with the Haar filters.

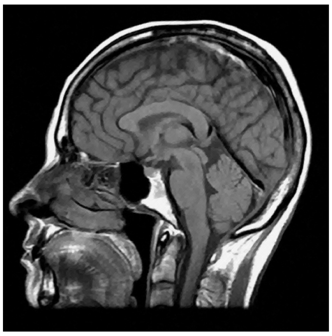

(a) SER = 26.5 dB, SSIM = 0.580.

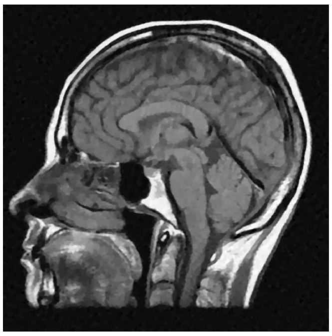

(b) SER = 22.1dB, SSIM = 0.481.

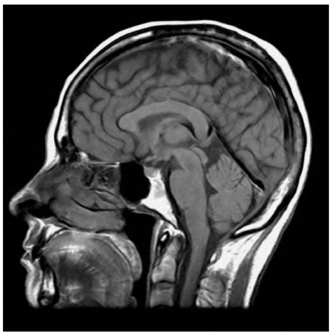

(c) SER = 27.7 dB, SSIM = 0.592.

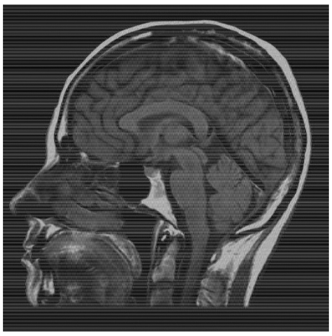

(d) SER = 2.53 dB, SSIM = 0.130.

Figure 4.15. Reconstructions of the Head image. In **(a)** we have the reconstruction for the Haar filters, in **(b)** we have the reconstruction with TV, in **(c)** we have the best reconstruction result for the directional filters, where the reconstruction is from the set of 40 filters windowed by Hamming in scenario III, in **(d)** we have the worst reconstruction result for the directional filters, where the reconstruction is from the set of 3 filters windowed by a rectangular window in scenario III.

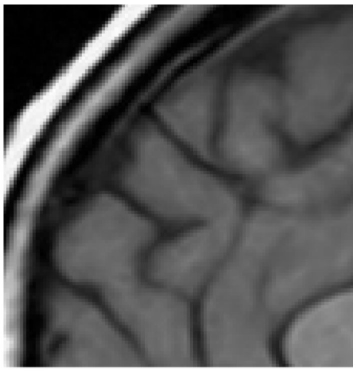

(a) Original. **(b)** Directional.

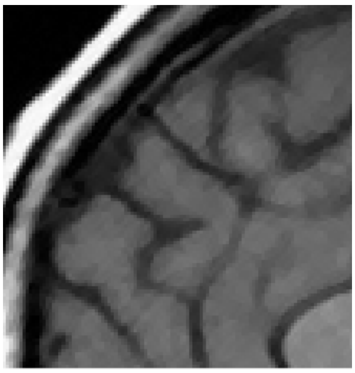

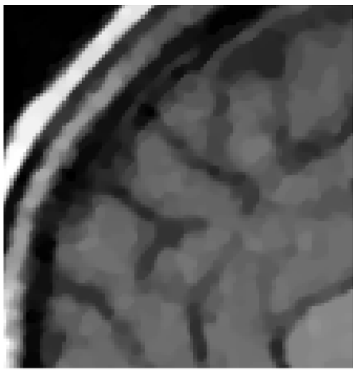

(c) Haar. **(d)** TV.

Figure 4.16. Detail comparison of the reconstructed image of the head and the original image. In **(a)** we have the original image of the head, in **(b)** we have the best reconstruction result for the directional filters, where the reconstruction is from the set of 40 filters windowed by Hamming in scenario III, in **(c)** we have the reconstruction for the Haar filters, and in **(d)** we have the reconstruction with TV.

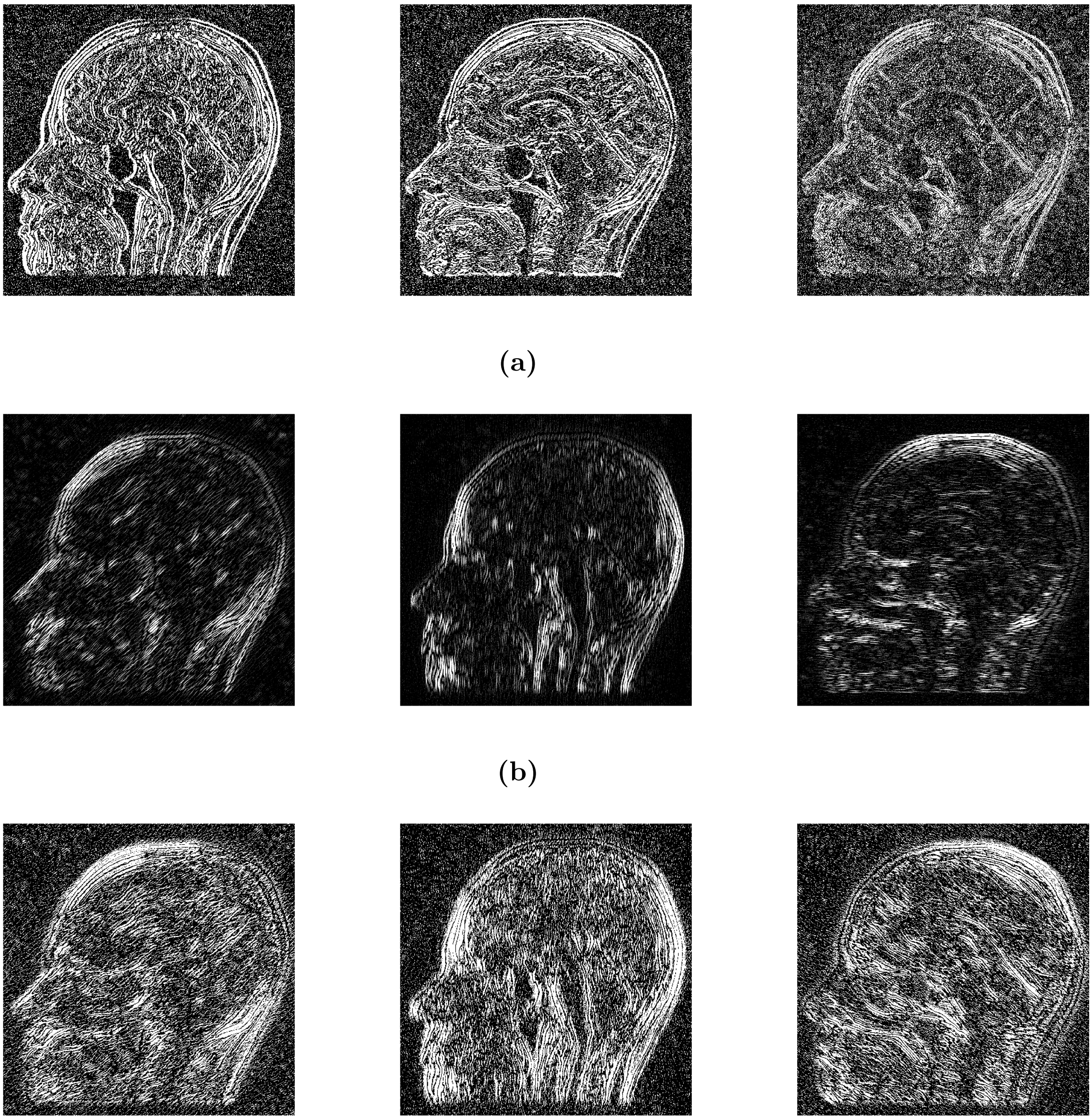

Figure 4.17. Reconstructed sparse xf_n components of the Head image. In **(a)** we have the three sparse components used to compose the final image, in **(b)** we have the three xf_n versions ($n = [10, 20, 30]$) for the Directional filter with best results, in **(c)** we have the three xf_n versions ($n = [10, 20, 30]$) for the Directional filter with worst results.

Finally, the reconstructions from measures acquired in a k-space spiral trajectory reinforced the results from the radial trajectory, however, the quality of the image showed improvements for both Haar and directional filters. For the Haar filter the gain was of 2.1 dB in SER and 0.193 in SSIM, on the other hand, the directional filter gain was of 2.5 dB in SER and 0.03 in SSIM. This is an interesting result since the spiral trajectory acquired slightly less measures than the radial trajectory, a difference of 0.13% in the number of measures. The Figures 4.19 and 4.20 display the graphical results of SER and SSIM for the reconstructions of the Head image with measures acquired in a spiral trajectory with exponential growth. The Figures 4.22a, 4.22b, and 4.22c, show the reconstructed images for the Haar filter, the directional filter with 40 filters in the set, windowed by the Hamming window in scenario III and the worst reconstruction for the directional filter with 3 filters in the set, windowed by a rectangular window in scenario III, the same filters from the previous experiment, but in this case with spiral trajectory. Also, in Figures 4.24a, 4.24b, and 4.24c, we present some of the xf_n reconstructions for the Haar and directional filters. Similar to the xf_n from the images reconstructed from measures in a radial trajectory, we can tell that the images are differents from each other, however we cannot visually define with precision which are the sparsest versions. In the Table 4.2, we summarize the SER and SSIM results for the Haar and directional filters for both k-space trajectories.

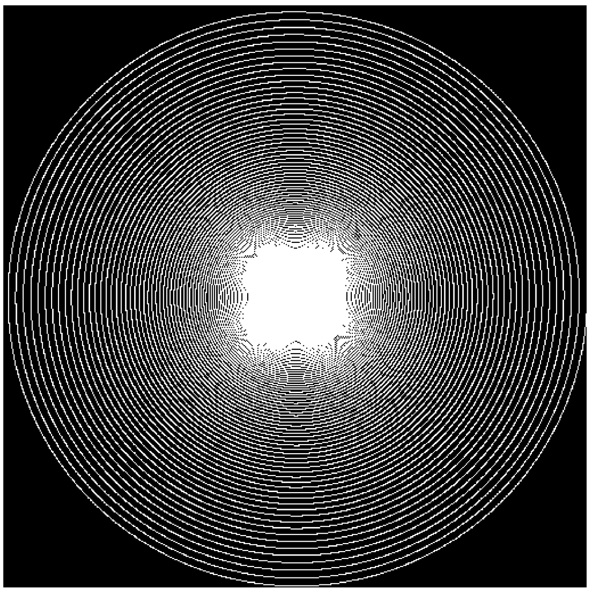

Figure 4.18. Representation of an spiral trajectory with radius growth and 180 turns representing $\approx$ 23.55% of the possible measurements for an image of size 512×512.

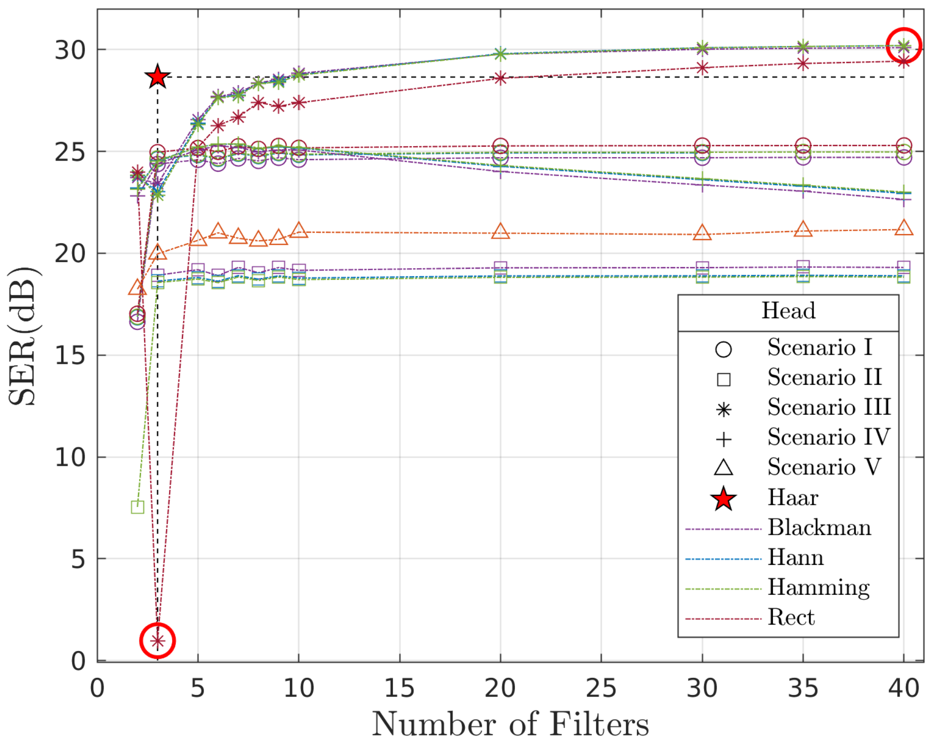

Figure 4.19. SER results for the reconstruction of the Head image in a spiral trajectory. The red circles highlight the highest and lowest SER for the image. The red star is the result of the reconstruction of the Head image with the Haar filters.

Table 4.2. Summary of the results for reconstructions of the Head image in both radial and spiral trajectory. The directional filter results are the best SER and SSIM results displayed in the graphs 4.13 and 4.14.

	Radial		Spiral	
	SER_{dB}	SSIM	SER_{dB}	SSIM
Haar	26.5	0.580	28.6	0.613
Directional	27.7	0.592	30.2	0.621

The next set of Figures 4.25, 4.26, 4.27, 4.28, and 4.29 present the SER results for all the images reconstructed in this work separated by scenario. The idea is to provide a visual display of how the different design strategies behave reconstructing different images. Overall, the SER results for the Brain phantom were higher than the results for the Shepp-Logan and Head image in the all the scenarios. Considering all scenarios results, in general the graphs are divided by scenarios with the best SER results for the Brain phantom, followed by the results for the Head image and Shepp-Logan phantom, except for the scenario I, where the SER results of the Shepp-Logan phantom reconstructions are higher than the reconstructions for the Head image. To remember, the filters in scenario I are projected from a smooth frequency distribution along all the frequency spectrum and truncated by a window and this setup seem to work better for piecewise continuous images than for a real image. Categorically in scenario IV, to increase the

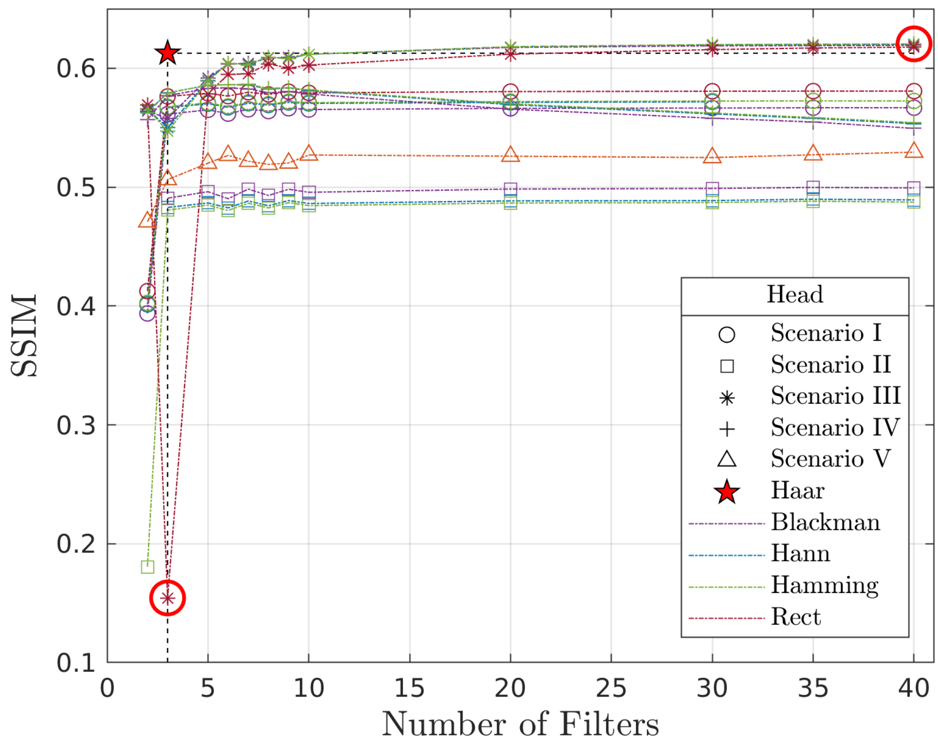

Figure 4.20. SSIM results for the reconstruction of the Head image in a spiral trajectory. The red circles highlight the highest and lowest SSIM for the image. The red star is the result of the reconstruction of the Head image with the Haar filters.

number of filters degraded the quality of the reconstructions. For the Head image the loss in SER was of 3 dB and for the Shepp-Logan was of 5.3 dB. The filers in Scenario V are implemented in the frequency domain from an ideal frequency response distribution and the results suggest that for real images the degradation suffered by adding more filters, which results in dividing the frequency spectrum in smaller ranges, is less aggressive than for piecewise continuous images.

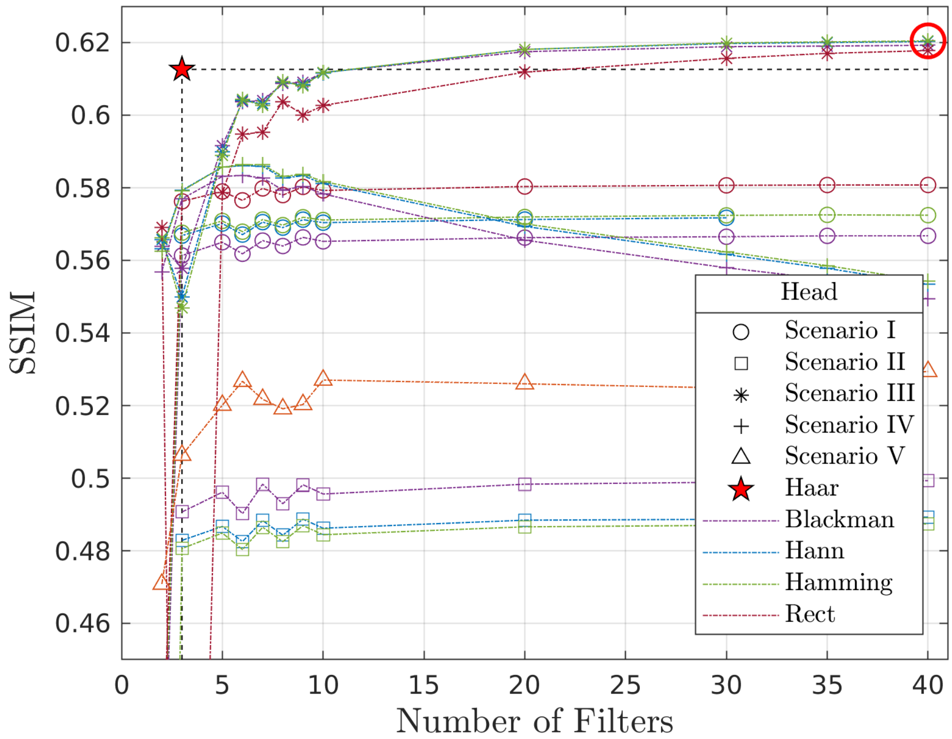

Figure 4.21. Zoomed in view of the upper graphs in SSIM results for the reconstruction of the Head image in a spiral trajectory. The red circle highlights the highest and lowest SSIM for the image. The red star is the result of the reconstruction of the Head image with the Haar filters.

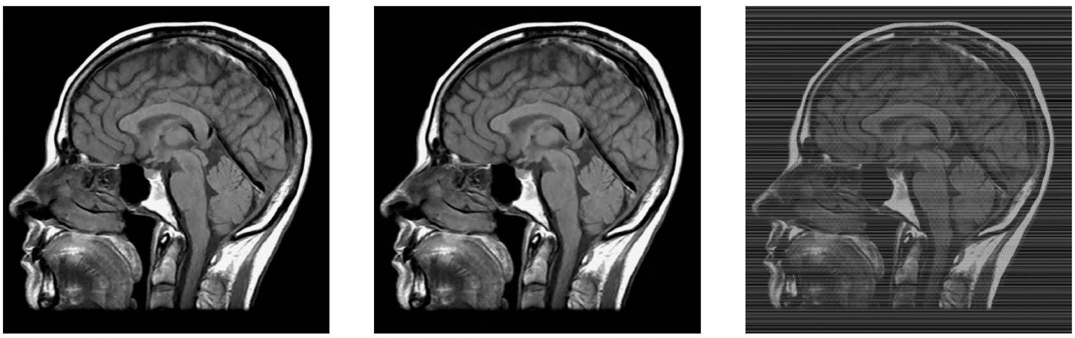

(a) SER = 28.6 dB, SSIM = 0.613.

(b) SER = 30.2 dB, SSIM = 0.621.

(c) SER = 0.97 dB, SSIM = 0.154.

Figure 4.22. Reconstructions of the Head image in spiral trajectory measure acquisition. In **(a)** we have the reconstruction for the Haar filters, in **(b)** we have the best reconstruction result for the directional filters, where the reconstruction is from the set of 40 filters windowed by Hamming in scenario III, in **(c)** we have the worst reconstruction result for the directional filters, where the reconstruction is from the set of 3 filters windowed by a rectangular window in scenario III.

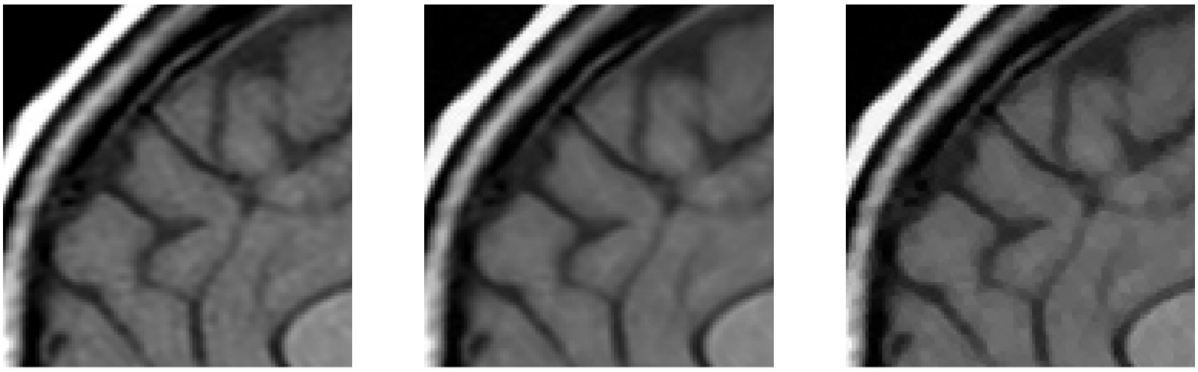

(a) Original. **(b)** Directional. **(c)** Haar.

Figure 4.23. Detail comparison of the reconstructed image of the head from measures acquired in a spiral trajectory and the original image. In **(a)** we have the original image of the head, in **(b)** we have the best reconstruction result for the directional filters, where the reconstruction is from the set of 40 filters windowed by Hamming in scenario III, in **(c)** we have the reconstruction for the Haar filters.

(a)

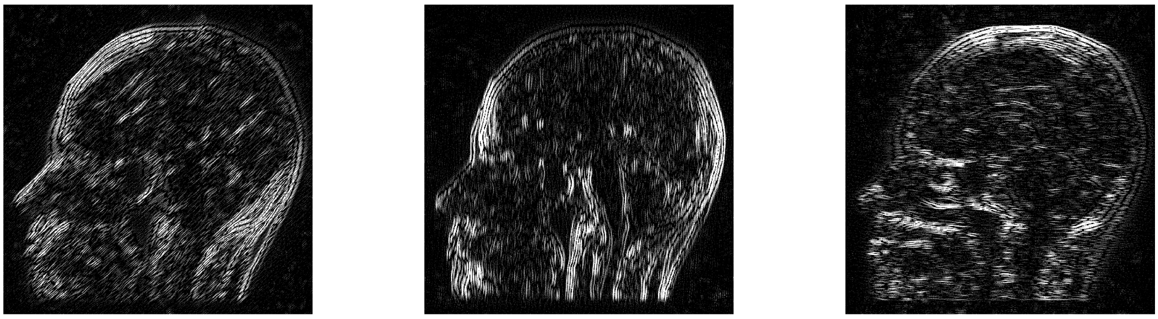

(b)

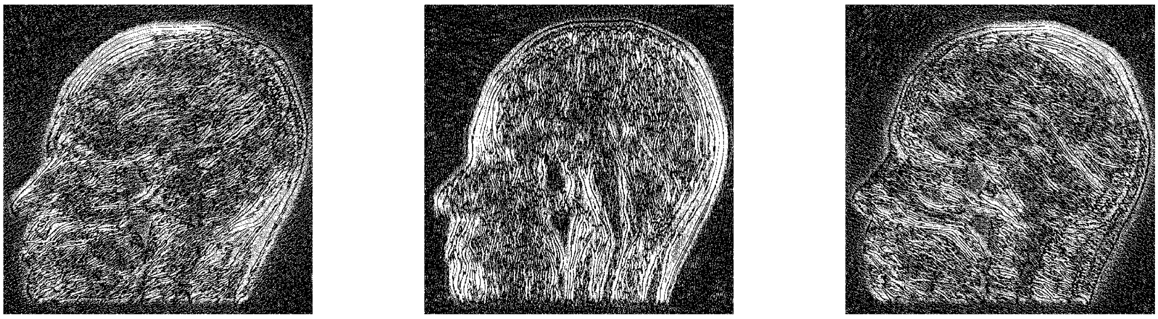

(c)

Figure 4.24. Reconstructed sparse xf_n components of the Head image with measurements acquired in a spiral trajectory. In **(a)** we have the three sparse components used to compose the final image, in **(b)** we have the three xf_n versions ($n = [10, 20, 30]$) for the Directional filter with best results, in **(c)** we have the three xf_n versions ($n = [10, 20, 30]$) for the Directional filter with worst results.

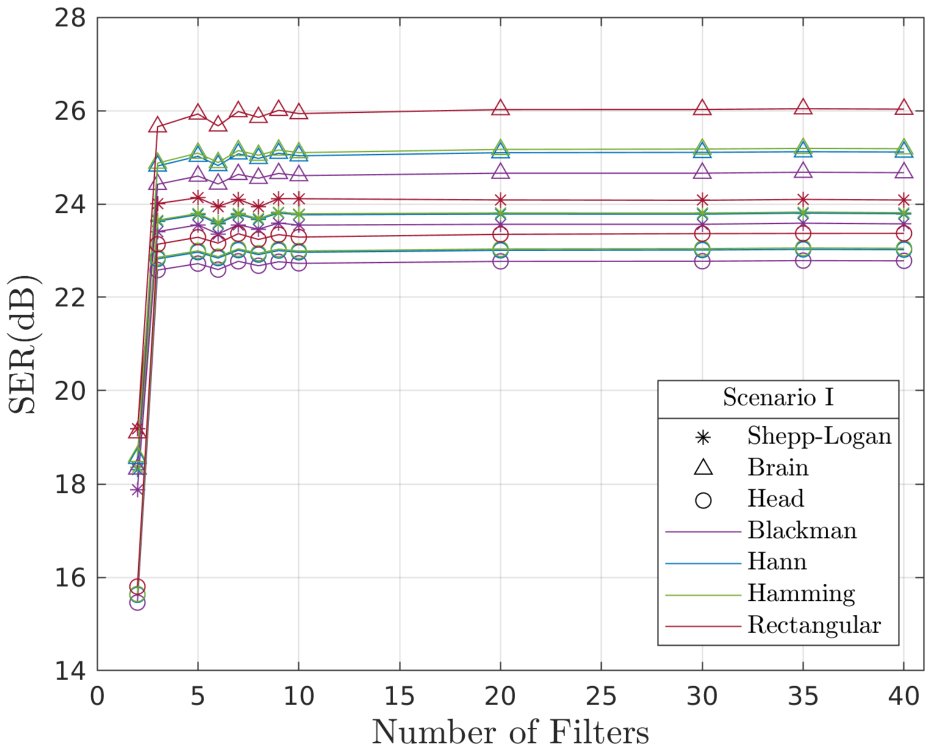

Figure 4.25. SER results for the Shepp-Logan, Brain and Head images in scenario I.

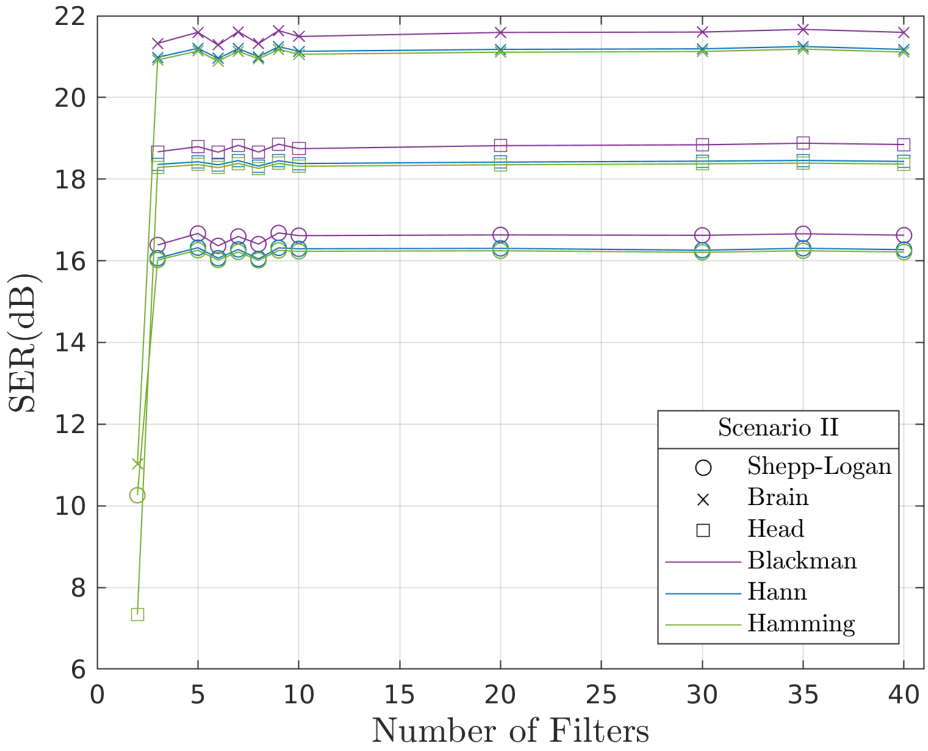

Figure 4.26. SER results for the Shepp-Logan, Brain and Head images in scenario II.

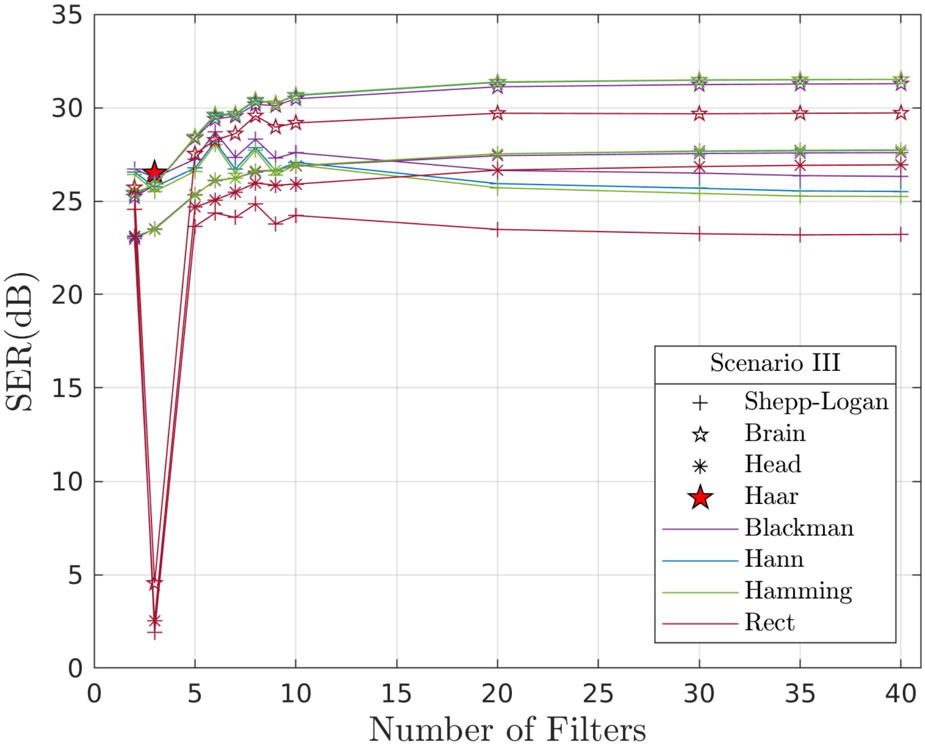

Figure 4.27. SER results for the Shepp-Logan, Brain and Head images in scenario III. The Haar SER result is for the reconstruction of the Head image.

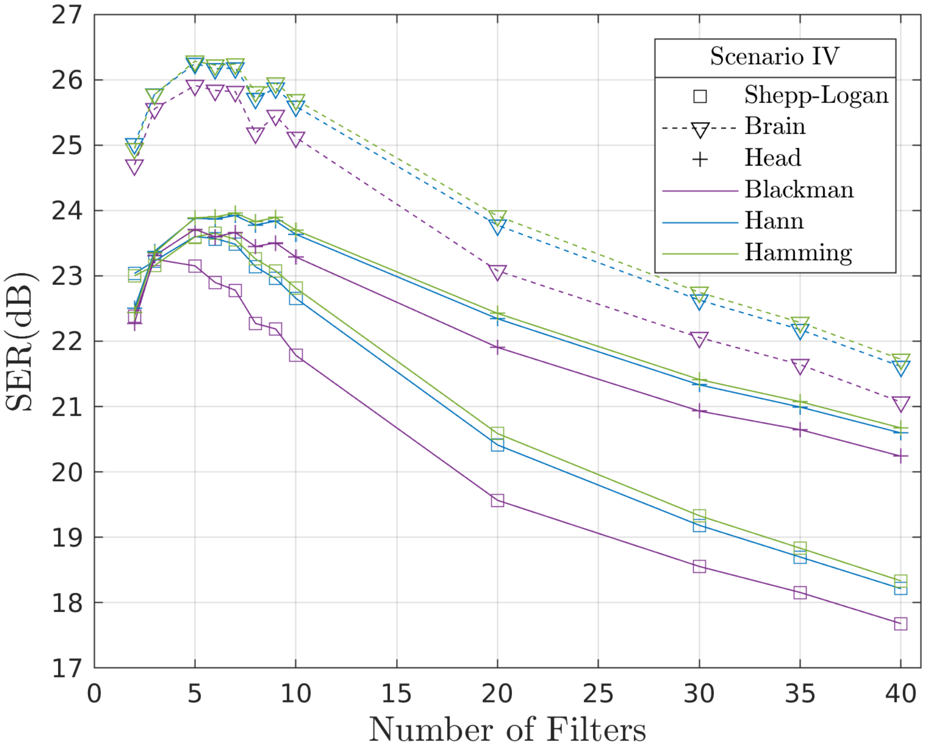

Figure 4.28. SER results for the Shepp-Logan, Brain and Head images in scenario IV.

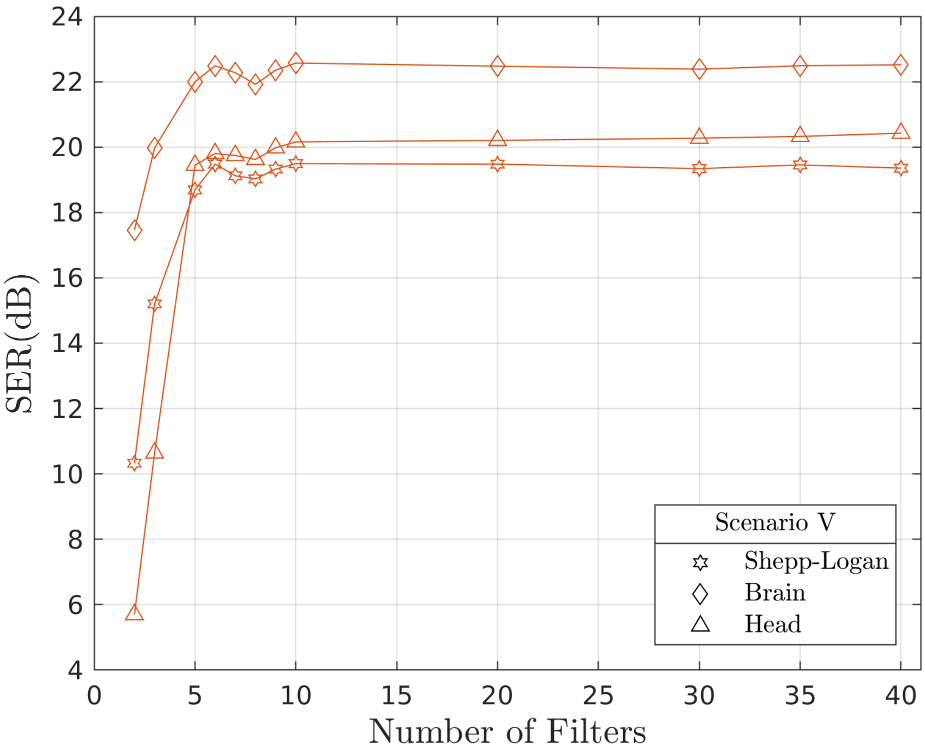

Figure 4.29. SER results for the Shepp-Logan, Brain and Head images in scenario IV.

Scenario I	Scenario II	Scenario III	Scenario IV	Scenario V
Projecting Directional Filters from a Smooth Frequency Distribution Along all Frequency Spectrum	Implementing Directional Filters from Smooth Windows Distributions Along all Frequency Spectrum	Projecting Directional Filters From an Ideal Frequency Response	Implementing Directional Filters From a Smooth Frequency Distribution in a Range of the Frequency Spectrum	Implementing Directional Filters From an Ideal Frequency Response Distribution
$H_{1d} = \begin{cases} Distribution\ from\ 0\ to\ \pi: \\ 0.5 + 0.5cos(2x - \pi), \end{cases}$ $H_{2d} = \begin{cases} Distribution\ from\ \pi\ to\ 2\pi: \\ 0.5 + 0.5cos(2x - \pi), \end{cases}$	$H_{1d} = \begin{cases} Distribution\ from\ 0\ to\ \pi: \\ 0.5 + 0.5cos(2x - \pi)\ or \\ 0.54 + 0.5cos(2x - \pi)\ or \\ 0.42 + 0.5cos(2x - \pi) + 0.08cos(4x - \pi). \end{cases}$	$h_{1d}[n_1, n_2] = \int_{\theta_{min}}^{\theta_{max}} \int_0^R re^{j2(cos\theta_{n1} + sin\theta_{n2})} drd\theta$ $h_1 = h_{1d}w,\ where\ w\ is\ the\ window\ type.$	$H_{1d} = \begin{cases} Distribution\ from\ \theta_{min}\ to\ \theta_{max}: \\ 0.5 + 0.5cos(2x - \pi)\ or \\ 0.54 + 0.5cos(2x - \pi)\ or \\ 0.42 + 0.5cos(2x - \pi) + 0.08cos(4x - \pi). \end{cases}$	$H_{1d} = \begin{cases} 1, \theta_{min}\ to\ \theta_{max} \\ 0,\ otherwise \end{cases}$
$H_d = H_{1d} + H_{2d}$ $hd[n_1, n_2] = D^{-1}\{H_d[n_1, n_2]\}$	$H_{2d} = \begin{cases} Distribution\ from\ \pi\ to\ 2\pi: \\ 0.5 + 0.5cos(2x - \pi)\ or \\ 0.54 + 0.5cos(2x - \pi)\ or \\ 0.42 + 0.5cos(2x - \pi) + 0.08cos(4x - \pi). \end{cases}$	$h_{2d}[n_1, n_2] = \int_{\theta_{min} + \pi}^{\theta_{max} + \pi} \int_0^R re^{j2(cos\theta_{n1} + sin\theta_{n2})} drd\theta$ $h_2 = h_{2d}w,\ where\ w\ is\ the\ window\ type.$	$H_{2d} = \begin{cases} Distribution\ from\ \theta_{min} + \pi\ to\ \theta_{max} + \pi: \\ 0.5 + 0.5cos(2x - \pi)\ or \\ 0.54 + 0.5cos(2x - \pi)\ or \\ 0.42 + 0.5cos(2x - \pi) + 0.08cos(4x - \pi). \end{cases}$	$H_{2d} = \begin{cases} 1,\ \theta_{min} + \pi\ to\ \theta_{max} + \pi \\ 0,\ otherwise \end{cases}$
$h = h_d w$, *where w is the window type.* *H is the Discrete Fourier Transform (DFT) of h with size equal to the image size.*	*Choose the same distribution for H_{1d} and H_{2d}.* $H = H_{1d} + H_{2d}$	$h = h_1 + h_2$ *H is the Discrete Fourier Transform (DFT) of h with size equal to the image size.*	*Choose the same distribution for H_{1d} and H_{2d}.* $H = H_{1d} + H_{2d}$	$H = H_{1d} + H_{2d}$

Figure 4.30. Summary of the steps to design each filter scenario.

Chapter 5

Conclusion

In this research, we evaluated different strategies to design directional filters. We first started from filters with smooth transitions all along the frequency domain, first in scenario I projecting filters from an ideal frequency response characterized by a smooth distribution following the Hann equation and them truncating the filter by windowing them with Hann, Hamming, Blackman and rectangular windows. Then, in scenario II we implemented the filters in the frequency domain following smooth distributions defined by the equations of the Hann, Hamming and Blackman window. These first two strategies where evaluated reconstructing phantoms from measurements acquired in a radial trajectory in the k-space.

When comparing these strategies to the reconstructions with prefiltering using Haar filters, the results were not positive for directional filters, since TV and CS with prefiltering using separable filters reconstructed both phantoms with way higher SER and SSIM values. However, we noticed that the SER results for the directional filters were higher with the Brain phantom than the Shepp-Logan phantom. Thus, it is important to evaluate what each quality index assess in terms of quality. When calculating the SER, we are in practice assessing the signal error between a reference signal and the distorted one. In fact, what the quality indexes were saying is that in general, for the Brain phantom the directional filters were able to present a small error signal in the reconstruction, however, they were not able to preserve the structural similarity so well as what it did for the Shepp-Logan phantom.

In the second part of the research, we proposed three other strategies to design directional filters keeping the filter impulse response in a range of the frequency spectrum, equally divided between the numbers of filters in the set. In scenario III, we projected filters from an ideal frequency response distribution and windowed them with the Hann, Hamming, Blackman and rectangular windows. Next, in scenario IV, we implemented filters from a smooth transition in a range of the frequency spectrum and finally, in scenario V we also implemented a set of filters from an ideal frequency response distribution in a range of the DFT. When comparing the performance of all the filters strategies in reconstructing a real image of the head, the filters in scenario III, showed better results in terms of image quality when compared to Haar filters. We relate this result to the ability of the directional filters in extracting features such as boundaries, edges, ridges, textures at different orientations of the image, and thus this ability favors the sparsity in each filtered version of the b_f measures, hence, simplifying the process of solving the lp minimization for each filtered version of the final reconstructed images. Equally important, the reconstructions from measures acquired in a spiral trajectory with exponential growth presented higher SER and SSIM results, even with a decrease of 0.13% measures compared to the radial trajectory.

Besides the filters strategies proposed in this work, we also tested some other different design strategies as emulating the spectral filling of the Haar filters with directional filters, we also tested the directional filters without the mirrored symmetry, and the results were below the SER and SSIM acquired with the Haar filters.

In future a research we think that windowing the filters in scenario III with Kaiser windows could improve the reconstruction quality even more, since with this window we have parameters to specifically interfere in the size of the ripples, in the stopband, caused by the truncation of the DTFT. Also, we think that exploring other strategies to project smooth filters as the project of filters with smooth transitions proposed by Burrus could show promising results. Further, in future researchers the directional filters should be tested with measures that are more realistic acquired in non-cartesian grids to approximate the results to realistic situations on magnetic resonance imaging reconstructions.

5.1 Considerations to Select a Filter

When conducting this research we had the opportunity to test different strategies to design directional filters and explore different ways to divide the frequency spectrum of the reconstructed images and also to compare the reconstructions with directional and separable filters and from that we acquire an sense of discernment to choose a more fitting filter for CS with prefiltering. We start these considerations by reflecting on the source of the measurements from where we want to reconstruct an image.

Starting from a piecewise continuous phantom, some researches argue that they overestimate the performance of the reconstructions algorithms, however, we want to consider the reconstruction of measurements from a phantom used to calibrate and test the MRI scan equipment, or even different types of phantoms for studies purpose. Some of these phantoms are piecewise continuous and then to properly reconstruct measurements from them we should use Haar filters in the prefiltering stage. For informations regarding the Reconstruction Time (RT) refer to Appendix A and for the hardware configurations where the reconstructions were conducted refer to Appendix B.

Further, when considering biological tissues or phantoms that emulate the complexity of biological tissues with different segments of information in small sections the directional seen to be a better fit in the prefiltering stage due to its ability to acquire information as ridges, edges and etc. Also, we want to take in account some considerations regarding the quality indexes and the RT. To see the RT, refer to Table 5 in Appendix A. To estimate the approximated reconstruction time for an equipment similar to the one used in this research we calculate $n \times RT_{mean}$, where n is the number of filters in the set and RT_{mean} is the average reconstruction time.

As an example, we refer to the best reconstruction result for the Head image with measures acquired in a spiral trajectory, see Figure 4.19. To this example, the total reconstruction time for serial reconstructions is of $40 \times 6.63 \approx 4$ hours and 25 minutes. However, using an parallelized algorithm the total reconstruction time is the RT_{max}. The quality indexes results for this reconstruction is SER of 27.7 dB and SSIM of 0.592. Whereas reconstructing the same image with half the number of filters results in SER 0f 27.5 dB and SSIM of 0.590 and total reconstruction time of $20 \times 6.73 \approx 2$ hours and 14 minutes, almost half the time of the reconstruction with 40 filters for a gain of 0.2 dB in SER and 0.002 in SSIM. For serial reconstructions, the number of filters in the set easily increase the total reconstruction time from minutes to hours and this should be a concern depending on the research scope. On the other hand, parallel reconstructions benefit from the fact that the total reconstruction time will take as long as the single most time consuming reconstruction, although the more number of filters used, the more time the composition stage will request to compose the final image

5.2 Research challenges

When we decided to conduct this research we had in mind the idea that directional filters could be able to provide sparse xf_n versions in the prefiltering stage of the reconstructions due to its ability to provide borders, ridges, edges and etc. However, we did not know by then what was the best way to design the directional filters and how it could impact in the final reconstructed images and we started from different approaches considering an smooth distribution along all the frequency spectrum because we believe at first that the smoother the filters transitions the sparse the filtered images. From testing and experimenting with different parameters we proposed the five scenarios and systematically tested them with different numbers of filters and directional positions for three images with measures acquired in a radial trajectory and after with a spiral trajectory.

Due to the empirical nature of the study, a great challenge was the time required to reconstruct the images and the fact that the reconstructions are computationally demanding and we only had access to a cluster near to the deadline to conclude the research and this limited the number of experiments with different images and trajectories. In a future work, we want to explore the five proposed scenarios reconstructing images from an image bank with different images of different parts of the human body exploring different k-space trajectories.

Appendices

A Reconstruction Time Results

The following tables are divided in lines by the reconstructed images (Shepp-Logan, Brain and Head) with measures b acquired in a radial trajectory, except for Head*, where the measures b were acquired in a spiral trajectory. The rows are divided, according to each scenario, by the type of window used to truncate the filters or the smooth distribution, the number of filters and the RT results. $RT_{Max}[min]$ is the maximum reconstruction time of Xf_n for each set of n filters. $RT_{Mean}[min]$ is the average RT for the set of filters and $RT_{\sigma}[min]$ is the RT standard deviation (σ) of the filters in the set. The grey lines are the results of the reconstructions in the Virgo Cluster and the white lines are the results for the reconstruction in an Asus k45Vm notebook, hardware info is in Appendix B.

Table 1

Haar	Nº of Filters	$RT_{Max}[min]$	$RT_{Mean}[min]$	$RT_{\sigma}[min]$
Shepp-Logan	3	1.33	1.15	0.18
Brain	3	5.31	4.22	1.26
Head	3	4.20	3.57	0.57
Head*	3	7.32	6.79	0.47

Table 2. Reconstruction time in Scenario I.

Scenario I	Window Type	Nº of Filters	$RT_{Max}[min]$	$RT_{Mean}[min]$	$RT_{\sigma}[min]$
Shepp-Logan	Blackman	2	7.27	7.22	0.07
		3	7.19	6.92	0.25
		5	7.43	7.09	0.32
		6	7.64	7.16	0.27
		7	7.74	7.23	0.40
		8	8.41	7.47	0.62
		9	7.98	7.19	0.44
		10	7.54	7.26	0.27
		20	21.43	8.93	3.61
		30	29.10	9.19	4.56
		35	8.66	7.40	0.43
		40	8.33	7.28	0.43
	Hann	2	7.29	7.13	0.22
		3	7.77	7.27	0.44
		5	7.38	7.01	0.33
		6	7.39	7.04	0.30
		7	7.79	7.21	0.50
		8	8.65	7.37	0.74

Table 2 continued from previous page

Scenario I	Window Type	Nº of Filters	$RT_{Max}[min]$	$RT_{Mean}[min]$	$RT_{\sigma}[min]$
		9	8.00	7.09	0.50
		10	7.44	6.98	0.33
		20	8.28	7.08	0.46
		30	7.75	6.73	0.45
		35	8.36	7.13	0.52
		40	28.10	9.52	4.29
	Hamming	2	7.66	7.39	0.38
		3	8.00	7.51	0.43
		5	8.28	7.62	0.53
		6	7.82	7.49	0.35
		7	7.97	7.35	0.51
		8	8.17	6.88	0.79
		9	7.35	6.54	0.43
		10	7.01	6.54	0.30
		20	7.77	6.55	0.47
		30	11.56	7.21	1.22
		35	11.33	8.15	1.21
		40	9.81	7.70	0.72
	Rect	2	7.29	7.19	0.14
		3	43.44	18.50	21.65
		5	24.96	9.94	8.45
		6	7.04	6.33	0.39
		7	7.23	6.69	0.47
		8	8.72	7.49	0.88
		9	59.16	12.37	17.56
		10	165.38	22.14	50.34
		20	8.04	6.65	0.60
		30	10.19	7.70	1.34
		35	7.82	6.40	0.59
		40	7.62	6.30	0.53
Brain	Blackman	2	4.50	4.36	0.21
		3	4.67	4.41	0.25
		5	4.58	4.37	0.16
		6	4.75	4.33	0.34
		7	4.62	4.30	0.21
		8	4.59	4.31	0.18
		9	4.48	4.21	0.19

Table 2 continued from previous page

Scenario I	Window Type	Nº of Filters	$RT_{Max}[min]$	$RT_{Mean}[min]$	$RT_{\sigma}[min]$
		10	4.46	4.16	0.22
		20	4.51	4.14	0.18
		30	4.43	4.13	0.19
		35	4.39	4.11	0.18
		40	4.59	4.18	0.18
	Hann	2	4.36	4.23	0.19
		3	4.34	4.24	0.15
		5	4.75	4.37	0.27
		6	4.83	4.50	0.29
		7	4.92	4.54	0.29
		8	8.42	5.83	1.61
		9	8.69	5.36	1.33
		10	6.19	4.82	0.57
		20	5.22	4.78	0.32
		30	14.74	6.27	2.88
		35	11.48	5.07	1.71
		40	8.82	4.60	0.76
	Hamming	2	4.21	4.15	0.07
		3	4.23	4.12	0.15
		5	4.24	4.01	0.25
		6	4.25	4.04	0.21
		7	4.62	4.26	0.28
		8	7.85	5.62	1.10
		9	6.00	5.47	0.42
		10	15.74	7.78	4.61
		20	11.21	5.04	1.59
		30	11.24	5.01	1.89
		35	9.09	5.78	1.22
		40	10.59	5.51	1.22
	Rect	2	3.39	3.22	0.25
		3	3.82	3.69	0.17
		5	4.88	4.23	0.47
		6	5.63	5.01	0.55
		7	5.78	5.39	0.46
		8	5.41	5.19	0.20
		9	5.54	4.63	0.61
		10	8.63	5.31	1.24

Table 2 continued from previous page

Scenario I	Window Type	Nº of Filters	$RT_{Max}[min]$	$RT_{Mean}[min]$	$RT_{\sigma}[min]$
		20	5.64	4.42	0.34
		30	4.41	4.15	0.19
		35	4.50	4.12	0.20
		40	5.90	4.16	0.40
Head	Blackman	2	7.68	7.67	0.02
		3	7.85	7.32	0.48
		5	7.86	7.29	0.55
		6	7.78	7.26	0.42
		7	7.66	7.07	0.40
		8	7.69	7.17	0.35
		9	7.72	7.14	0.37
		10	7.86	7.25	0.43
		20	7.75	7.17	0.34
		30	7.89	7.21	0.35
		35	7.95	7.22	0.36
		40	7.79	7.13	0.34
	Hann	2	7.17	7.09	0.11
		3	7.48	7.02	0.41
		5	7.46	6.95	0.51
		6	7.41	6.79	0.50
		7	7.34	6.96	0.37
		8	7.25	6.89	0.35
		9	7.34	6.87	0.33
		10	7.50	6.91	0.43
		20	7.46	6.89	0.35
		30	7.31	6.78	0.29
		35	7.39	6.82	0.30
		40	7.30	6.73	0.31
	Hamming	2	7.33	7.21	0.17
		3	7.27	6.85	0.38
		5	7.44	6.88	0.52
		6	7.44	6.94	0.44
		7	7.39	6.98	0.40
		8	7.15	6.71	0.35
		9	6.98	6.65	0.26
		10	7.27	6.66	0.41
		20	7.33	6.76	0.33

Table 2 continued from previous page

Scenario I	Window Type	Nº of Filters	$RT_{Max}[min]$	$RT_{Mean}[min]$	$RT_{\sigma}[min]$
		30	7.37	6.77	0.32
		35	7.35	6.72	0.32
		40	7.21	6.65	0.31
	Rect	2	6.45	6.43	0.02
		3	7.30	6.91	0.43
		5	6.73	6.17	0.46
		6	6.48	6.12	0.29
		7	6.51	6.10	0.41
		8	6.53	6.08	0.42
		9	6.71	6.12	0.34
		10	6.65	6.20	0.37
		20	6.56	6.12	0.33
		30	6.77	6.16	0.32
		35	6.88	6.06	0.36
		40	6.66	6.11	0.32
Head*	Blackman	2	8.91	8.90	0.01
		3	8.91	8.82	0.08
		5	9.72	9.03	0.43
		6	9.45	8.95	0.28
		7	9.38	8.93	0.38
		8	9.20	8.94	0.19
		9	9.35	8.97	0.25
		10	9.47	8.81	0.33
		20	9.81	9.00	0.31
		30	9.67	8.98	0.27
		35	9.53	8.93	0.25
		40	9.78	9.00	0.29
	Hann	2	8.66	8.55	0.16
		3	8.58	8.47	0.14
		5	8.79	8.52	0.28
		6	9.05	8.64	0.30
		7	8.93	8.53	0.28
		8	8.81	8.56	0.20
		9	8.78	8.53	0.17
		10	8.69	8.42	0.20
		20	8.79	8.44	0.21
		30	9.55	8.56	0.29

Table 2 continued from previous page

Scenario I	Window Type	Nº of Filters	$RT_{Max}[min]$	$RT_{Mean}[min]$	$RT_{\sigma}[min]$
	Hamming	2	8.47	8.40	0.10
		3	8.56	8.48	0.09
		5	8.53	8.34	0.27
		6	8.51	8.28	0.20
		7	8.73	8.39	0.19
		8	8.67	8.40	0.16
		9	8.63	8.49	0.11
		10	8.57	8.39	0.16
		20	8.68	8.32	0.21
		30	8.77	8.34	0.22
		35	8.72	8.31	0.19
		40	8.58	8.23	0.16
	Rect	2	7.32	7.28	0.05
		3	7.33	7.29	0.03
		5	7.53	7.31	0.23
		6	7.36	7.23	0.08
		7	7.48	7.34	0.13
		8	7.65	7.37	0.21
		9	7.74	7.38	0.18
		10	7.56	7.25	0.24
		20	7.77	7.35	0.24
		30	7.72	7.36	0.20
		35	7.75	7.36	0.19
		40	7.67	7.31	0.19

Table 3. Reconstruction time in Scenario II.

Scenario II	Distribution	Nº of Filters	$RT_{Max}[min]$	$RT_{Mean}[min]$	$RT_{\sigma}[min]$
Shepp-Logan	Blackman	2	7.75	7.03	1.02
		3	4.56	4.43	0.12
		5	4.74	4.39	0.28
		6	4.82	4.34	0.27
		7	4.83	4.46	0.29
		8	4.95	4.48	0.31
		9	5.00	4.37	0.33
		10	4.58	4.27	0.27
		20	4.61	4.18	0.24

Table 3 continued from previous page

Scenario II	Distribution	Nº of Filters	$RT_{Max}[min]$	$RT_{Mean}[min]$	$RT_{\sigma}[min]$
		30	4.85	4.27	0.29
		35	4.70	4.20	0.25
		40	4.91	4.26	0.28
	Hann	2	4.15	3.96	0.27
		3	4.04	3.99	0.09
		5	4.28	3.98	0.19
		6	4.26	4.13	0.18
		7	4.55	4.22	0.27
		8	4.70	4.22	0.34
		9	4.59	4.17	0.26
		10	4.93	4.51	0.34
		20	4.29	3.89	0.21
		30	10.36	5.88	1.43
		35	6.41	4.82	0.57
		40	5.13	4.36	0.41
	Hamming	2	4.29	4.06	0.33
		3	4.09	4.08	0.02
		5	4.48	4.21	0.23
		6	4.29	4.13	0.18
		7	4.51	4.14	0.26
		8	4.63	4.17	0.31
		9	4.71	4.19	0.31
		10	4.55	4.16	0.24
		20	4.63	4.14	0.25
		30	4.62	4.13	0.26
		35	4.65	4.16	0.26
		40	8.94	5.18	1.35
Brain	Blackman	2	3.39	3.09	0.43
		3	3.79	3.68	0.15
		5	3.89	3.77	0.09
		6	4.06	3.77	0.17
		7	3.93	3.62	0.17
		8	4.03	3.70	0.22
		9	4.10	3.73	0.28
		10	4.11	3.80	0.22
		20	4.22	3.82	0.26
		30	7.19	3.93	0.67

Table 3 continued from previous page

Scenario II	Distribution	Nº of Filters	$RT_{Max}[min]$	$RT_{Mean}[min]$	$RT_{\sigma}[min]$
		35	9.36	5.70	1.85
		40	7.13	4.27	0.87
	Hann	2	3.48	3.47	0.03
		3	3.88	3.64	0.36
		5	3.95	3.71	0.24
		6	4.29	3.96	0.21
		7	4.33	3.82	0.25
		8	4.07	3.73	0.22
		9	4.04	3.80	0.28
		10	4.03	3.71	0.26
		20	3.98	3.63	0.21
		30	3.96	3.59	0.24
		35	3.95	3.53	0.21
		40	4.19	3.66	0.24
	Hamming	2	3.56	3.35	0.29
		3	3.72	3.55	0.19
		5	3.91	3.62	0.24
		6	4.27	3.86	0.31
		7	4.16	3.61	0.26
		8	3.94	3.52	0.26
		9	3.88	3.58	0.23
		10	3.99	3.62	0.25
		20	4.07	3.78	0.20
		30	10.35	4.52	1.71
		35	13.02	6.14	2.53
		40	7.34	4.41	0.80
Head	Blackman	2	5.73	5.72	0.02
		3	5.84	5.74	0.09
		5	6.36	5.80	0.41
		6	6.13	5.79	0.19
		7	6.02	5.68	0.21
		8	6.13	5.68	0.27
		9	6.53	5.80	0.36
		10	6.43	5.74	0.36
		20	6.42	5.79	0.30
		30	6.54	5.81	0.34
		35	6.49	5.76	0.32

Table 3 continued from previous page

Scenario II	Distribution	Nº of Filters	$RT_{Max}[min]$	$RT_{Mean}[min]$	$RT_{\sigma}[min]$
		40	6.52	5.73	0.29
	Hann	2	5.54	5.46	0.12
		3	5.55	5.42	0.16
		5	6.10	5.55	0.38
		6	5.82	5.53	0.19
		7	5.78	5.57	0.22
		8	5.93	5.55	0.25
		9	6.20	5.54	0.34
		10	6.16	5.53	0.31
		20	6.14	5.54	0.26
		30	6.35	5.60	0.29
		35	6.31	5.59	0.29
		40	6.28	5.56	0.28
	Hamming	2	5.54	5.45	0.13
		3	5.60	5.47	0.14
		5	5.95	5.46	0.38
		6	5.75	5.51	0.17
		7	5.72	5.53	0.23
		8	5.91	5.50	0.27
		9	6.14	5.54	0.32
		10	6.11	5.51	0.32
		20	6.09	5.48	0.26
		30	6.21	5.57	0.28
		35	6.14	5.49	0.27
		40	6.10	5.46	0.27
Head*	Blackman	2	6.16	6.03	0.18
		3	6.61	6.34	0.24
		5	6.79	6.28	0.37
		6	7.66	6.99	0.41
		7	6.75	6.33	0.27
		8	6.72	6.26	0.29
		9	6.97	6.34	0.37
		10	6.87	6.25	0.38
		20	6.88	6.29	0.35
		30	7.24	6.30	0.36
		35	7.43	6.58	0.39
		40	6.87	6.21	0.31

Table 3 continued from previous page

Scenario II	Distribution	Nº of Filters	$RT_{Max}[min]$	$RT_{Mean}[min]$	$RT_{\sigma}[min]$
	Hann	2	6.01	5.94	0.11
		3	6.31	6.15	0.14
		5	6.68	6.11	0.40
		6	6.60	6.09	0.29
		7	6.60	6.23	0.24
		8	6.53	6.06	0.32
		9	6.81	6.14	0.35
		10	6.61	6.00	0.34
		20	6.63	6.07	0.30
		30	6.68	6.06	0.33
		35	6.84	6.10	0.34
		40	6.70	6.04	0.31
	Hamming	2	6.14	6.01	0.19
		3	6.23	6.11	0.13
		5	6.73	6.13	0.44
		6	6.51	6.08	0.27
		7	6.53	6.15	0.31
		8	6.45	6.02	0.32
		9	6.82	6.12	0.33
		10	6.67	6.01	0.37
		20	6.65	6.06	0.32
		30	6.82	6.09	0.39
		35	6.92	6.07	0.37
		40	6.82	6.10	0.33

Table 4. Reconstruction time of Scenario III.

Scenario III	Window Type	Nº of Filters	$RT_{Max}[min]$	$RT_{Mean}[min]$	$RT_{\sigma}[min]$
Shepp-Logan	Blackman	2	4.61	4.44	0.23
		3	5.19	4.85	0.34
		5	5.39	5.17	0.17
		6	5.51	5.25	0.21
		7	5.57	5.33	0.21
		8	5.60	5.28	0.19
		9	5.60	5.27	0.23
		10	5.86	5.43	0.25
		20	6.32	5.58	0.32

Table 4 continued from previous page

Scenario III	Window Type	Nº of Filters	$RT_{Max}[min]$	$RT_{Mean}[min]$	$RT_{\sigma}[min]$
		30	6.89	6.01	0.43
		35	20.18	7.10	2.56
		40	19.94	6.96	2.78
	Hann	2	4.82	4.66	0.22
		3	6.21	5.79	0.44
		5	7.86	6.18	0.94
		6	8.26	6.58	1.00
		7	6.14	5.94	0.20
		8	11.06	6.93	1.86
		9	8.07	6.60	0.85
		10	6.70	6.23	0.29
		20	6.90	6.19	0.32
		30	15.44	6.97	2.11
		35	7.36	6.19	0.57
		40	6.94	5.83	0.53
	Hamming	2	4.86	4.76	0.13
		3	5.58	5.30	0.41
		5	5.66	5.55	0.09
		6	5.99	5.64	0.34
		7	5.96	5.76	0.19
		8	5.93	5.69	0.14
		9	6.04	5.67	0.27
		10	6.08	5.73	0.26
		20	6.22	5.71	0.29
		30	6.57	5.59	0.41
		35	6.75	5.77	0.47
		40	7.07	6.10	0.41
	Rect	2	4.46	4.31	0.21
		3	4.81	4.62	0.21
		5	5.57	5.16	0.39
		6	15.72	7.51	4.19
		7	19.47	9.99	4.42
		8	20.59	11.23	6.66
		9	19.63	7.14	4.71
		10	14.70	8.24	3.31
		20	8.53	5.38	0.93
		30	6.38	4.99	0.57

Table 4 continued from previous page

Scenario III	Window Type	Nº of Filters	$RT_{Max}[min]$	$RT_{Mean}[min]$	$RT_{\sigma}[min]$
		35	6.03	4.86	0.56
		40	6.25	4.76	0.55
Brain	Blackman	2	3.57	3.24	0.47
		3	4.03	3.78	0.41
		5	4.14	3.90	0.26
		6	4.38	4.03	0.24
		7	4.44	3.94	0.29
		8	4.59	4.21	0.28
		9	4.46	4.03	0.30
		10	4.44	4.02	0.36
		20	16.27	7.39	4.91
		30	4.47	3.94	0.28
		35	4.25	3.72	0.27
		40	4.14	3.65	0.24
	Hann	2	3.66	3.27	0.56
		3	6.03	4.49	1.34
		5	8.11	5.92	1.59
		6	7.32	4.63	1.40
		7	7.78	5.42	1.32
		8	5.86	4.40	0.61
		9	5.05	4.13	0.39
		10	4.22	3.87	0.25
		20	4.37	3.81	0.27
		30	4.46	3.77	0.26
		35	4.34	3.74	0.25
		40	4.32	3.76	0.30
	Hamming	2	3.10	2.91	0.27
		3	3.64	3.39	0.26
		5	3.94	3.64	0.28
		6	4.22	3.77	0.24
		7	4.23	3.77	0.29
		8	4.09	3.80	0.20
		9	4.41	3.90	0.32
		10	4.39	3.99	0.33
		20	9.94	4.43	1.40
		30	157.56	9.63	27.97
		35	4.93	4.21	0.32

Table 4 continued from previous page

Scenario III	Window Type	Nº of Filters	$RT_{Max}[min]$	$RT_{Mean}[min]$	$RT_{\sigma}[min]$
		40	6.73	4.27	0.52
	Rect	2	3.07	2.93	0.19
		3	3.54	3.37	0.21
		5	4.04	3.59	0.34
		6	3.92	3.58	0.29
		7	4.20	3.70	0.27
		8	4.02	3.62	0.21
		9	4.47	3.62	0.34
		10	4.20	3.56	0.36
		20	4.43	3.53	0.38
		30	4.68	3.54	0.45
		35	4.64	3.69	0.44
		40	4.95	3.67	0.45
Head	Blackman	2	4.84	4.80	0.06
		3	5.99	5.88	0.11
		5	6.44	5.94	0.41
		6	6.20	5.87	0.19
		7	6.26	5.82	0.24
		8	6.30	5.87	0.31
		9	6.43	5.97	0.23
		10	6.41	6.05	0.22
		20	6.62	6.03	0.25
		30	7.31	6.04	0.39
		35	6.51	5.97	0.29
		40	7.00	6.06	0.33
	Hann	2	4.76	4.72	0.05
		3	5.52	5.36	0.14
		5	6.26	5.86	0.30
		6	6.39	6.10	0.20
		7	6.53	6.07	0.26
		8	6.48	6.01	0.33
		9	6.52	6.08	0.22
		10	6.51	6.18	0.22
		20	6.76	6.23	0.34
		30	6.89	6.19	0.36
		35	6.84	6.24	0.35
		40	6.94	6.23	0.38

Table 4 continued from previous page

Scenario III	Window Type	Nº of Filters	$RT_{Max}[min]$	$RT_{Mean}[min]$	$RT_{\sigma}[min]$
	Hamming	2	4.74	4.70	0.05
		3	5.45	5.33	0.14
		5	6.15	5.83	0.28
		6	6.38	6.11	0.19
		7	6.53	6.09	0.26
		8	6.60	6.14	0.37
		9	6.50	6.08	0.23
		10	6.69	6.36	0.24
		20	6.98	6.38	0.36
		30	7.20	6.41	0.41
		35	6.95	6.29	0.39
		40	6.90	6.22	0.36
	Rect	2	5.13	4.97	0.22
		3	6.92	6.36	0.49
		5	7.81	7.09	0.61
		6	7.79	7.13	0.70
		7	7.96	7.30	0.54
		8	8.32	7.48	0.65
		9	8.10	7.45	0.62
		10	8.29	7.43	0.57
		20	8.57	7.19	0.84
		30	8.82	7.03	0.90
		35	8.86	7.04	0.87
		40	9.14	7.14	0.90
Head*	Blackman	2	5.00	4.98	0.03
		3	5.54	5.45	0.10
		5	6.39	6.00	0.24
		6	6.68	6.29	0.26
		7	6.75	6.19	0.30
		8	6.75	6.28	0.29
		9	6.72	6.32	0.23
		10	6.78	6.40	0.24
		20	7.04	6.46	0.30
		30	7.64	6.49	0.45
		35	6.97	6.38	0.33
		40	7.99	7.13	0.35
	Hann	2	5.15	5.10	0.07

Table 4 continued from previous page

Scenario III	Window Type	Nº of Filters	$RT_{Max}[min]$	$RT_{Mean}[min]$	$RT_{\sigma}[min]$
		3	5.72	5.65	0.10
		5	6.50	6.15	0.27
		6	6.86	6.43	0.27
		7	7.00	6.48	0.28
		8	7.11	6.52	0.34
		9	7.00	6.59	0.24
		10	7.06	6.65	0.23
		20	7.31	6.67	0.40
		30	7.11	6.50	0.32
		35	7.21	6.57	0.36
		40	7.31	6.55	0.37
	Hamming	2	5.13	5.09	0.06
		3	5.75	5.67	0.10
		5	6.54	6.18	0.25
		6	6.86	6.46	0.23
		7	7.08	6.51	0.29
		8	7.14	6.63	0.34
		9	7.06	6.60	0.26
		10	7.12	6.65	0.29
		20	7.48	6.73	0.35
		30	7.29	6.62	0.37
		35	7.43	6.71	0.38
		40	7.31	6.63	0.35
	Rect	2	5.33	5.29	0.05
		3	6.55	6.09	0.40
		5	7.20	6.52	0.63
		6	7.58	6.76	0.92
		7	7.39	6.82	0.64
		8	7.81	6.91	0.64
		9	7.60	6.95	0.65
		10	8.01	6.87	0.65
		20	8.19	6.81	0.79
		30	8.49	6.67	0.89
		35	8.74	6.64	0.88
		40	8.51	6.46	0.83

Table 5. Reconstructio time of Scenario IV.

Scenario IV	Distribution	Nº of Filters	$RT_{Max}[min]$	$RT_{Mean}[min]$	$RT_{\sigma}[min]$
Shepp-Logan	Blackman	2	4.84	4.83	0.01
		3	5.37	4.86	0.50
		5	5.41	4.71	0.49
		6	5.65	4.76	0.45
		7	5.93	4.95	0.46
		8	21.86	11.73	7.31
		9	19.20	10.18	4.66
		10	8.82	6.44	1.33
		20	9.31	5.56	1.17
		30	21.37	9.39	5.17
		35	9.24	4.35	0.98
		40	6.97	4.22	0.94
	Hann	2	17.09	10.96	8.68
		3	9.45	6.26	2.77
		5	7.85	6.39	1.16
		6	5.96	5.31	0.56
		7	7.70	7.08	0.56
		8	6.75	6.13	0.48
		9	9.51	6.25	1.49
		10	10.54	6.66	1.74
		20	7.06	5.09	0.65
		30	6.51	4.54	0.54
		35	6.69	4.28	0.53
		40	6.89	4.02	0.58
	Hamming	2	5.66	5.60	0.08
		3	5.54	5.27	0.45
		5	6.71	5.44	0.78
		6	6.41	5.56	0.50
		7	6.64	5.55	0.53
		8	6.73	5.79	0.44
		9	7.14	5.77	0.57
		10	6.67	5.60	0.43
		20	6.43	4.98	0.46
		30	15.95	7.10	2.26
		35	6.99	4.59	0.55
		40	6.55	4.29	0.49

Table 5 continued from previous page

Scenario IV	Distribution	Nº of Filters	$RT_{Max}[min]$	$RT_{Mean}[min]$	$RT_{\sigma}[min]$
Brain	Blackman	2	4.14	3.93	0.31
		3	4.00	3.74	0.38
		5	4.05	3.66	0.27
		6	3.90	3.58	0.31
		7	4.16	3.56	0.38
		8	4.38	3.50	0.52
		9	4.68	3.58	0.48
		10	4.66	3.59	0.43
		20	4.66	3.13	0.57
		30	4.77	2.94	0.60
		35	4.41	2.70	0.48
		40	3.99	2.57	0.45
	Hann	2	3.81	3.21	0.85
		3	4.53	3.82	0.62
		5	3.99	3.40	0.43
		6	3.83	3.42	0.27
		7	3.71	3.36	0.33
		8	3.71	3.36	0.36
		9	4.00	3.36	0.36
		10	4.42	3.42	0.47
		20	4.46	3.09	0.52
		30	4.25	2.82	0.48
		35	4.12	2.68	0.46
		40	4.08	2.56	0.46
	Hamming	2	3.64	3.44	0.28
		3	4.29	3.76	0.52
		5	4.49	3.81	0.52
		6	4.30	3.86	0.40
		7	4.35	3.78	0.42
		8	4.33	3.78	0.47
		9	4.38	3.80	0.38
		10	4.62	3.81	0.45
		20	4.96	3.50	0.57
		30	4.82	3.20	0.57
		35	11.51	3.84	2.16
		40	10.69	3.77	1.82

Table 5 continued from previous page

Scenario IV	Distribution	Nº of Filters	$RT_{Max}[min]$	$RT_{Mean}[min]$	$RT_{\sigma}[min]$
Head	Blackman	2	5.66	5.43	0.34
		3	6.05	5.57	0.48
		5	6.29	5.92	0.33
		6	6.96	6.19	0.42
		7	6.69	6.25	0.33
		8	7.01	6.34	0.44
		9	6.76	6.11	0.41
		10	7.01	6.35	0.43
		20	6.40	5.77	0.39
		30	6.68	5.37	0.59
		35	6.71	5.09	0.62
		40	6.37	4.88	0.57
	Hann	2	5.47	5.26	0.30
		3	5.83	5.41	0.40
		5	6.13	5.74	0.36
		6	6.68	6.03	0.40
		7	6.47	6.07	0.28
		8	6.75	6.19	0.37
		9	6.44	6.21	0.26
		10	6.87	6.30	0.37
		20	6.70	5.93	0.45
		30	6.45	5.54	0.49
		35	6.64	5.39	0.57
		40	6.59	5.17	0.56
	Hamming	2	5.40	5.17	0.33
		3	5.86	5.38	0.43
		5	6.13	5.74	0.38
		6	6.72	6.03	0.41
		7	6.64	6.14	0.36
		8	6.84	6.25	0.41
		9	6.50	6.24	0.24
		10	6.85	6.27	0.40
		20	6.64	5.95	0.48
		30	6.27	5.48	0.46
		35	6.68	5.40	0.56
		40	6.75	5.21	0.56

Table 5 continued from previous page

Scenario IV	Distribution	Nº of Filters	$RT_{Max}[min]$	$RT_{Mean}[min]$	$RT_{\sigma}[min]$
Head*	Blackman	2	5.88	5.72	0.23
		3	6.47	5.99	0.45
		5	6.80	6.24	0.42
		6	7.26	6.51	0.47
		7	7.11	6.58	0.37
		8	7.31	6.59	0.51
		9	7.23	6.65	0.56
		10	7.24	6.60	0.55
		20	6.72	5.96	0.54
		30	6.22	5.43	0.56
		35	6.54	5.28	0.63
		40	6.07	5.03	0.59
	Hann	2	5.86	5.66	0.28
		3	6.14	5.77	0.34
		5	6.44	6.17	0.31
		6	7.62	7.05	0.48
		7	7.41	6.80	0.52
		8	6.81	6.45	0.27
		9	7.43	6.85	0.42
		10	7.20	6.57	0.47
		20	7.38	6.30	0.54
		30	7.26	5.92	0.68
		35	6.66	5.53	0.63
		40	6.25	5.30	0.58
	Hamming	2	5.86	5.54	0.45
		3	6.11	5.78	0.33
		5	6.39	6.01	0.32
		6	6.76	6.30	0.34
		7	6.71	6.38	0.32
		8	6.84	6.44	0.27
		9	6.91	6.46	0.35
		10	7.12	6.54	0.44
		20	6.90	6.30	0.49
		30	6.55	5.72	0.57
		35	6.77	5.52	0.62
		40	6.56	5.37	0.61

Table 6. Reconstruction time of Scenario V.

Scenario V	Nº of Filters	$RT_{Max}[min]$	$RT_{Mean}[min]$	$RT_{\sigma}[min]$
Shepp-Logan	2	3.51	3.44	0.10
	3	4.13	4.05	0.14
	5	10.18	9.26	0.80
	6	10.21	9.45	0.59
	7	10.99	9.43	0.89
	8	11.32	9.51	1.12
	9	11.09	9.58	0.89
	10	11.85	9.86	1.05
	20	12.29	10.18	0.95
	30	12.35	10.12	1.05
	35	12.48	9.92	0.90
	40	11.45	8.57	1.83
Brain	2	2.46	2.28	0.26
	3	3.34	3.16	0.22
	5	9.90	9.01	0.64
	6	10.40	9.23	0.84
	7	10.68	9.59	0.87
	8	10.77	9.37	0.84
	9	10.18	9.36	0.72
	10	10.80	9.34	0.91
	20	12.40	9.78	1.18
	30	13.33	10.12	1.36
	35	12.91	10.30	1.18
	40	10.91	8.07	1.16
Head	2	4.42	4.32	0.14
	3	5.28	5.12	0.22
	5	6.13	5.68	0.42
	6	6.62	5.87	0.52
	7	6.28	5.75	0.46
	8	6.61	5.93	0.59
	9	6.97	6.09	0.71
	10	7.16	6.18	0.69
	20	7.52	6.49	0.61
	30	7.89	6.42	0.85
	35	8.24	6.42	0.79
	40	8.10	6.49	0.93

Table 6 continued from previous page

Scenario V	Nº of Filters	$RT_{Max}[min]$	$RT_{Mean}[min]$	$RT_{\sigma}[min]$
Head*	2	5.31	5.12	0.27
	3	6.22	5.91	0.30
	5	6.61	6.32	0.37
	6	7.32	6.56	0.48
	7	7.23	6.57	0.51
	8	7.95	7.38	0.55
	9	7.88	6.71	0.66
	10	8.14	6.75	0.70
	20	8.94	7.04	0.82
	30	8.91	6.96	0.89
	35	9.21	6.85	0.91
	40	9.13	7.02	0.92

B Hardware Info

Table 7. Hardware information of Asus k45Vm.

Asus k45Vm	
Processor	Intel(R) Core(TM) i7-3610QM CPU @ 2.30
Architecture	x86_64
Memory	8GB, DDR3 1600 MHz SDRAM
Core/threads	4/8
CPU(s)	8
Kernel Version	Linux 42~16.04.1-Ubuntu

Table 8. Hardware information of Virgo 2.0 from [29].

Virgo Cluster	
Virgo 2.0	Beowulf Cluster
Nodes	23
Processor	Intel Quad Core XEON E5430
Memory	8GB/64GB/16GB to 32GB - Depends on node.
OS	CentOS (RHEL)

C Annex

Articles Search Definitions

C.1 IEEE Xplore Digital Library

Boolean expression: MRI AND (Segmentation OR Delineation OR Detection OR Classification OR Diagnosis OR Early Diagnosis).
Search on Metadata: Includes abstract, summary, title text and indexing terms.
Year range: 2018 - 2019.
Search returned 992 articles.

C.2 Web of Science

Boolean expression: TS = (MRI AND (Segmentation OR Delineation OR Detection OR Classification OR Diagnosis OR Early Diagnosis)).
Article types: Includes classical article, clinical trial and review.
Sorted by: Best match.
Year range: 2018 - 2019.
Search returned 9.858 articles.

C.3 PubMed

Boolean expression: MRI AND (Segmentation OR Delineation OR Detection OR Classification OR Diagnosis OR Early Diagnosis).
Search on Metadata: Includes abstract, summary, title text and indexing terms.
Year range: 2018 - 2019.
Search returned 39.724 articles.

Table 9. The ten most relevant articles in MRI searched with the advanced definitions in Section C.1 on IEEE Xplore Digital Library.

Order	Title	Authors	DOI	Reference Count	Publisher
1	Boundary Delineation of MRI Images for Lumbar Spinal Stenosis Detection Through Semantic Segmentation Using Deep Neural Networks	A. S. Al-Kafri; S. Sudirman; et al.	10.1109/ACCESS.2019.2908002	46	IEEE
2	An Intelligent System for Early Assessment and Classification of Brain Tumor	T. Keerthana; S. Xavier	10.1109/ICICCT.2018.8473297	13	IEEE
3	Automatic Segmentation and Cardiopathy Classification in Cardiac Mri Images Based on Deep Neural Networks	Y. Chang; B. Song; C. Jung; et al.	10.1109/ICASSP.2018.8461261	13	IEEE
4	Enhancement and automated segmentation of ultrasound knee cartilage for early diagnosis of knee osteoarthritis	P. R. Desai; I. Hacihaliloglu	10.1109/ISBI.2018.8363850	9	IEEE
5	Comprehensive computer-aided diagnosis for breast T1-weighted DCE-MRI through quantitative dynamical features and spatio-temporal local binary patterns	G. Piantadosi; S. Marrone; et al.	10.1049/iet-cvi.2018.5273	109	IET
6	A Significant Regional-based Diagnosis System for Early Detection of Alzheimer?s Disease Using sMRI Scans	F. E. A. El-Gamal; M. M. Elmogy; et al.	10.1109/ISSPIT.2018.8642665	33	IEEE
7	Segmentation of MRI images for brain cancer detection	W. El Hajj Chehade; R. A. Kader; et al.	10.1109/ICOIACT.2018.8350721	11	IEEE
8	Image Segmentation for Detection of Knee Cartilage	A. Thengade; B. H. Mutha	10.1109/ICCUBEA.2018.8697658	10	IEEE
9	Segmentation and Detection of Tumor in MRI images Using CNN and SVM Classification	R. Vinoth; C. Venkatesh	10.1109/ICEDSS.2018.8544306	16	IEEE
10	Early Diagnosis of Alzheimer's Disease: A Neuroimaging Study with Deep Learning Architectures	J. Islam; Y. Zhang	10.1109/CVPRW.2018.00247	12	IEEE

Table 10. The ten most relevant articles in MRI searched with the advanced definitions in Section C.2 on Web of Science.

Order	Title	Authors	DOI	Total Citations	Publisher
1	Diagnosis of multiple sclerosis: 2017 revisions of the McDonald criteria	Thompson, Alan J.; Banwell, Brenda L.; et al.	10.1016/S1474-4422(17)30470-2	267	ELSEVIER SCIENCE
2	MRI-Targeted or Standard Biopsy for Prostate-Cancer Diagnosis	Kasivisvanathan, V; Rannikko, ; et al.	10.1056/NEJMoa1801993	208	MASSACHUSETTS MEDICAL SOC
3	International guidelines for groin hernia management	Simons, M. P.; Smietanski, M.; et al.	10.1007/s10029-017-1668-x	78	SPRINGER
4	Multimodal Neuroimaging Feature Learning With Multimodal Stacked Deep Polynomial Networks for Diagnosis of Alzheimer's Disease	Shi, Jun; Zheng, Xiao; et al.	10.1109/JBHI.2017.2655720	40	IEEE-INST
5	Learning a variational network for reconstruction of accelerated MRI data	Hammernik, Kerstin; Klatzer, Teresa; et al.	10.1002/mrm.26977	39	WILEY
6	Deep convolutional neural network and 3D deformable approach for tissue segmentation in musculoskeletal magnetic resonance imaging	Liu, Fang; Zhou, Zhaoye; et al.	10.1002/mrm.26841	31	WILEY
7	A new switching-delayed-PSO-based optimized SVM algorithm for diagnosis of Alzheimer's disease	Zeng, Nianyin; Qiu, Hong; et al.	10.1016/j.neucom.2018.09.001	29	ELSEVIER SCIENCE BV
8	Coordination-Responsive Longitudinal Relaxation Tuning as a Versatile MRI Sensing Protocol for Malignancy Targets	Zhang, Kun; Cheng, Yu; et al.	10.1002/advs.201800021	29	WILEY
9	Optimising the Diagnosis of Prostate Cancer in the Era of Multiparametric Magnetic Resonance Imaging: A Cost-effectiveness Analysis Based on the Prostate MR Imaging Study (PROMIS)	Faria, Rita; Soares, Marta O.; et al.	10.1016/j.eururo.2017.08.018	29	ELSEVIER SCIENCE BV
10	A Meshfree Representation for Cardiac Medical Image Computing	Zhang, Heye; Gao, Zhifan; et al.	10.1109/JTEHM.2018.2795022	28	IEEE-INST

Table 11. The ten most relevant articles in MRI searched with the advanced definitions in Section C.3 on PubMed.

Order	Title	Authors	URL	Journal
1	Early undifferentiated arthritis.	Micheroli R, Ciurea A.	/pubmed/29468290	Der Orthopäde
2	Tokyo Guidelines 2018: diagnostic criteria and severity grading of acute cholangitis (with videos).	Kiriyama S, Kozaka K, et al.	/pubmed/29032610	Journal of Hepato-Biliary-Pancreatic Sciences
3	A review on automatic fetal and neonatal brain MRI segmentation.	Makropoulos A, Counsell SJ, et al.	/pubmed/28666878	NeuroImage
4	Early Diagnosis and Treatment of Cerebral Palsy in Children with a History of Preterm Birth.	Spittle AJ, Morgan C, et al.	/pubmed/30144846	Clinics in Perinatology
5	MRI in otology: applications in cholesteatoma and Ménière's disease.	Lingam RK, Connor SEJ, et al.	/pubmed/28969854	Clinical Radiology
6	Clinical Diagnostic Tests Versus MRI Diagnosis of ACL Tears.	Brady MP, Weiss W.	/pubmed/29140170	Journal of Sport Rehabilitation
7	Impact of Advancing Technology on Diagnosis and Treatment of Breast Cancer.	Greenwood HI, Dodelzon K, et al.	/pubmed/30005769	Surgical Clinics of North America
8	The value of MRI in early diagnosis of dysbaric osteonecrosis.	Shen YT, Chen H, et al.	/pubmed/30248746	Chinese Journal of Industrial Hygiene and Occupational Diseases
9	Whole Body MRI and oncology: recent major advances.	Pasoglou V, Michoux N, et al.	/pubmed/29334236	The British Journal of Radiology
10	MRI Brain Tumour Segmentation Using Hybrid Clustering and Classification by Back Propagation Algorithm	M M, P S.	/pubmed/30486629	Asian Pacific Journal of Cancer Prevention,

References

[1] Daniel L. F. Almeida. Reconstrução de imagens de ressonância magnética com base em compressive sensing usando informação a priori estrutural em abordagem bayesiana. Dissertação de mestrado, Universidade de Brasília - Faculdade do Gama (FGA), December 2016. Programa de Pós-Graduação em Engenharia Biomédica.

[2] C. Andica, A. Hagiwara, M. Nakazawa, et al. The Advantage of Synthetic MRI for the Visualization of Early White Matter Change in an Infant with Sturge-Weber Syndrome. *Magnetic Resonance in Medical Sciences*, 15(4):347–348, 2016.

[3] Y. Assaf. Imaging laminar structures in the gray matter with diffusion MRI. *NeuroImage*, 2018.

[4] R. Baraniuk. Compressive Sensing [Lecture Notes]. *IEEE Signal Processing Magazine*, 24:118–121, 2007.

[5] M. Bernstein, K. King, e X. Zhou. *Handbook of MRI Pulse Sequences*. 2004.

[6] R. Brown, Y. Cheng, E. Haacke, et al. Magnetic Resonance Imaging: Physical Principles and Sequence Design. 2014.

[7] Image by OpenClipart-Vectors from Pixabay. Female Anatomy of Body in a Standing Position, October 2013. Available at https://pixabay.com/vectors/female-body-woman-standing-anatomy-154952/. Image under Pixabay License. Last access: July 2nd, 2019.

[8] Servier Medical Art by Servier. Normal Vertebral Column. Available at https://smart.servier.com/smart_image/vertebral-column-7/. Image under Creative Commons Licence. Last access: July 2nd, 2019.

[9] E. Candès. The restricted isometry property and its implications for compressed sensing. *Comptes Rendus Mathematique*, 2008.

[10] E. Candès, J. Romberg, e T. Tao. Robust Uncertainty Principles : Exact Signal Reconstruction from Highly Incomplete Frequency Information. páginas 1–41, 2005.

[11] E. Candès, J. Romberg, e T. Tao. Robust Uncertainty Principles : Exact Signal Frequency Information. 52(2):489–509, 2006.

[12] E. Candès e T. Tao. Near Optimal Signal Recovery from Random Projections. 2006. https://arxiv.org/abs/math/0410542.

[13] E. Candès e M Wakin. An introduction to compressive sampling. *Signal Processing Magazine, IEEE*, 25(2):21–30, 2008.

[14] R. Chartrand. Iteratively Reweighted Algorithms for Compressive Sensing. páginas 1–4, 2008.

[15] Sansum Clinic. Mri of the abdomen. Available at https://www.sansumclinic.org/medical-services/radiologyGR/mri---magnetic-resonance-scanning/mri-of-the-abdomen. Last access: March 18th, 2019.

[16] Fábio J. Costa. Reconstrução de imagens de ressonância magnética com base em *Compressive Sensing* com pré-filtragem no domínio de medidas usando computação paralela. Dissertação de mestrado, Universidade de Brasília - Faculdade do Gama (FGA), December 2016. Programa de Pós-Graduação em Engenharia Biomédica.

[17] C. Dagia e M. Ditchfield. 3T MRI in paediatrics: Challenges and clinical applications. *European Journal of Radiology*, 68(2):309–319, November 2008.

[18] S. Dahdouh, N. Andescavage, S. Yewale, et al. In vivo placental MRI shape and textural features predict fetal growth restriction and postnatal outcome. *Journal of Magnetic Resonance Imaging*, 47(2):449–458, 2018.

[19] D. Donoho. Compressed sensing. *IEEE Transactions on Information Theory*, 2006.

[20] E. Dyrberg, E. Larsen, H. Hendel, et al. Diagnostic bone imaging in patients with prostate cancer: patient experience and acceptance of NaF-PET/CT, choline-PET/CT, whole-body MRI, and bone SPECT/CT. *Acta Radiologica*, page 028418511775128, 2018.

[21] J. Edmund e T. Nyholm. A review of substitute CT generation for MRI-only radiation therapy. *Radiation Oncology*, 12(1):28, dec 2017.

[22] M. Foster. Magnetic resonance in medicine and biology. 1984.

[23] S. Foucart e H. Rauhut. *A Mathematical Introduction to Compressive Sensing*. 2013.

[24] N. Gorelik, S. Reddy, R. Turcotte, et al. Early detection of metastases using whole-body MRI for initial staging and routine follow-up of myxoid liposarcoma. *Skeletal Radiology*, 47(3):369–379, mar 2018.

[25] G. Grolez, M. Kyheng, R. Lopes, et al. MRI of the cervical spinal cord predicts respiratory dysfunction in ALS. *Scientific Reports*, 8(1):1828, dec 2018.

[26] J. Hornak. *The basics of MRI.* Interactive Learning Software, Henietta, NY, Bellingham, Wash. New York, 1996-2010.

[27] Y. Hue, A. Guimaraes, O. Cohen, et al. Magnetic Resonance Mediated Radiofrequency Ablation. *IEEE Transactions on Medical Imaging*, 37(2):417–427, 2018.

[28] T. Küstner, C. Würslin, S. Gatidis, et al. MR image reconstruction using a combination of compressed sensing and partial fourier acquisition: Espresso. *IEEE Transactions on Medical Imaging*, 35(11):2447–2458, November 2016.

[29] UTEP Distributed Computing Lab. Computing resources. Available at http://wwwold.ece.utep.edu/research/webdcl/index.html. Last access: Jul 12$^{\text{th}}$, 2019.

[30] Z. Liang e P. Lauterbur. *Principles of Magnetic Resonance Imaging: A Signal Processing Perspective.* SPIE Optical Engineering Press, 2000.

[31] R. Lim, T. Flood, M. McInnes, et al. Renal angiomyolipoma without visible fat: Can we make the diagnosis using ct and mri? *European Radiology*, 28(2):542–553, February 2018.

[32] T. Liu, S. Wang, H. Liu, et al. Detection of vertebral metastases: a meta-analysis comparing MRI, CT, PET, BS and BS with SPECT. *Journal of Cancer Research and Clinical Oncology*, 143(3):457–465, March 2017.

[33] D. Lloyd, M. van Poppel, A. Schultz, et al. 31 Motion corrected fetal cardiac mri increases diagnostic confidence in clinically challenging cases. In *Heart*, volume 104, páginas A11–A11, 2018.

[34] M. Lustig. *Sparse MRI.* Phd thesis, Stanford University, September 2008.

[35] M. Meier-Schroers, R. Homsi, D. Skowasch, et al. Lung cancer screening with MRI: results of the first screening round. *Journal of Cancer Research and Clinical Oncology*, 144(1):117–125, January 2018.

[36] C. Miosso, R. von Borries, M. Argàez, et al. Compressive Sensing Reconstruction With Prior Information by Iteratively Reweighted Least-Squares. 57(6):2424–2431, 2009.

[37] C. Miosso, R. von Borries, e J. Pierluissi. Compressive sensing method for improved reconstruction of gradient-sparse magnetic resonance images. *Signal, System and Computers, 2009 Conference Record on the Forty-Third Asilomar Conference on*, páginas 799–806, 2009.

[38] C. Miosso, R. von Borries, e J. Pierluissi. Compressive sensing with prior information: Requirements and probabilities of reconstruction in ℓ_1-minimization. *IEEE Transactions on Signal Processing*, 61(9):2150–2164, 2013.

[39] National Institute of Diabetes, Digestive, e Kidney Diseases (NIDDK). Urinary Tract Imaging, May 2012. Available at https://www.niddk.nih.gov/health-information/diagnostic-tests/urinary-tract-imaging. Last access: May 24$^{\text{th}}$, 2019.

[40] Department of Radiology & Biomedical Imaging. Prepare for Magnetic Resonance Imaging (MRI). Available at https://radiology.ucsf.edu/patient-care/prepare/mri. Last access: January 29$^{\text{th}}$, 2019,.

[41] A. Owrangi, P. Greer, C. Glide-hurst, et al. MRI-only treatment planning : benefits and challenges. 63(5):1–30, 2019.

[42] Gian L. de O. Paiva. Comparação Objetiva de Imagens de Ressonância Magnética usando Compressive Sensing em Diferentes Estruturas de Decomposição Multinível. Dissertação de mestrado, Universidade de Brasília - Faculdade do Gama (FGA), 2017. Programa de Pós-Graduação em Engenharia Biomédica.

[43] The Visible Human Project. Specimen from the Visible Human Male - Abdomen subset. Available at https://www.nlm.nih.gov/research/visible/mri.html Last access: May 24$^{\text{th}}$, 2019.

[44] B. Rao e K Kreutz-Delgado. An affine scaling methodology for best basis selection. *IEEE Transactions on Signal Processing*, 1999.

[45] J. Romberg. l_1-magic - Barrier iterations for equality constrained TV minimizaiton., October 2015. Available at https://statweb.stanford.edu/~candes/l1magic/. Last access: Jul 9$^{\text{th}}$, 2019.

[46] W. Rooney e D. McRobbie. *MRI: From Picture to Proton*, volume 85. 2003.

[47] K. Schilling, Y. Gao, V. Janve, et al. Confirmation of a gyral bias in diffusion MRI fiber tractography. *Human Brain Mapping*, 39(3):1449–1466, March 2018.

[48] P. Shah, D. Bassett, L. Wisse, et al. Mapping the structural and functional network architecture of the medial temporal lobe using 7T MRI. *Human Brain Mapping*, 39(2):851–865, 2018.

[49] J. van Amerom, D. Lloyd, A. Price, et al. Fetal cardiac cine imaging using highly accelerated dynamic MRI with retrospective motion correction and outlier rejection. *Magnetic Resonance in Medicine*, 79(1):327–338, 2018.

[50] R. von Borries, C. Miosso, e C. Potes. Directional filter banks for wavelet decomposition of images based on the radon transform. 2007.

[51] Z. Wang e A. Bovik. Mean squared error: Love it or leave it? a new look at signal fidelity measures. *IEEE Signal Processing Magazine*, 26(1):98–117, January 2009.

[52] Z. Wang, A. Bovik, e H. Sheikh. Structural Similarity Based Image Quality Assessment. In *Digital Video Image Quality and Perceptual Coding*. CRC press, 2005.